Tidal flows, sill dynamics, and mixing in the Canadian Arctic Archipelago

Kenneth Hughes
B. Sc. (Hons), University of Otago, 2011
M. Sc., University of Otago, 2013

A dissertation submitted in partial fulfilment
of the requirements for the degree of

Doctor of Philosphy

in the School of Earth
and Ocean Sciences

Tidal flows, sill dynamics, and mixing in the Canadian Arctic Archipelago

Kenneth Hughes
B. Sc. (Hons), University of Otago, 2011
M. Sc., University of Otago, 2013

Supervisory committee

Dr. Jody Klymak, Supervisor
School of Earth and Ocean Sciences

Dr. Ann Gargett, Departmental Member
School of Earth and Ocean Sciences

Dr. Bill Williams, Additional Member
Institute of Ocean Sciences

Dr. Charles Hannah, Committee Member
Institute of Ocean Sciences

Dr. Brad Buckham, Outside Member
Department of Engineering

Abstract

The transport of low-salinity waters through the Canadian Arctic Archipelago links the North Pacific, Arctic, and North Atlantic Oceans. This transport is influenced by many related small-scale processes including mixing, internal hydraulics, and internal tide generation. In this thesis, I quantify and elucidate the physics of such processes with aims of addressing discrepancies between observed and simulated fluxes through the Archipelago and advancing the skill of numerical models by identifying shortcomings and informing where and how progress can be achieved.

To address the dearth of mixing rates across the network of channels, I first use a large-scale model to obtain baseline estimates of the spatial and seasonal variability of the vertical buoyancy flux. Much of the mixing occurs in the eastern half of the Archipelago and is attributed to the abundance of sills and narrow channels. Indeed, the so-called 'central sills area' is shown to be a mixing hot spot. I investigate this region further using high-spatial-resolution observational transects to examine the role of tides, which are excluded from the large-scale model. The many shallow channels here accelerate tidal currents and thereby induce strong bottom boundary layer dissipation. This is the largest energy sink within an observationally constrained energy budget. The generation of internal tides is another primary sink of barotropic tidal energy. Because the study site lies poleward of the critical latitudes of the dominant tidal constituents, internal tides propagate as internal Kelvin waves. Idealized, process-oriented modelling demonstrates that the amplitudes of such waves, or similarly the energy extracted from the barotropic tide, is sensitive to channel width because waves generated at each side of the channel interfere. Given the multiple connecting channels of the Archipelago, it is difficult to make a priori estimates of internal tide generation for a given channel. Nevertheless, the phenomenology I describe will be detectable in, and a requisite to understanding, pan-Arctic or global three-dimensional tidal models, which are becoming more prevalent.

Contents

List of figures

List of tables

Acknowledgments

I would like to thank my advisor Jody for all the help over the past four years. His mutual enthusiasm for combining numerical modelling and observational analysis appealed to my interest and has left me with many skills that I will be able to use into the future as well as the chance to board a ship in the Arctic, which I won't forget. Jody's editor's eye for both the details and bigger picture put my papers and abstracts on much stronger footing before submission.

Xianmin Hu and Paul Myers kindly provided model output to help me get spun up on how the Archipelago works. I'm not sure I want to know the amount of work that goes into getting one of these models to run. So to simply be offered whatever output I needed was a great help.

Bill Williams's and Humfrey Melling's expertise on all things Archipelago proved very helpful. Their input on the cruise planning made our short survey in the Arctic effective and worthwhile, and their comments helped resolve a number of pieces of the observational puzzle that is Chapter 3.

Hauke Blanken, Rowan Fox, and numerous people from the ArcticNet and Amundsen Science teams helped with the actual deployment, use, and retrieval of profilers, without which I wouldn't have any data to analyse.

To my committee, Bill, Charles, Ann, and Brad, thanks for all enthusiastically agreeing to be a member, for pointing me to important parts of the literature that I might otherwise have missed, reading my drafts, and advice throughout.

The observational component of this thesis was funded through the Canadian Geotraces project, part of the Natural Sciences and Engineering Research Council of Canada's Climate Change and Atmospheric Research initiative. Computing power was provided by WestGrid and Compute Canada.

Finally, thanks to Erin for coming to Canada with me, finding us a place to live, teaching me how to be a cat dad, planning road trips, and coming with me to my next academic adventure.

Chapter 1

Introduction

1.1 The roles of the Archipelago

The Canadian Arctic Archipelago is a topographically complex region and one of two main outflows of water from the Arctic Ocean to the North Atlantic. Much of the outflowing water originates from the Pacific and is low salinity owing to a net convergence of atmospheric water vapour over the north Pacific (Broecker, 1991, Figure 1.1). One estimate puts the equivalent freshwater flux out of the Archipelago at 70 mSv, 35% of the total out of the Arctic (Serreze et al., 2006).

Early studies viewed the freshwater outflow as important for its direct limiting effect on deep convection in the Labrador Sea, one starting point for the meridional overturning circulation. The argument, supported by coarse-resolution models (Goosse et al., 1997; Wadley and Bigg, 2002), is that freshwater exiting the Archipelago will end up in the Labrador Sea and act as a cap thereby reducing the overturning circulation in the North Atlantic Ocean. Reductions of 1–5 Sv (5–25%) occurred when the gap (one or two grid cells wide) representing the Archipelago was closed.

Newer, higher-resolution studies suggest this is not the case (Myers, 2005; Komuro and Hasumi, 2005). The freshwater is largely confined to the shelf, away from the centre of the Labrador Sea where the convection occurs. In fact, freshwater outflow through the Archipelago may actually lead to more saline water, via the pathway east of Greenland, arriving in the Labrador Sea (Komuro and Hasumi, 2005). Nevertheless, the freshwater cap concept perpetuates in the recent literature (e.g., Wang et al., 2016). Beszczynska-Möller et al. (2011) summarizes it best by stating that the details of how freshwater affects meridional overturning circulation are poorly known.

Freshwater remains an important metric and there are more pressing issues than possible slight trends in the overturning circulation. Changes in the magnitude, distribution, and phase of freshwater are predicted in the future. Hu

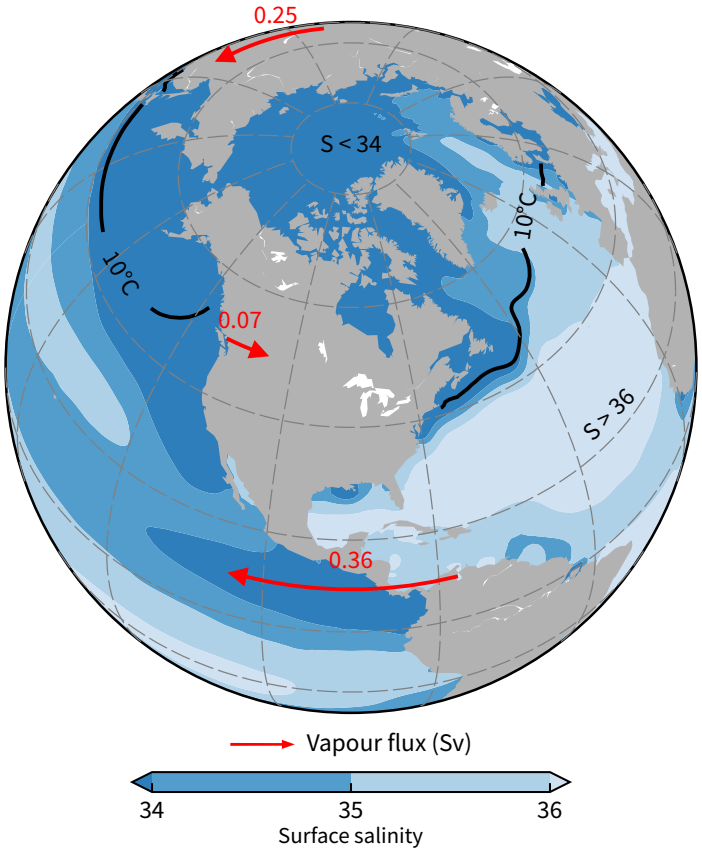

Figure 1.1 – Surface hydrographic differences between the Pacific and Atlantic Oceans. The noticeable differences in temperature and salinity between the two basins persist with depth. Net vapour flux across drainage basin boundaries follow Broecker (1991).

and Myers (2014), for example, predict significant decreases in volume and freshwater fluxes through the central Archipelago in the coming decades. Associated with such changes will be changes in properties and boundaries of ocean biomes (Michel et al., 2006; Carmack, 2007); the rate of ocean acidification, as mixing with freshwater reduces seawater's alkalinity (Carmack et al., 2016); and the potential for heat from warm Atlantic waters, otherwise at kept at mid-depth due to low-salinity surface waters, to reach the near surface in some places (Rippeth et al., 2015). Ultimately, freshwater outflow is one of the Arctic Ocean's links to the global hydrological cycle (Serreze et al., 2006; Melling et al., 2008; Woodgate, 2013).

1.2 Spanning the scales

At large scales, volume and freshwater fluxes through the Archipelago are driven by differences in density and atmospheric pressure. The two strongly correlated fluxes are modulated by smaller-scale (metre to kilometre) phenomena such as internal waves, topographically induced eddies, and hydraulic jumps. The consequent mixing, bottom-pressure variability, and hydraulic control act to modify the source waters, increase drag, and influence fluxes. These processes are often not explicitly resolved by large-scale circulation models or mesoscale surveys; therefore, process-oriented studies are necessary to understand and quantify the cumulative effect of these unresolved motions.

The shallow ($\sim$100–600 m) channels within the Archipelago (Figure 1.2) host waters with components that can be traced back to the North Pacific Ocean, the North Atlantic Ocean, the rivers of North America and Eurasia (e.g., Carmack et al., 2008), and the annual cycle of sea ice growth and decay. The many freshwater components of the system result in a net flux of low-salinity (S=32–33) water from the Arctic toward the Atlantic Ocean. A clear example of the different sources and modification of waters across the Archipelago is Figure 2.6 of de Lange Boom et al. (1987, reproduced in Figure 1.3). Note the diverging isohalines (effectively isopycnals in this context) near Penny Strait and Wellington Channel, a clear signature of mixing. Further southeastward, the isohalines converge owing to the introduction of water masses from other pathways.

Even a single channel may host waters from different sources. This occurs because many channels are an order of magnitude wider than the internal Rossby radius, a measure of the scale at which rotation is relevant, which is 2–10 km throughout the Archipelago (Figure 1.4). Indeed, the Archipelago is oceanographically unique in its preponderance of dynamically wide channels (Leblond, 1980). Such a trait poses a challenge to both observationalists and numerical modellers.

Any simulation or survey intending to adequately capture the physics of interactions between stratified flow and topography requires grid or station spacing on the order of a few kilometres or better. Observational studies address this problem in part by increasing spatial resolution near coasts. Similar scale-dependent approaches from a modelling perspective show promise (e.g., Wekerle et al., 2013), but resolution will remain an issue for the foreseeable future given

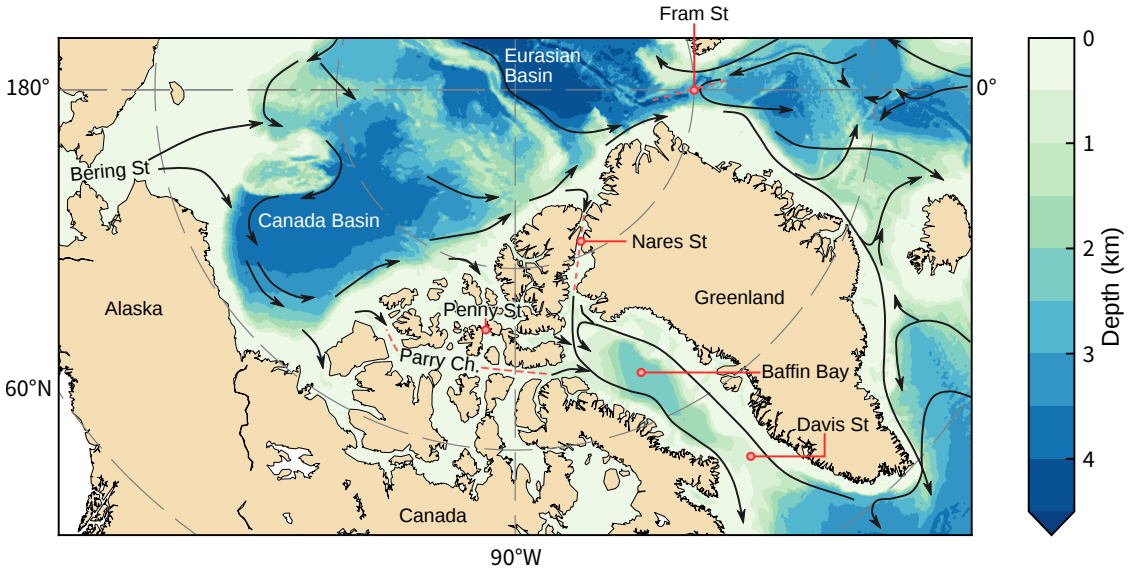

Figure 1.2 – Representative near-surface circulation in and around the Archipelago. Arrows follow Beszczynska-Möller et al. (2011).

the small internal Rossby radii.

1.3 Problems with existing models

Large-scale models focusing on the Archipelago estimate larger volume fluxes than observations, indicating that improved physics is needed in these models. Wekerle et al. (2013) and Lu et al. (2014) both simulate volume fluxes through the eastern end of Parry Channel that are approximately twice the value estimated from observations (Prinsenberg et al., 2009). Discrepancies also exist in the simulated salinity, which has consequences for the freshwater flux. Houssais and Herbaut (2011) found the simulated polar water to be too fresh and therefore overestimated total freshwater flux, whereas Lu et al. (2014) suggest that a positive bias in their simulated salinity resulted in underestimation of freshwater flux through Nares Strait.

A factor-of-two discrepancy in the volume flux is concerning. This is exacerbated by looking at coarser-resolution models. For example, Jahn et al. (2012) compare 10 different models in the Arctic Ocean Model Intercomparison Project (Figure 1.5). The comparison demonstrates both a fivefold range in freshwater

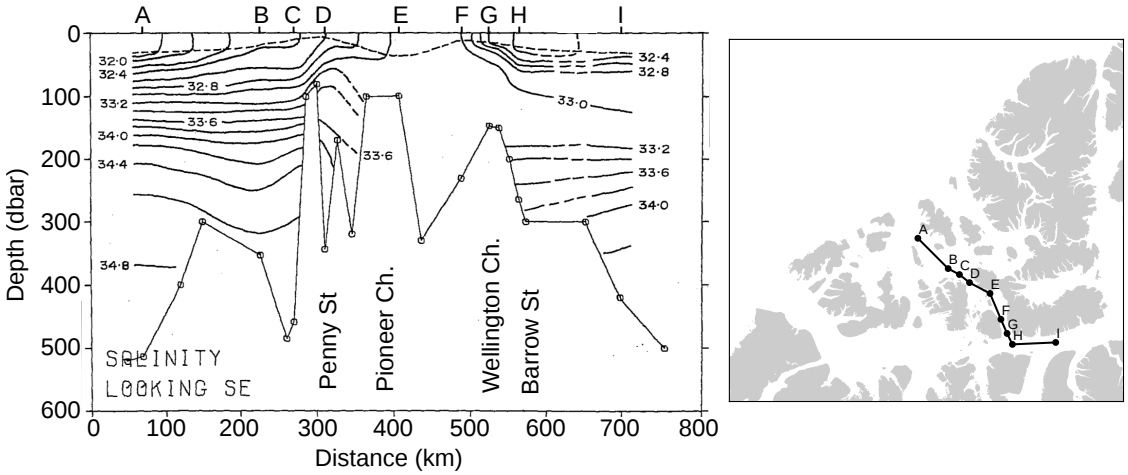

Figure 1.3 – Isohalines across the Archipelago. Original figure from de Lange Boom et al. (1987). Net flow is left to right.

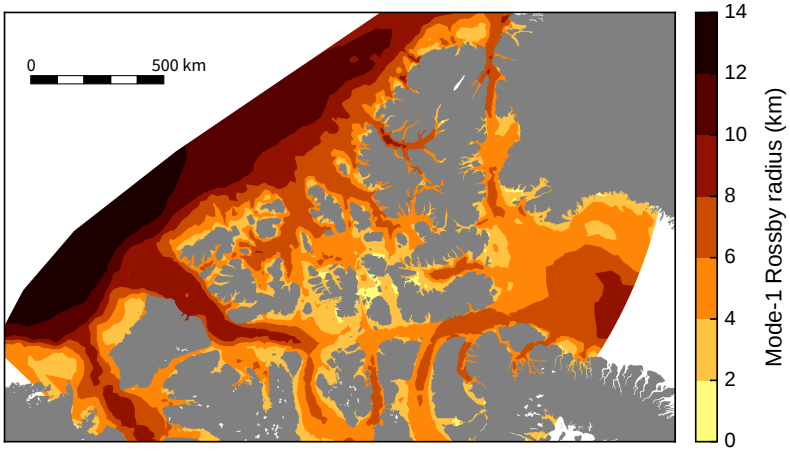

Figure 1.4 – The internal Rossby radius in late summer. Values are calculated following Chelton et al. (1998) using temperature and salinity climatologies based on data centred about September 1 (Kliem and Greenberg, 2003).

flux and that there is no robust relationship between resolution and freshwater flux and its standard deviation. Jahn et al. further caution that models can have the right freshwater flux despite incorrect physics and flow, hampering an ability to predict future change.

Resolution is nevertheless important in the Archipelago as demonstrated by Wang et al. (2017). Changing grid resolution in only the Archipelago, they demonstrated induced circulation changes across the Arctic Ocean. Indeed, they

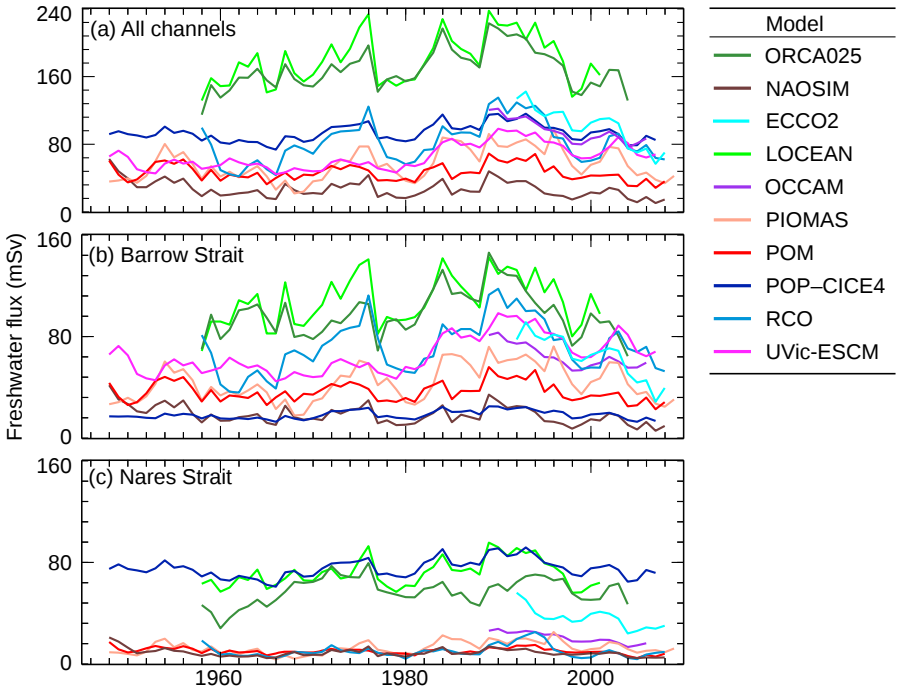

Figure 1.5 – A fivefold range in simulated freshwater fluxes from a model intercomparison. Figure adapted from Jahn et al. (2012).

conclude that an important task for development of ocean climate models is tuning the necessarily coarse representation of the Archipelago. Ideally such a task will be somewhat physically based and constrained rather than simply an empirical match to observations and higher-resolution models.

Tides are not included in studies cited thus far. Their relevance is often outweighed by their additional complexity and computational cost. Notable exceptions are the Arctic Ocean FVCOM (Chen et al., 2009, 2016; Zhang et al., 2016), a NEMO configuration for the pan-Arctic system (Luneva et al., 2015) and a NEMO configuration under development for the Arctic and North Atlantic (pers. comm. Paul Myers). Of these studies, only Chen et al. describe any implications for the Archipelago. Of note, they highlight the importance of topographically trapped waves to dissipation.

Excluding tides is typically justified by a study's focus on seasonal and interannual time scales. Despite not playing a direct role over such scales, tides nevertheless need to be accounted for. For example, Melling (2000) propose in-

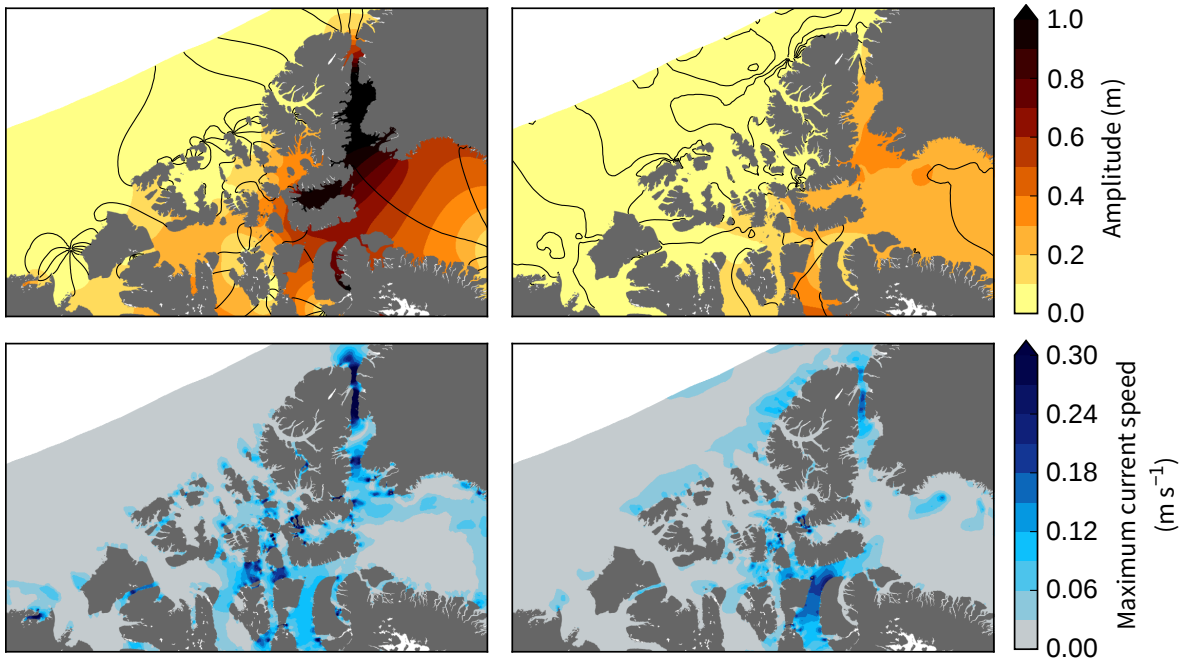

Figure 1.6 – Properties of the M_2 and K_1 tide. In both cases, the tides primarily arrive from the Atlantic via Baffin Bay (McLaughlin et al., 2004; Prinsenberg and Hamilton, 2005). Higher tidal amplitudes and current speeds reach as far west as the sill in Barrow Strait, which reflects much of the incoming tide. Data are from a barotropic tidal model (Collins et al., 2011) and co-phase lines are spaced in 30° increments.

creasing the drag coefficient to account for the drag induced by strong tidal flow. Dewey et al. (2005) suggest the same to account stratified flow over an isolated obstacle. Such proposals raise first-order questions: how much should the drag coefficient be increased? where should it be increased? and what dimensional or non-dimensional parameters should be taken in account?

The two main tidal constituents in the Archipelago, M_2 and K_1 (Figure 1.6), are both spatially heterogeneous. Consequently, drag, mixing, and energy losses, which scale nonlinearly with tidal velocity, will likely be confined to hotspots (see, e.g., Hannah et al., 2009). Furthermore, mean currents will typically be accelerated in the same places as tidal currents, which raises a further question: how do mean and tidal currents couple with respect to energetics?

1.4 Characterizing friction

A possible explanation for the volume flux discrepancies described is poor parameterization of the friction acting on the flow within channels. This friction acts to limit the flow that arises predominantly from a 10–20 cm sea level difference between the Arctic Ocean and Baffin Bay (Houssais and Herbaut, 2011; Wang et al., 2012; Wekerle et al., 2013). Improving the models will require characterizing the friction within channels of appropriate geometry, hydrography, and forcing.

In regions with complex topography, boundary layer friction associated with tangential stress is augmented or even dominated by form drag, the force that arises due to pressure differences across irregular topography such as a ridge or headland due to generation of baroclinic motions. Unlike frictional drag, form drag is not currently well parametrized (Moum et al., 2008; Warner and MacCready, 2014) and can have nonlocal consequences: waves generated in one location can deposit momentum elsewhere. (A quantity related to form drag that is used in this thesis is the energy loss that it induces.)

Warner et al. (2013) found that form drag at Three Tree Point in Puget Sound, Washington was 30 times larger than frictional drag over a flat bottom of the same area. The form drag there manifests as both internal waves and topographically induced eddies. Although this is likely an extreme example, a key point is the enhancement of form drag by tides. This is well demonstrated by the curious, albeit artificial, example of potential (inviscid) flow around a cylinder (e.g., D'Alembert, 1752; Warner and MacCready, 2009). If the flow is steady, there is no drag. If the flow is oscillatory, form drag is nonzero and its magnitude is proportional to the oscillation frequency. A more realistic example is the periodic formation of internal hydraulic jumps due to tidal flow over a ridge (e.g., Klymak and Gregg, 2001). Typically, the pressure on the upstream face of the ridge will be noticeably greater than on the downstream face leading to drag even in the absence of bottom friction or viscosity (e.g., Pratt and Whitehead, 2008, p. 69).

Diagnosing form drag is a challenge, requiring careful, localized observations or high-resolution modelling. MacCready et al. (2003) estimates topography with length scales of 20 m to 10 km induce the greatest form drag. Consequently, recent models of the Archipelago, with resolutions of $\sim$2–4 km, may resolve some form drag. Care is needed if inferring drag from such simulations as results can be

strongly resolution dependent. Niwa and Hibiya (2011), for example, found that the conversion of barotropic to baroclinic tidal energy increased exponentially as their grid spacing reduced from 1/5° to 1/15°.

Evidently, quantifying drag in the cases of purely tidal flow or purely mean flow is challenging. Combining the two introduces additional challenges. For example, Staalstrøm et al. (2015) note a highly nonlinear coupling between the two energy sources in Oslofjord with no clear way to separate the two, even in their arguably simple geometry of an approximately constant width channel with a steep sill. The presence of mean currents may also change a flow's hydraulic character, pushing it under or above the threshold of criticality. An example is observed at Stonewall Bank on the Oregon shelf by Nash and Moum (2001) who note the consequent temporal intermittency of the effective drag and mixing coefficients.

1.5 Processes near constrictions

Flow through or over constrictions is intriguing for several reasons: it may constrain exchange between larger bodies of water, it may enhance mixing and drag, and its dynamics has well-established, effective theories. The archetypal constrictions used in the theories are shallow obstacles or narrow channels separating two reservoirs each containing one or two density layers. If sufficiently small, the constriction will exert a hydraulic control, decoupling flow up and downstream. In such cases, the large-scale flow is described by a small set of parameters, thereby simplifying interpretation and prediction of subsequent changes.

The simplest theories consider one or two active, depth-averaged layers in a single along-channel coordinate (e.g., Armi, 1986; Baines, 1995). The theories are nevertheless applicable in certain settings such as the Strait of Gibraltar and the Bosphorus (Armi and Farmer, 1985; Gregg and Özsoy, 2002). These theories can be extended to include Coriolis in idealized geometries. Typically, rotation acts to reduce the total transport (Pratt and Lundberg, 1991). Analytical solutions quickly become intractable, however, when moving beyond idealized geometries. Nevertheless, the concepts of hydraulic control and maximum exchange remain useful, intuitive aids to understanding (Garrett, 2004). For

example, by mapping where flow is supercritical near a sill within the Strait of Gibraltar using a numerical model, Sánchez-Garrido et al. (2011) was able to characterize the overall tidally-driven flow as transient between crest-controlled and approach-controlled flow (see Lawrence, 1993).

Recently, theories have been developed with the aid of numerical models to establish the fate of barotropic tidal energy near constrictions. Of particular interest is how much energy dissipates locally relative to the total energy extracted. However, a consensus on the main influences on this fraction remains elusive (e.g., Staalstrøm et al., 2015; Arneborg et al., 2017). Perhaps unsurprisingly, many studies identify local factors as playing key roles. Examples include interactions between baroclinic trapped waves and the surface tide (Musgrave et al., 2017) or the presence of parallel ridges within which internal tides can interfere or resonate (Buijsman et al., 2012, 2014).

The Archipelago is far removed from a simple geometry: most channels are hydrodynamically wide, channels join at various angles, and the coastline is seldom straight. A somewhat analogous setting occurs in the Samoan Passage at the bottom of the Pacific Ocean. Despite the depth differences, a statement by Alford et al. (2013, paraphrased here) regarding these deep passages is pertinent to the Archipelago: *the water emanating from the channels is the integral over all turbulent processes over each of the possible pathways and accurate parameterization requires understanding (at least in a statistical sense) of the processes and pathways*. Processes that are expected to play a role in the channels in the Archipelago include internal waves, topographically induced eddies, and buoyant coastal currents. These and other sources and sinks of energy are summarized in Figure 1.7.

Internal tides are a special class of internal waves. In Figure 1.7, they are identified parenthetically as Kelvin waves, alluding to the fact that internal tides behave differently poleward of the critical latitude where tidal and Coriolis frequencies are equal. As will become evident in Chapter 4, studies of tidal dynamics from lower-latitudes are relevant to this thesis, but additional complications must be considered.

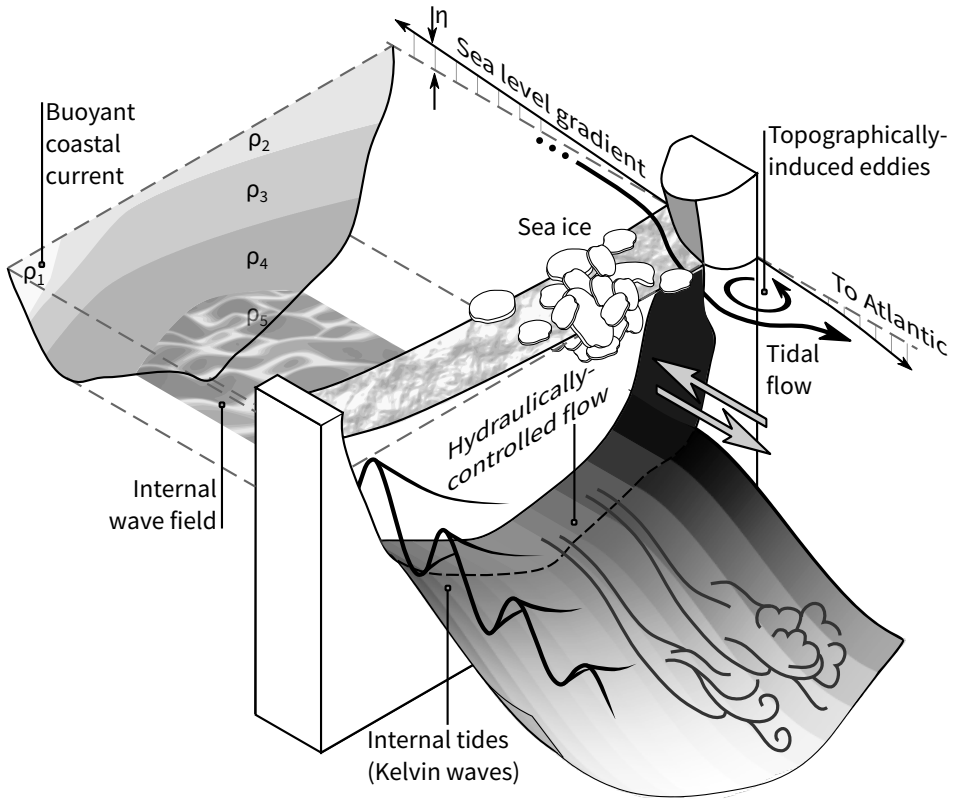

Figure 1.7 – Phenomena within channels of the Archipelago.

1.6 Mixing over rough topography

Enhanced dissipation and mixing above rough topography is a cliché in oceanography, but for a reason. Dissipation rates, for example, may be four orders of magnitude larger than background levels (Gregg et al., 1999; Klymak et al., 2012). Given that it is feasible to describe the whole Archipelago as topographically rough, what mixing rates are induced? and what is the lateral extent of enhanced mixing? Unfortunately, few studies are currently available to provide any quantitative estimates of mixing. Analogous settings, however, may provide guidance.

Inlets, tidal channels, canyons, fracture zones, and continental shelves each share some similarities with the Archipelago in that they are shallow, constricted, or home to fast currents. Using published estimates from such sites, Figure 1.8 shows that a wide range of diffusivities and dissipation rates exists. Indeed, a

challenge in creating such a figure is to decide what constitutes a reasonable range of values for each site. Figure 1.8 should be understood to represent typical values rather than an exact range. Some publications explicitly state a single value, in which case this value is used in place of a range. In some cases, however, this single value may not be representative of the mean but rather the maximum value as studies tend to promote the evocative, larger values observed.

The two studies with the largest range in dissipation values (Klymak and Gregg, 2004; Staalstrøm et al., 2015) are similarly sized fjords with measurements taken in the vicinity of a sill. In both cases, the large range arises because dissipation is enhanced by orders of magnitude due to hydraulic processes over the sill. Moving a couple of kilometres away from the sill, the dissipation reverts back to near-background values. A similar horizontal scale over which mixing decayed was found for shear-generated billows in Admiralty Inlet (Seim and Gregg, 1994).

Hydraulic jumps also occur in the deep ocean (Ferron et al., 1998; St Laurent and Thurnherr, 2007; Alford et al., 2013). A noticeable difference to the fjord studies, however, is that enhanced dissipation now tends to decay over a much longer horizontal scale (50–100 km). In these settings, the dissipation is weak relative to the fjords, but diffusivities are nevertheless large due to the low stratification.

Along with spatial variability, temporal variability plays an important role in the ranges of observed dissipation or diffusivity. Gregg et al. (1999), for example, describes 4–5 hour-long periods of enhanced mixing on the New England Shelf owing to passing internal solibores. Similarly, Marsden et al. (1994b) and Crawford et al. (1999) both identify tidally driven processes such as high-frequency internal waves as the causes of intermittently strong mixing. Indeed, the importance of tides in general is highlighted by a comparison between the diffusivities for the sites with the strongest and weakest tidal currents in the figure: a value of 10^{-3}–$10^{-1}\,\mathrm{m^2\,s^{-1}}$ occurs in Cordova Channel due to currents up to $1\,\mathrm{m\,s^{-1}}$ (Lu et al., 2000), whereas a value of 10^{-6}–$10^{-5}\,\mathrm{m^2\,s^{-1}}$ occurs in the approximately tideless Bosphorus (Gregg et al., 1999).

The lower values in Figure 1.8 typically occur when hydraulic or high-frequency processes are not observed. In such cases, the mixing is primarily attributed to shear as in Viscount Melville Sound and the Florida Strait (Melling et al., 1984;

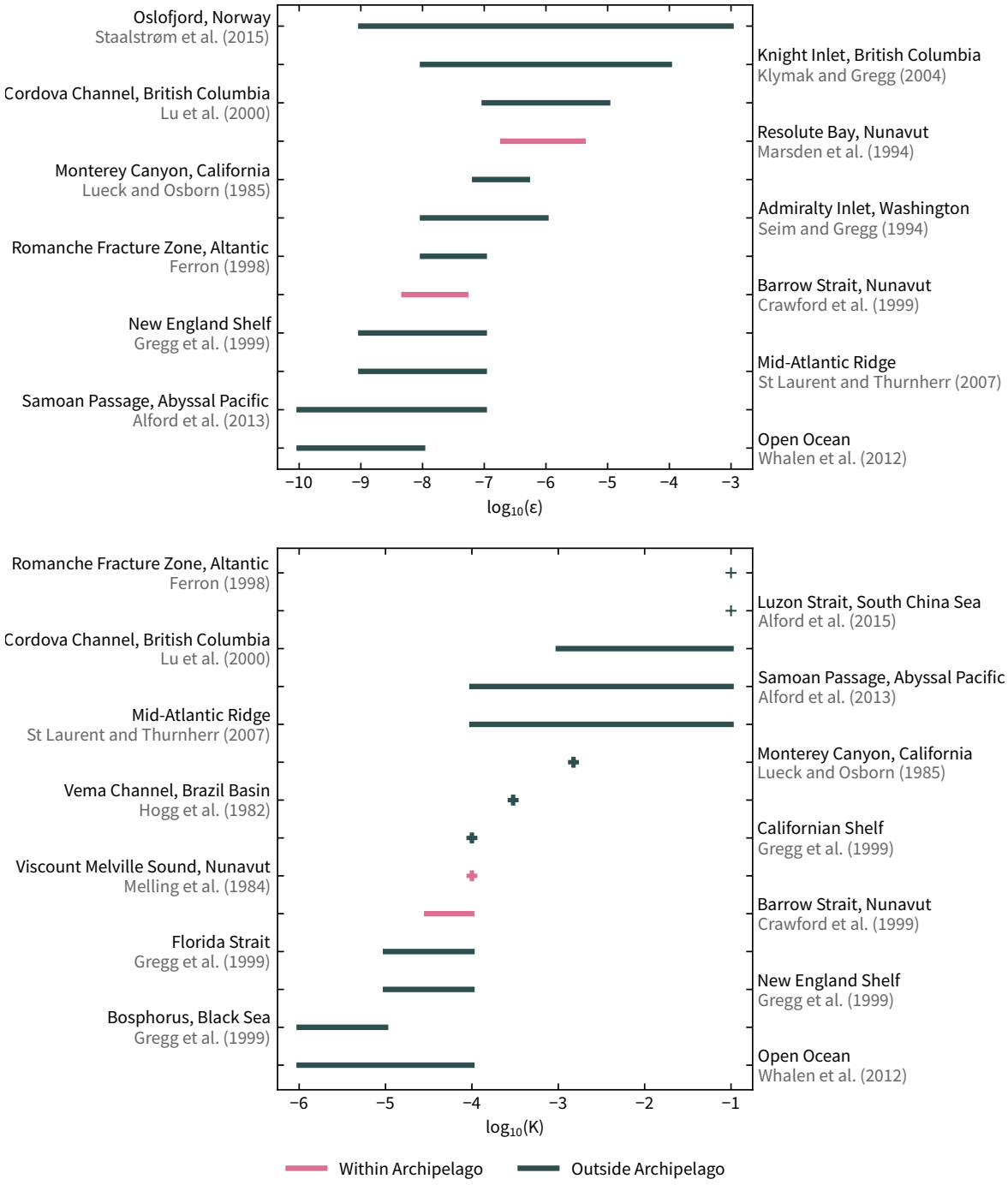

Figure 1.8 – Mixing metrics from shallow, constricted, or topographically complex sites. Crosses indicate that a single value was explicitly stated in the publication. Horizontal lines indicate a typical range.

Gregg et al., 1999) or breaking internal waves as in the open ocean.

1.7 Structure of this thesis

This thesis analyzes small-scale ocean dynamics in the Archipelago in three distinct and complementary ways. Given that a primary aim of this work is to inform large-scale models, Chapter 2 investigates such a model. The overarching question addressed in this chapter is how well mixing and water mass modification are simulated by a model that does not feature tides nor adequately resolve many processes that ultimately lead to mixing.

The influence of tides is clearly evident in Chapter 3, which describes and discusses a new high-spatial-resolution observational dataset. Processes directly observed include an internal hydraulic jump modulated by the tide and an internal tide propagating beside a large island. These are compared to other inferred energy sources and sinks such as large incoming barotropic tidal energy fluxes and strong bottom boundary layer dissipation.

The internal Kelvin wave, being a significant component of the observationally constrained energy budget, proves worthy of further study (Chapter 4). Even in the idealized case of a single obstacle in a rectangular channel, internal wave interference arises. As well as the Archipelago, the results of this idealized study are shown to be important to Arctic fjords.

Chapters 2, 3, and 4 each correspond to studies published or submitted as stand-alone papers. Therefore, Chapter 5 ends the thesis by noting how the respective conclusions from the other chapters tie together and provides advice for future study.

Chapter 2

Water mass modification and mixing rates in a 1/12° simulation

Abstract

Strong spatial differences in diapycnal mixing across the Canadian Arctic Archipelago are diagnosed in a $1/12^\circ$ basin-scale model. Changes in mass flux between water flowing into or out of several regions are analyzed using a volume-integrated advection–diffusion equation, and focus is given to denser water, the direct advective flux of which is mediated by sills. The unknown in the mass budget, mixing strength, is a quantity seldom explored in other studies of the Archipelago, which typically focus on fluxes. Regionally averaged diapycnal diffusivities and buoyancy fluxes are up to an order of magnitude larger in the eastern half of the Archipelago relative to those in the west. Much of the elevated mixing is concentrated near sills in Queens Channel and Barrow Strait, with stronger mixing particularly evident in the net shifts of the densest water to lower densities as it traverses these constrictions. Associated with these shifts are areally averaged buoyancy fluxes up to $10^{-8}\,\mathrm{m^2\,s^{-3}}$ through the $1027\,\mathrm{kg\,m^{-3}}$ isopycnal surface, which lies at approximately 100 m depth. This value is similar in strength to the destabilizing buoyancy flux at the ocean surface during winter. Effective diffusivities estimated from the buoyancy fluxes can exceed $10^{-4}\,\mathrm{m^2\,s^{-1}}$, but are often closer to $10^{-5}\,\mathrm{m^2\,s^{-1}}$ across the Archipelago. Tidal forcing, known to modulate mixing in the Archipelago, is not included in the model. Nevertheless, mixing metrics derived from our simulation are of the same order of magnitude as the few comparable observations.

Published as

Hughes K.G., J. M. Klymak, X. Hu, and P. G. Myers (2017) Water mass modification and mixing rates in a 1/12° simulation of the Canadian Arctic Archipelago. *J. Geophys. Res.*, 122, 803–820, doi:10.1002/2016JC012235

2.1 Introduction

The Canadian Arctic Archipelago is one of two conduits for outflow of cool, low-salinity water from the Arctic Ocean to the North Atlantic. Water in these channels (Figure 2.1) flows at a net rate of order 1 Sv (Prinsenberg et al., 2009), with velocities within the channels predominately governed by four factors: sea level gradient, wind, tidal currents, and buoyant boundary currents. Both modelling and observational studies agree that seasonal and interannual variability of net volume transport though the Archipelago is driven by sea level differences between the Beaufort Sea and Baffin Bay (e.g., Peterson et al., 2012; McGeehan and Maslowski, 2012; Lu et al., 2014). Sea levels in the Beaufort Sea are primarily controlled by the wind regime, while those in Baffin Bay are linked to air–sea heat exchanges in the Labrador Sea (Houssais and Herbaut, 2011). Indeed, Hu and Myers (2014) predict a significant decrease to the flux through Parry Channel in the coming century due to lifting of the sea surface in Baffin Bay. On daily and weekly time scales, tidal currents are responsible for much of the velocity variance (Prinsenberg and Bennett, 1989). In many places, root-mean-square currents exceed $0.1\,\mathrm{m\,s^{-1}}$ and peak velocities exceed $1\,\mathrm{m\,s^{-1}}$ (Hannah et al., 2009). These channels also have strong buoyant currents (0.1–$0.4\,\mathrm{m\,s^{-1}}$) that oppose the mean flow, narrowly confined to the northern and eastern sides of the channels by geostrophy. Currents far from the boundary (>15 km) are weak.

To date, most studies of the Archipelago have focused on the two main channels: Parry Channel, which runs approximately east–west and provides an exit for Pacific Water that passed through Bering Strait, and Nares Strait, which is perpendicular and contains a significant component of Atlantic Water (Münchow et al., 2007). The "central sills area" north of Parry Channel has seen less study, likely a combination of its remoteness, short ice-free season, and smaller volume fluxes. Nevertheless, the complex topography and strong tidal currents in this area have implications for water ultimately leaving the Archipelago.

Several observations point to the central sills area as a key location within the Archipelago with respect to mixing. Point measurements from the early 1980s show significant slopes in the isohalines in both directions toward Penny Strait, with isohalines from 70–80 m deep in northern Archipelago outcropping at the surface (de Lange Boom et al., 1987). Similarly, during these studies in the 1980s

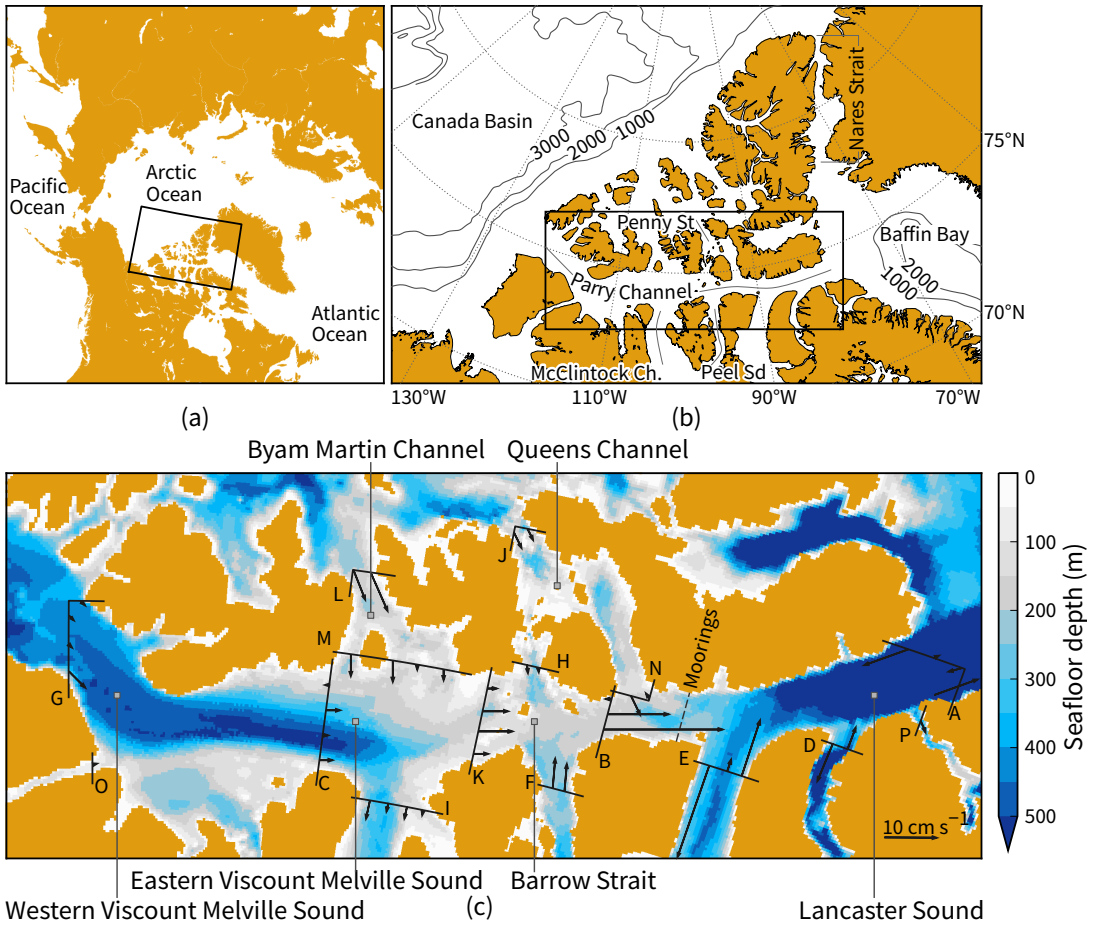

Figure 2.1 – Location and bathymetry of the Canadian Arctic Archipelago. (b) Enlargement of the region outlined in panel a. (c) Coastline and bathymetry in the model configuration for the region outlined in panel b. In this chapter the Archipelago is divided into six named regions demarcated by the sixteen labelled cross sections. Sections lie along the model grid, hence the need for corners in some sections, and arrows represent the net along-channel velocity. Here we denote the upper central part of panel c as the ''central sills area''.

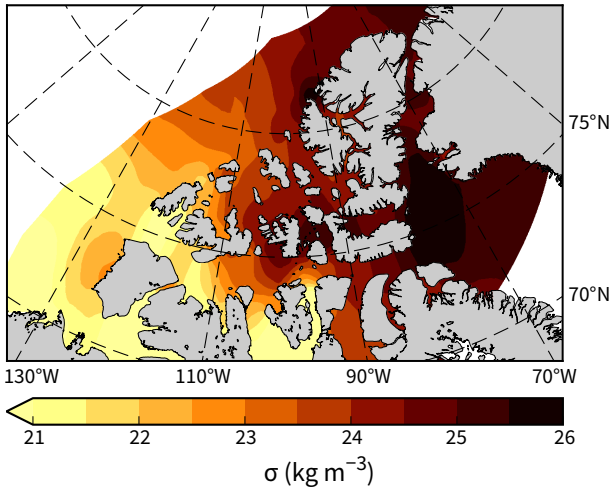

Figure 2.2 – Surface density anomaly across the Archipelago. Contours are calculated using surface temperature and salinity from the climatology produced by Kliem and Greenberg (2003), which is centred around the time of minimum ice coverage. Note the denser water in the central channels.

and prior, Penny Strait and Queens Channel were consistently observed to have the highest surface salinity within the Archipelago. Based on the climatology of Kliem and Greenberg (2003), a maximum in surface density also occurs in this region (Figure 2.2). Another indicator of strong mixing is a local minimum in sea ice coverage. Additional heat bought to the surface by diapycnal mixing is manifest through visible and invisible polynyas (Melling et al., 2015), which are ice-free or thin ice regions, respectively. Satellite images identify a number of sites in the central sills area where polynyas consistently occur or ice breaks up comparatively early.

A number of physical processes cause elevated mixing within the Archipelago. These include wind, convection, shear instabilities, breaking large-amplitude internal waves, and boundary layers at the seafloor and ice–ocean interface. Both Marsden et al. (1994a) and Crawford et al. (1999) observed large, but short-lived, peaks in dissipation due to passing internal waves. Marsden et al. (1994b) attributed the observed near-surface internal waves to interaction of tidal flow with nearby ridged ice. These waves were necessary to create sufficient shear to induce mixing in the pycnocline. Below the pycnocline but away from the seafloor, active mixing events identified by enhanced dissipation rates have

been observed over a range of depths (Crawford et al., 1999). These shear-induced events had vertical scales of 10–20 m. Near the seafloor in Barrow Strait, Prinsenberg and Bennett (1987) observed bottom mixed layers up to 50 m thick. All of these studies conclude that mixing is tidally modulated, with turbulence more energetic during spring tides. This is most apparent in the surface mixed layer and the pycnocline.

The complexity of the Archipelago limits the generalizability of these mixing studies to other locations or time periods. Consequently, there is a lack of quantitative mixing estimates with which spatial and/or seasonal variability can be discerned. Such estimates would complement the many existing studies concerned with freshwater and volume fluxes through the Archipelago. Identifying where water mass modification occurs allows for a more complete conceptual understanding of throughflow in the Archipelago. Additionally, it suggests where to focus effort for further targeted mixing studies.

In this chapter, we use a $1/12^\circ$ resolution model run for 2002–2010 (Section 2.2). We analyze simulated volume fluxes, density structure, and sea ice conditions (Section 2.3) insofar as necessary to explain mixing variability. Then, by using cross sections to demarcate six contiguous regions of the Archipelago, we estimate mixing strength across the Archipelago and how this changes with season and location (Section 2.4). Our estimates focus on waters with potential densities equal to or greater than $1027\,\mathrm{kg\,m^{-3}}$, which is the approximate mean density of Pacific Water in the Canada Basin. These waters typically lie below 100 m meaning that direct advective flux of their properties across the Archipelago is limited by sills such as those in Penny Strait (80 m) and Barrow Strait (125 m). They also seldom experience direct ventilation during winter convective mixing. Last, we consider the validity of our estimates, the implications for water mass modification, and the causes of mixing variability (Sections 2.5 and 2.6).

2.2 Model description

The model configuration used in this study, the Arctic and Northern Hemisphere Atlantic $1/12^\circ$ (ANHA12), uses the Nucleus for European Modelling of the Ocean (NEMO; Madec and the NEMO team, 2008) version 3.4 framework coupled with

the Louvain-la-Neuve (LIM2; Fichefet and Morales Maqueda, 1997) sea ice model with an elastic-viscous-plastic rheology. The ocean model is three-dimensional and hydrostatic with a free surface. In the vertical, 50 z-levels are used along with partial steps. Horizontally, the grid consists of 1632×2400 grid points and contains the whole Arctic Ocean (with Bering Strait at the boundary) and the Atlantic Ocean as far as 20°S. Within the Archipelago, the model has a resolution of $\sim$4 km. Typical channels contain 10–20 grid cells in the across-channel direction and 20–25 vertically. Consequently, the model has the ability to resolve, or at least permit, buoyant coastal currents within the channels. Such currents are ubiquitous in the Archipelago and constitute much of the component of flow toward the Arctic.

Vertical mixing of tracers within the model is treated using a turbulent kinetic energy (TKE) closure scheme. The diffusivity coefficients are computed based on a prognostic equation for TKE and an assumption about the turbulent length scales. The prognostic equation includes production by vertical shear, and reduction by stratification, vertical diffusion, and dissipation (see Madec and the NEMO team (2008) for further details). A minimum vertical diffusivity of $10^{-6}\,\mathrm{m^2\,s^{-1}}$ is applied to avoid numerical instabilities associated with weak vertical diffusion. Conversely, where the water column is unstable or neutrally stable (buoyancy frequency of less than $10^{-6}\,\mathrm{s^{-1}}$), the vertical diffusivity is set to $10^{1}\,\mathrm{m^2\,s^{-1}}$.

Lateral mixing in the model is calculated along isoneutral surfaces, reducing horizontal diffusion across tilted isopycnals. The harmonic diffusivity is grid-size-dependent with a maximum of $50\,\mathrm{m^2\,s^{-1}}$, but is approximately $20\,\mathrm{m^2\,s^{-1}}$ within the Archipelago. We expect overly diffusive downslope flows as no bottom boundary layer scheme was included (e.g., Beckmann and Döscher, 1997). Note that these mixing parameters were chosen before this study was proposed.

ANHA12 was run for 2002–2010 with initial and boundary conditions given by the global ocean reanalysis and simulation (GLORYS1v1) (Ferry et al., 2010) and an early version of the Canadian Meteorological Centre's global deterministic prediction system reforecasts (CGRF) atmospheric forcing, including uncorrected precipitation fields (Smith et al., 2013). No tidal forcing is included. Five-day means of a range of quantities for each grid cell are saved, and our analysis focuses on density and velocity in six regions demarcated by sixteen cross-sections

within the Archipelago. The names used to refer to these six regions throughout the text are given in Figure 2.1c.

2.3 Simulated hydrography

2.3.1 Flow structure and fluxes

Qualitatively, ANHA12 simulates the expected average flow structure within the Archipelago: strong coastal flows superimposed on a generally southward and/or eastward flow. This is evident in the along-channel velocities at each cross-section averaged over the entire simulation period (Figure 2.3). With the fluxes displayed in this manner, it is clear that much of the toward-Atlantic flow (red) is composed of barotropic coastal flows on the south or west sides of channels. Conversely, the toward-Arctic flow (blue) is much weaker and often away from the surface. Such flow structure is observed in mooring data from western Lancaster Sound (Prinsenberg et al., 2009, see Figure 2.1c for mooring location). Indeed, Peterson et al. (2012) note that flow through this region is adequately monitored by measuring flux through only the southern half of the channel.

Section F (Peel Sound) is noteworthy as it has a net northward flow. This results from the sill in western Barrow Strait (97°W) steering flow southward through McClintock Channel, with this flow then returning northward to join the eastward flow through Parry Channel (e.g., Wang et al., 2012).

Within the channels, a simple measure of the relative importance of barotropic and baroclinic forcing is to consider the positive and negative components of the net flux. Figure 2.4 shows volume flux partitioned by sign of along-channel velocity for water entering and exiting the entire Parry Channel (panels a–b), the centre of Parry Channel (panels c–d), and the central sills area (panels e–f). Of these sites, those in the centre of the Archipelago show minimal exchange flow for most times of the year (panels c–f). Typically the toward-Arctic component is an order of magnitude smaller than the net flux at these central sites. Nevertheless, there is a clear negative correlation between the flux components: the toward-Arctic flux is maximum when the toward-Atlantic flow is minimum. This suggests that the toward-Arctic flow is masked by the stronger overall toward-Atlantic flow. A

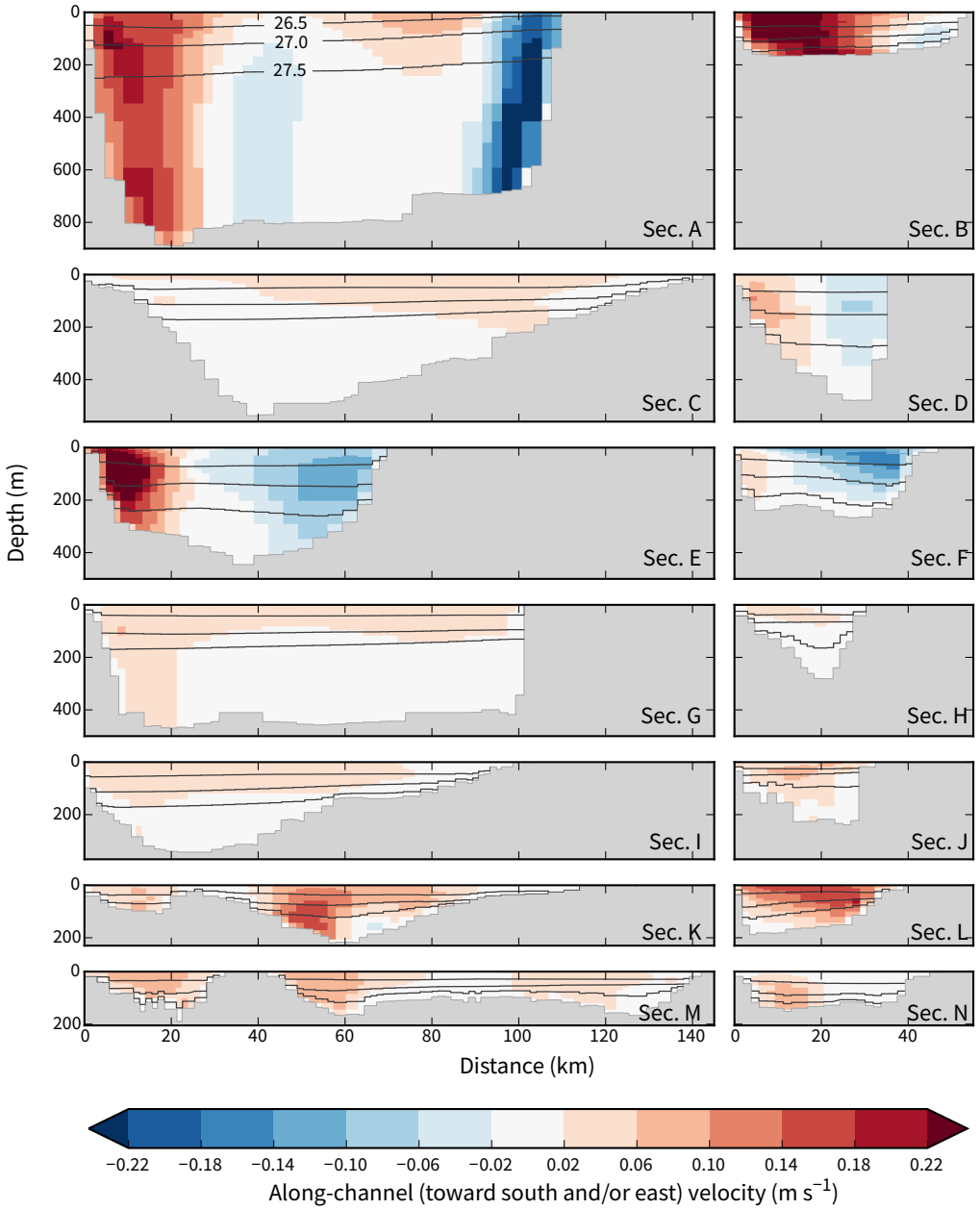

Figure 2.3 – Simulated cross-sectional flow structure. Velocities are the mean over the whole simulation period (2002–2010) and density contours are the mean depths of the $\sigma_\theta = 26.5, 27.0$, and $27.5\,\mathrm{kg\,m^{-3}}$ isopycnals. In all panels, the southern or western coast is on the left hand side. See Figure 2.1c for section labels and note that for sections with a corner, we present velocities interpolated along a straight line between the ends of the section. Sections O and P, each only five grid cells wide, are not shown.

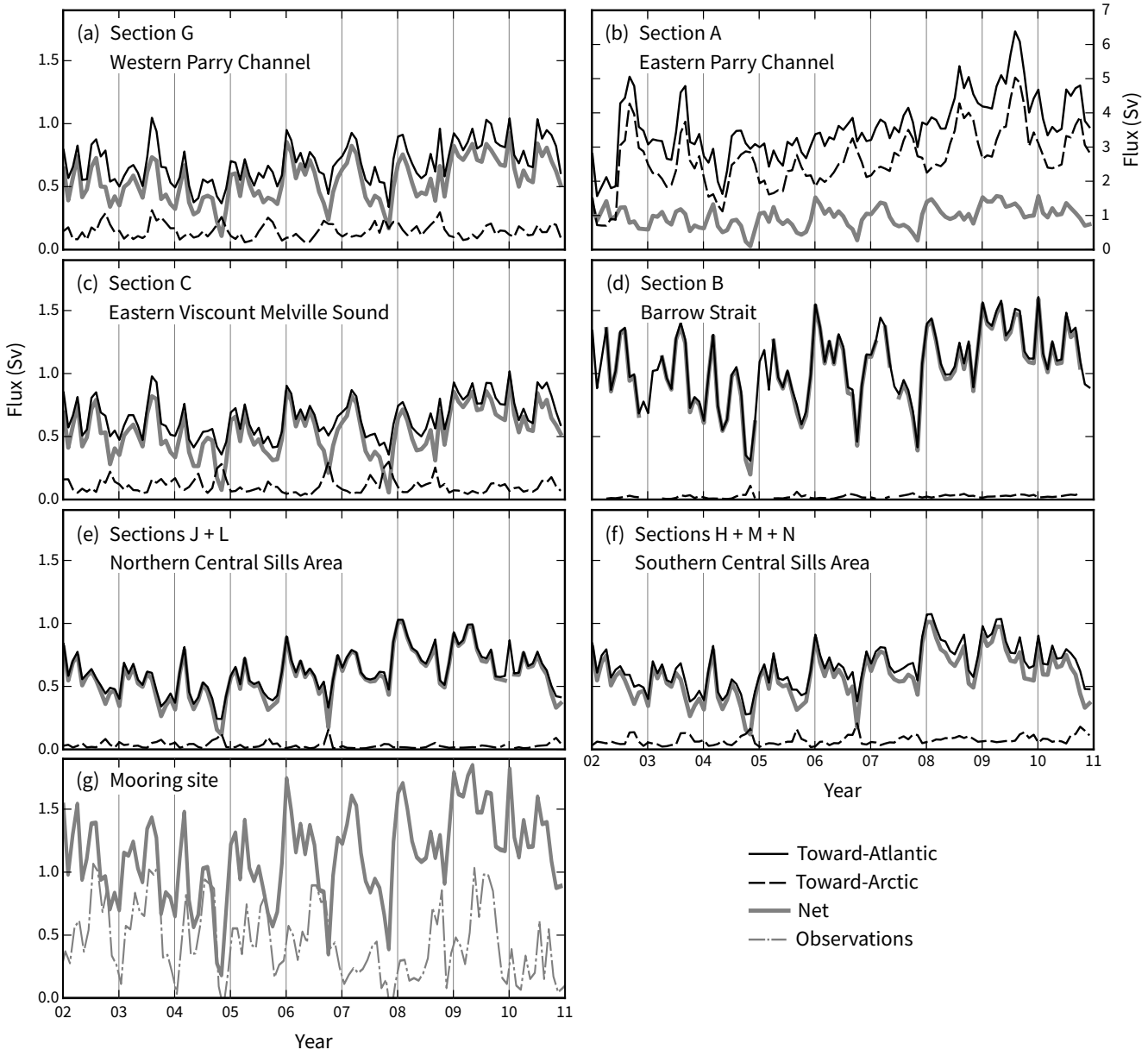

Figure 2.4 – Simulated fluxes at various sections throughout the Archipelago partitioned by along-channel velocity. Note that a different y-axis is used for section A. Panel g provides simulated fluxes at the mooring transect (Figure 2.1c) to compare against observations (Peterson et al., 2012).

stronger exchange flow can therefore be expected in years with a smaller overall sea level difference.

The timing of the peak in toward-Arctic flux, which occurs in early autumn, agrees well with the aforementioned mooring data. There is also some agreement between these data and the simulated net flux at the location of the moorings (Figure 2.4g). The agreement is better for the first three years of simulation. Thereafter the simulated fluxes are noticeably larger. This is related in part to issues with the interpolation of runoff onto the model grid, which has been fixed for future experiments. Overestimates of a similar magnitude are also simulated by Wekerle et al. (2013) and Lu et al. (2014). Note also that our simulation suggests large fluxes in the early months of the year, whereas observations suggest a minimum at this time. An early peak flux is also simulated by McGeehan and Maslowski (2012) who discuss several reasons for the discrepancy, in particular that flow in the northern half of the channel is given too little weight in estimates of net flux from moorings. Indeed, in mid-2006, the two northernmost of the four moorings in Barrow Strait were removed (Peterson et al., 2012). There is a noticeable difference in the mean net flux observed before and after this time.

Flux through eastern Lancaster Sound (Section A, Figure 2.4b) is noticeably different from the other sections in that the toward-Arctic component is stronger than the net flow. This flow results from a strong coastal current from Baffin Bay that recirculates in the mouth of the Sound (e.g., Prinsenberg et al., 2009; Wang et al., 2012). The coherent inflow and outflow regions dominate the velocities for this section (Figure 2.3a). Remnants of the inflow can be identified in Wellington Channel (Figure 2.3n; see also de Lange Boom et al. 1987), but the current significantly weakens during its 300–400 km transit along the northern side of Lancaster Sound.

The seasonal cycles of net flux through each of the sections correlate strongly with each other, with the highest fluxes at or just after the new year and the lowest fluxes late in the year. To some extent, this correlation is expected as sections are not independent. Nevertheless, that the north–south and east–west fluxes correlate strongly agrees with previous studies that note that flow through individual channels is primarily driven by the same large-scale atmospheric forcing (Houssais and Herbaut, 2011; Wekerle et al., 2013).

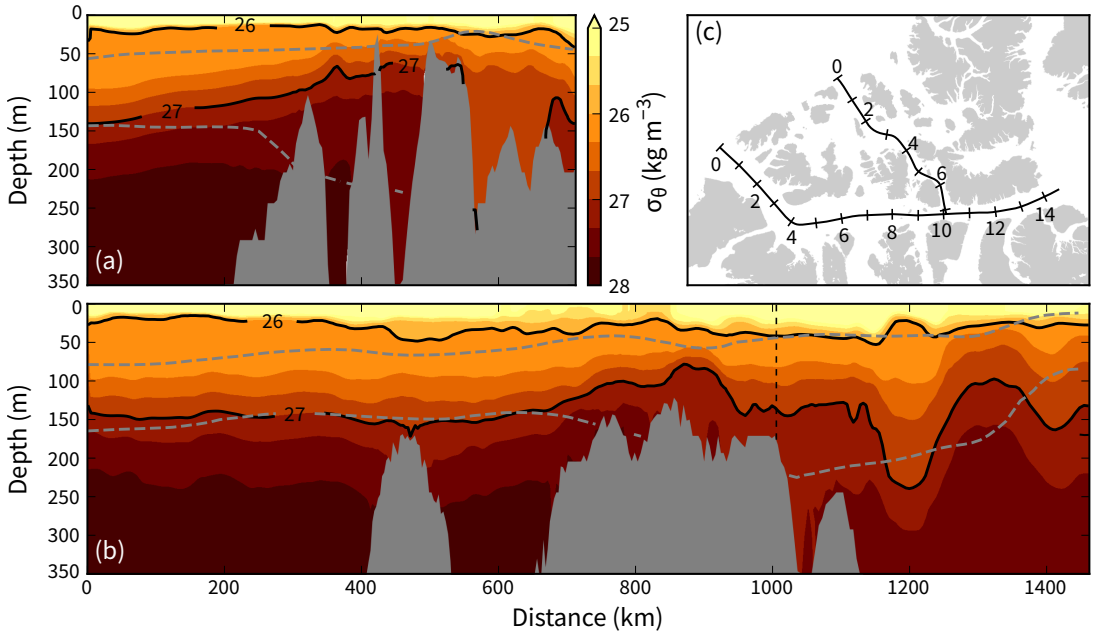

Figure 2.5 – The potential density field in early September 2003 through (a) the northern Archipelago and (b) Parry Channel. Dashed, grey contours show the 26 and 27 kg m^{-3} isopycnals calculated from the climatology produced by Kliem and Greenberg (2003). (c) Distances in multiples of 100 km. The final 35 km of the northern transect lie within Parry Channel and the vertical dashed line indicates the intersection of the two transects.

2.3.2 Density structure

The density structure across the Archipelago (Figure 2.5) highlights the importance of processes that transport properties vertically, especially for water at depth. The centre of the Archipelago is shallower than the areas to the west, north, and east. Consequently, distinct differences exist in the density structure at depth depending on location within the Archipelago. In both Parry Channel and the northern Archipelago, isopycnals of 27 kg m^{-3} or more occur noticeably higher in the water column on the western or northern sides of the transect. Buoyancy fluxes up through these isopycnals influence how strongly water properties are communicated across the Archipelago.

North of the shallow sills in Queens Channel, isopycnals slope upward toward the south. This is consistent with the isohalines shown by Fissel et al. (1984, their Figure 21) along a very similar transect taken in March–April 1983. Similarly, isohalines from their transect through Parry Channel (their Figure 18) are

consistent with the simulated field shown in Figure 2.5b. These authors attribute the reduced salinity, and hence density, in the east to the influence of Baffin Bay Atlantic Water in place of Canada Basin Atlantic Water. Note that below approximately 200 m, water in Baffin Bay is fresher than in the Canada Basin and vice versa above.

A comparison between the modelled density field and a climatology centred on September 1 is given for two isopycnals in Figure 2.5. This climatology is calculated from sparse data, especially in the northwest (see Figure 3 of Kliem and Greenberg (2003)), and does not account for sills separating water masses. Consequently, it cannot capture the upward tilt in $27\,\mathrm{kg\,m^{-3}}$ isopycnal at 0–500 km in Figure 2.5a. The depth of this contour at each end of the transect, however, is reasonable. Similarly, the depths of climatological and modelled isopycnals broadly agree throughout Parry Channel (Figure 2.5b). Although the fields shown in Figure 2.5 represent data at only one time, the picture remains similar throughout the simulation. Typical interannual variation of the depth a given isopycnal is 10–20 m.

2.3.3 Sea ice conditions

A thorough description of sea ice conditions is provided by Hu et al. (2018) and outside the scope of this study as it will have at most a minor influence here given our focus on deeper waters. Consequently, we review only briefly the simulated conditions. We also note that despite suggestions of enhanced mixing through ice–current interactions (Section 2.1), sea ice typically acts to inhibit mixing by reducing momentum transfer from the atmosphere (e.g., Rainville et al., 2011).

For 8–10 months of the year, sea ice coverage is 80–100% throughout the Archipelago. The thickest ice (4–5 m) occurs at the northern and western boundaries. Here, ice thickens dynamically as it approaches the many islands. The thinnest ice (0–2 m) occurs at the outlets to Baffin Bay, where the ice undergoes large seasonal variations. Simulated ice thickness within the Archipelago and over the continental shelf to the northwest agrees well with IceBridge (airborne laser altimetry), ICESat (satellite lidar), and drilled thickness observations (Lindsay, 2013).

2.4 Mixing rates throughout the Archipelago

Prior knowledge of the hydrography throughout the Archipelago (Section 2.1) suggests there is variation across the Archipelago with respect to mixing levels, with the strongest mixing expected in the central sills area. By quantifying mixing in different regions of the Archipelago, we will estimate the magnitude of this variation. In doing so, we also ascertain the fate of water transiting the Archipelago. For example, dense water may flow through the channels unchanged or may completely mix with the water above.

2.4.1 Inverse estimates of diapycnal diffusivity and buoyancy flux

Analysis of changes in transport as a function of density between the incoming and outgoing flows in a channel allows estimates of diapycnal diffusivities and buoyancy fluxes. Here we estimate these quantities (i) spatially averaged over the region enclosed by cross sections and (ii) temporally averaged over monthly time scales.

Conceptually, the method is encapsulated in Figure 2.6a. Assume a well-stratified flow enters the left end of the channel and that total transport is spread somewhat evenly amongst all densities ($Q_1^{\text{in}} \approx Q_2^{\text{in}} \approx Q_3^{\text{in}}$). Mixing within the channel causes the least and most dense layers to mix with the middle density layers. Consequently, transport out of the channel is dominated by middle density water ($Q_2^{\text{out}} > Q_1^{\text{out}}, Q_3^{\text{out}}$). For flow within the Archipelago, this concept needs to be extended to three-dimensional flow to allow for lateral variation in flow direction (Figure 2.6b). Specifically, the inward and outward fluxes no longer correspond with one end of the channel each (Figure 2.6c). Not demonstrated in Figure 2.6 is the potential for the total mass within the channel to change due to a flux of, say, denser water that is then stored within the channel rather than being mixed upward.

Mathematically, the method uses the advection–diffusion equation for mass within a variable volume V:

$$\frac{\mathrm{d}}{\mathrm{d}t}\int_V \rho_\theta \,\mathrm{d}V + \int_V \nabla\cdot(\rho_\theta \mathbf{u})\,\mathrm{d}V + F = \int_V \nabla\cdot(K\nabla\rho_\theta)\,\mathrm{d}V \tag{2.1}$$

where ρ_θ is potential density, $\mathbf{u}$ is velocity, and K is the diffusivity of density. Any

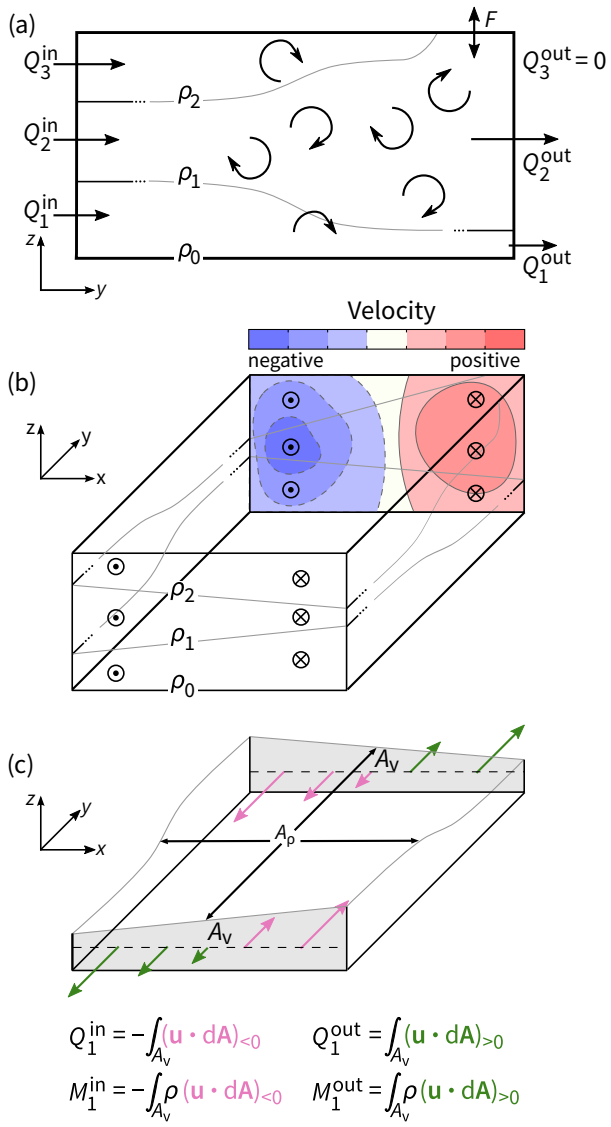

Figure 2.6 – Concept, notation, and scheme used to estimate diapycnal diffusivity. (a) In unidirectional flow within a channel, diapycnal mixing causes isopycnals to slope and causes changes to mass transport as a function of density. (b) Extending the concept from panel a to a three-dimensional, rectangular channel and allowing for lateral differences in flow direction. (c) Definition of the volume Q_1 and mass M_1 fluxes for the densest layer. Subscript '>0' implies only positive values are included in the integration and vice versa, and minus signs for the inward fluxes ensure all fluxes are non-negative.

surface buoyancy exchange due to ice growth and melt and atmospheric and solar forcing is included in F. This term is nonzero when part or all of the upper surface of V coincides with the sea surface; see, for example, the ρ_2 isopycnal in Figure 2.6a. Positive values for F correspond to a stabilizing flux (warming or freshening).

Applying the divergence theorem, Equation 2.1 becomes

$$\frac{\mathrm{d}}{\mathrm{d}t}\int_V \rho_\theta \,\mathrm{d}V + \oint_A \rho_\theta \mathbf{u}\cdot\mathrm{d}\mathbf{A} + F = \oint_A K\nabla\rho_\theta\cdot\mathrm{d}\mathbf{A} \tag{2.2a}$$

$$\approx \int_{A_\rho} K\frac{\partial\rho_\theta}{\partial z}\,\mathrm{d}A_h \tag{2.2b}$$

$$\approx \overline{K}\int_{A_\rho} \frac{\partial\rho_\theta}{\partial z}\,\mathrm{d}A_h \tag{2.2c}$$

where A is the total area enclosing V, A_ρ is the isopycnal surface at the top of the integration volume, and A_h is the projection of A_ρ onto the horizontal plane. The right-hand side is first simplified by noting that the total area through which diffusion occurs is dominated by A_ρ. Further, we rely on the large aspect ratio of the volume V to use the vertical density gradient in place of its diapycnal counterpart. The second step defines an effective mean turbulent diffusivity $\overline{K}$ through the isopycnal surface. Note that the expression in Equation 2.2b, which is the residual of the three terms on the left hand side, is closely related to the integrated buoyancy flux across the isopycnal surface:

$$\int_{A_\rho} J_\mathrm{b}\,\mathrm{d}A_h = \frac{-g}{\rho}\int_{A_\rho} K\frac{\partial\rho_\theta}{\partial z}\,\mathrm{d}A_h = \int_{A_\rho} KN^2\mathrm{d}A_h \tag{2.3}$$

where J_b is buoyancy flux in units of $\mathrm{m^2\,s^{-3}}$ (or equivalently $\mathrm{W\,kg^{-1}}$) and N is the buoyancy frequency.

The continuity equation provides a link between three quantities, two of which are derived directly from the model: the net flux through the vertical sides of the volume and the rate of change of the volume V beneath the isopycnal surface. The difference between these gives the advective flux through the isopycnal

surface:

$$\int_{A_\rho} \mathbf{u} \cdot \mathrm{d}\mathbf{A} = -\int_{A_v} \mathbf{u} \cdot \mathrm{d}\mathbf{A} - \frac{\mathrm{d}V}{\mathrm{d}t} = (Q_1^{\text{in}} - Q_1^{\text{out}}) - \frac{\mathrm{d}V}{\mathrm{d}t} \tag{2.4}$$

Q_1^{in} and Q_1^{out} are defined in Figure 2.6c.

To summarize our method and make the result more intuitive, we rewrite Equation 2.2c and invoke the notation shown in Figure 2.6c:

$$\underbrace{-(M_1^{\text{in}} - M_1^{\text{out}}) + \rho_1(Q_1^{\text{in}} - Q_1^{\text{out}})}_{\text{horizontal mass divergence}} + \underbrace{\frac{\mathrm{d}}{\mathrm{d}t}\int_{V_1} \rho_\theta \, \mathrm{d}V - \rho_1 \frac{\mathrm{d}V_1}{\mathrm{d}t}}_{\text{mass rate of change}} + F = \underbrace{\overline{K}_1 \int_{A_1} \frac{\partial \rho_\theta}{\partial z} \mathrm{d}A_h}_{\text{diffusive buoyancy flux}} \tag{2.5}$$

The effective diffusivity on any isopycnal is found by selecting a desired isopycnal ρ_1, undertaking the areal and volume integrals, and then solving for $\overline{K}_1$. Note that the various terms are collected such that each of the three braced expressions have comparable magnitude.

The quantities used in Equation 2.5 are all calculated using five-day means: vertical density gradients are evaluated on grid cell faces using finite differences of adjacent density values and the associated depths at the cell centres; rates of change, which stem predominantly from seasonal changes in water masses, are estimated using a central finite difference; and the surface buoyancy exchange F is derived from several mean surface quantities such as heat flux and ice growth rate. By using five-day means, uncertainty is introduced to the left-hand side of Equation 2.5 in two ways. First, advective mass flux and surface buoyancy flux are approximated as the products of means, not the means of products. Second, rates of change will be smoothed estimates of their true values. We reduce the influence of these uncertainties by considering changes on monthly time scales.

2.4.2 Flux versus density

Expressing flux as a function of potential density can demonstrate whether there is strong mixing within a particular region. To do this, we calculate inward and outward fluxes as in Figures 2.6a and 2.6c, with density bins of $0.1\,\mathrm{kg\,m^{-3}}$. The inward fluxes are shown in Figure 2.7 together with the net change (outward − inward). Fluxes were averaged across one year of data to minimize the

effect of seasonal density changes. Results are shown for only 2005, but the other years are qualitatively similar.

For all regions except Lancaster Sound, the average flux into the region is dominated by water with a potential density anomaly of approximately 26.5 $\mathrm{kg\,m^{-3}}$. There is also a significant contribution to the inward flux by dense water (27.5–28.0 $\mathrm{kg\,m^{-3}}$) in the two deepest regions, western Viscount Melville Sound and Lancaster Sound.

Barrow Strait and Queens Channel display a distinct loss of the denser water flowing into the channel, with a corresponding increase in water of slightly lower density. This change is consistent with strong mixing within the channel as shown conceptually in Figure 2.6a. Similar net changes are not as evident in the other four regions, at least relative to the inward flux. This suggests Queens Channel and Barrow Strait will have the strongest mixing rates, but to substantiate this statement we need to evaluate the diffusivity and buoyancy flux.

2.4.3 Regionally averaged mixing

Time series of effective diffusivity in each region are evaluated on 10 isopycnals ($\sigma_\theta = 26.8, 26.9, \ldots, 27.7\,\mathrm{kg\,m^{-3}}$). This range is chosen for three reasons. First, it corresponds to water whose direct advective flux is at least somewhat limited by sills as described in Section 2.3.2. Second, it broadly corresponds to the density range of Pacific Water in the Canada Basin of the Arctic Ocean (Carmack et al., 2008, 2016). Third, it avoids volumes that are strongly influenced by buoyancy flux at the ocean surface. Shallower isopycnals are addressed in Section 2.4.4.

Two results are evident in the time series (Figure 2.8). First, a seasonal cycle is evident in each series. There is also some evidence for interannual variability, but we do not investigate this here given the short simulation length. Second, most diffusivities fall in the range 10^{-5}–$10^{-4}\,\mathrm{m^2\,s^{-1}}$. For comparison, values of this magnitude have been observed in Florida Strait and the New England Shelf, smaller values ($10^{-6}\,\mathrm{m^2\,s^{-1}}$) in much of the water column in the Black Sea Shelf north of the Bosphorus Strait (Gregg et al., 1999), slightly larger values (10^{-4}–$10^{-3}\,\mathrm{m^2\,s^{-1}}$) in Vema Channel in the Brazil Basin (Hogg et al., 1982) and on the shelf near Monterey Canyon, California (Gregg et al., 1999), and much larger values (10^{-3}–$10^{-1}\,\mathrm{m^2\,s^{-1}}$) in other regions of complex topography such as

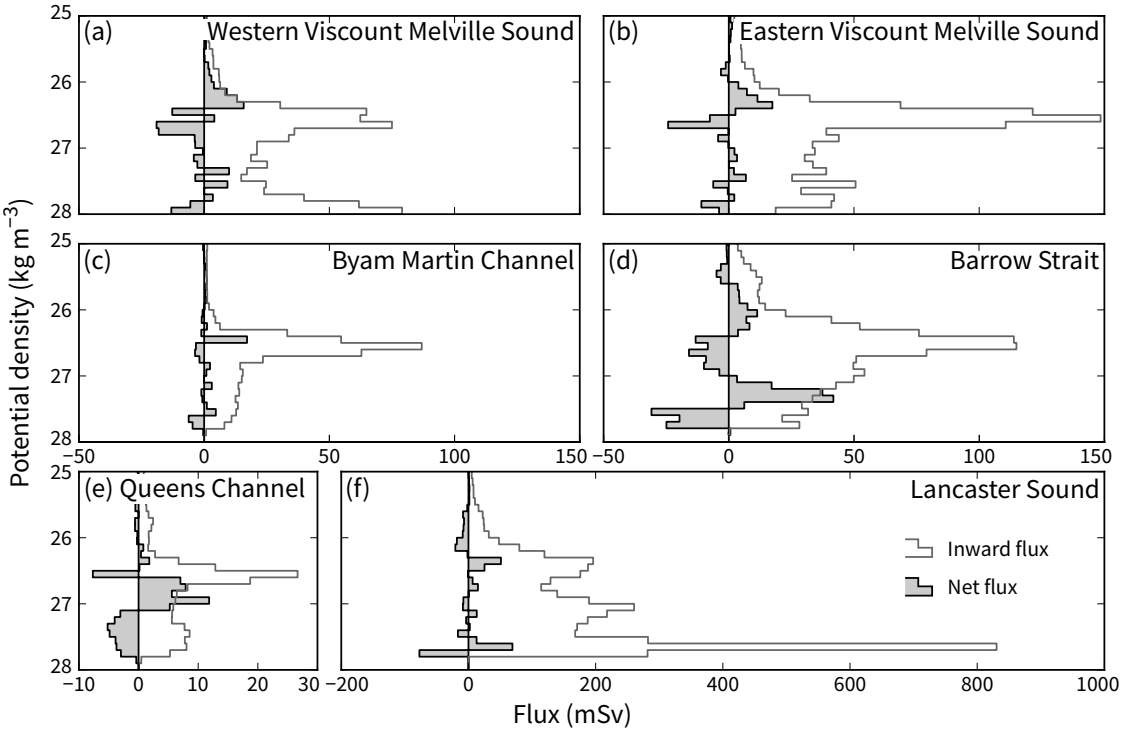

Figure 2.7 – Changes in the composition of volume flux between water flowing into and out of the six regions. Fluxes are an average across a year (2005), potential density bins are 0.1 kg m^{-3}, and a positive net flux for a given density bin signifies that outflow is greater than inflow. Inward fluxes, as defined in Figure 2.6c, are the summed flux for all water with a velocity into the region through any of the bounding cross sections. Note that no water exceeded $\sigma_\theta = 28\,\mathrm{kg\,m^{-3}}$ and flux for water with $\sigma_\theta < 25\,\mathrm{kg\,m^{-3}}$ is insignificant.

the Romanche Fracture Zone in the mid-Atlantic Ridge (Ferron et al., 1998) or Cordova Channel, British Columbia (Lu et al., 2000). Values in the open ocean at mid-depth are typically 10^{-6}–$10^{-4}\,\mathrm{m^2\,s^{-1}}$ (Whalen et al., 2012).

To understand the diffusivities derived, and more generally the fate of the water passing through different channels, we consider the cycles of each of the four terms in Equation 2.5. These terms are shown in Figure 2.9 as volume fluxes for the regions with the smallest and largest diffusivities. In western Viscount Melville Sound, the budget is a near balance between the integrated rate of change of mass and the horizontal mass divergence. For example, if a given mass of dense water is advected into this region, it will tend to move through or be stored within the region with its properties unchanged as opposed to mixing with

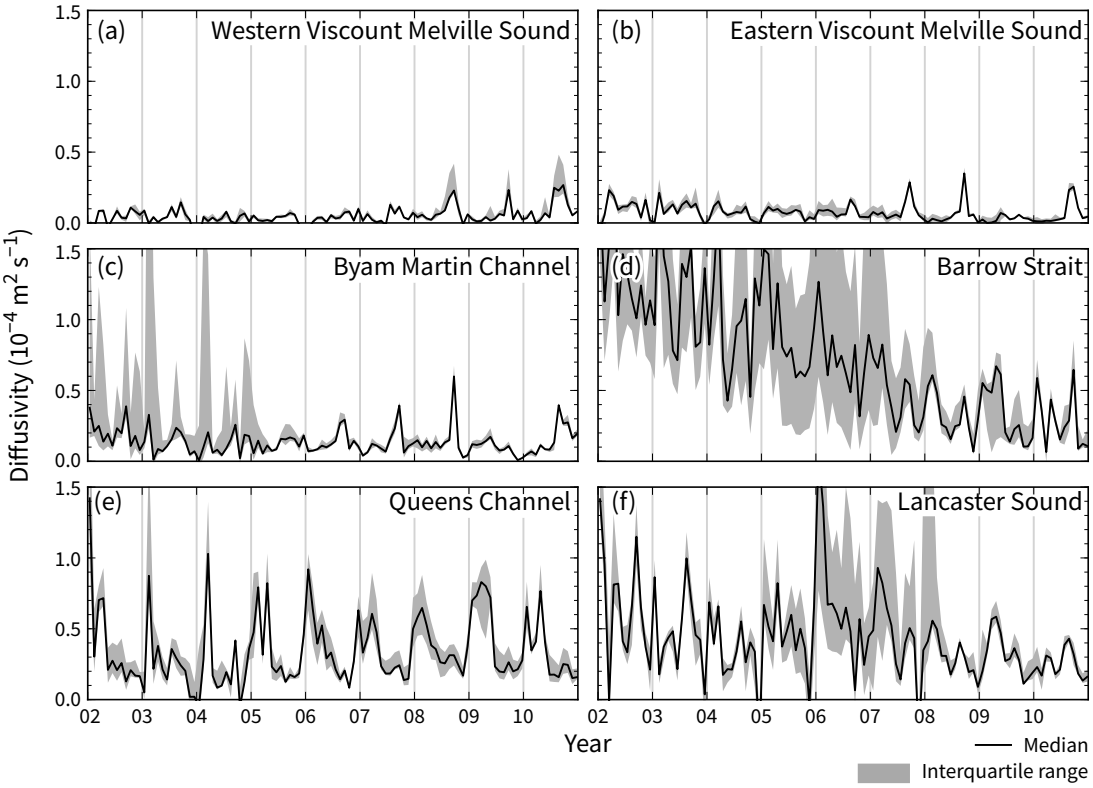

Figure 2.8 – Regionally averaged diffusivity ($\overline{K}$) exhibiting strong spatial and seasonal variability. Monthly averages were evaluated on 10 isopycnal surfaces (σ_θ = 26.8, 26.9, . . . , 27.7 kg m^{-3}), with the median and quartiles calculated from these 10 values.

the water above it. Conversely, in Barrow Strait the horizontal mass divergence is noticeably larger than the density rate of change term. This is akin to the situation shown in Figure 2.6a in which differences in properties between the ends of a channel are significantly affected by mixing.

It is difficult to discern the nature of the seasonal cycle of diffusivities as they are currently presented (Figure 2.8). Therefore, Figure 2.10a displays the median diffusivity on the $\sigma_\theta = 27.0\,\mathrm{kg\,m^{-3}}$ contour for each month of the year for each region. Each monthly median is calculated from nine values (one for each year of simulation). The three western regions exhibit one peak during the year. This peak occurs around late-summer. This time of year corresponds to both the minimum ice coverage and the maximum toward-Arctic fluxes (Figure 2.4). In contrast, the three eastern regions exhibit two peaks. In these regions the

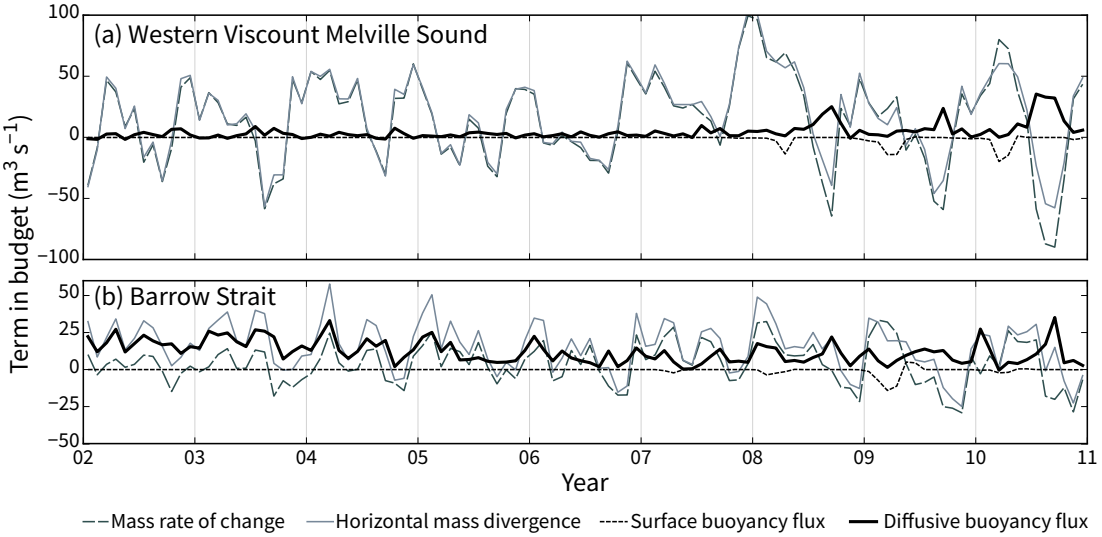

Figure 2.9 – The terms in the water mass budget (Equation 2.5) for the regions with the smallest and largest diffusivities. The budgets shown are calculated for water beneath the $\sigma_\theta = 27.0\,\mathrm{kg\,m^{-3}}$ isopycnal.

late-summer peak is minor in comparison to one around the new-year. This second peak occurs when the strongest volume fluxes typically occur.

To some degree, the diffusivities we have derived are influenced by stratification. Increased stratification limits diffusivity and vice versa. Therefore, we briefly consider alternative metrics that quantify mixing. These are the buoyancy flux J_b defined within Equation 2.3 and turbulent dissipation rate ε given by

$$\varepsilon = J_\mathrm{b}/\Gamma \approx 5J_\mathrm{b} \tag{2.6}$$

where Γ is the mixing efficiency set as 0.2 (Osborn, 1980). Plots of buoyancy flux (Figure 2.10b) look similar to those for effective diffusivity because stratification varies less than diffusivity. Using $\varepsilon \approx 5J_\mathrm{b}$ suggests average turbulent dissipation rates of 3–5$\times 10^{-8}\,\mathrm{m^2\,s^{-3}}$ in Queens Channel and Barrow Strait. For comparison, background dissipation rates of less than $10^{-8}\,\mathrm{m^2\,s^{-3}}$ have been observed in locations such as the New England Shelf (Gregg et al., 1999) and rates of 10^{-8}–$10^{-6}\,\mathrm{m^2\,s^{-3}}$ in Admiralty Inlet in Washington (Seim and Gregg, 1994) and over the Romanche Fracture Zone (Ferron et al., 1998). Values of 10^{-5}–$10^{-3}\,\mathrm{m^2\,s^{-3}}$ can occur in the immediate vicinity of sills (e.g., Klymak and Gregg, 2004; Staalstrøm

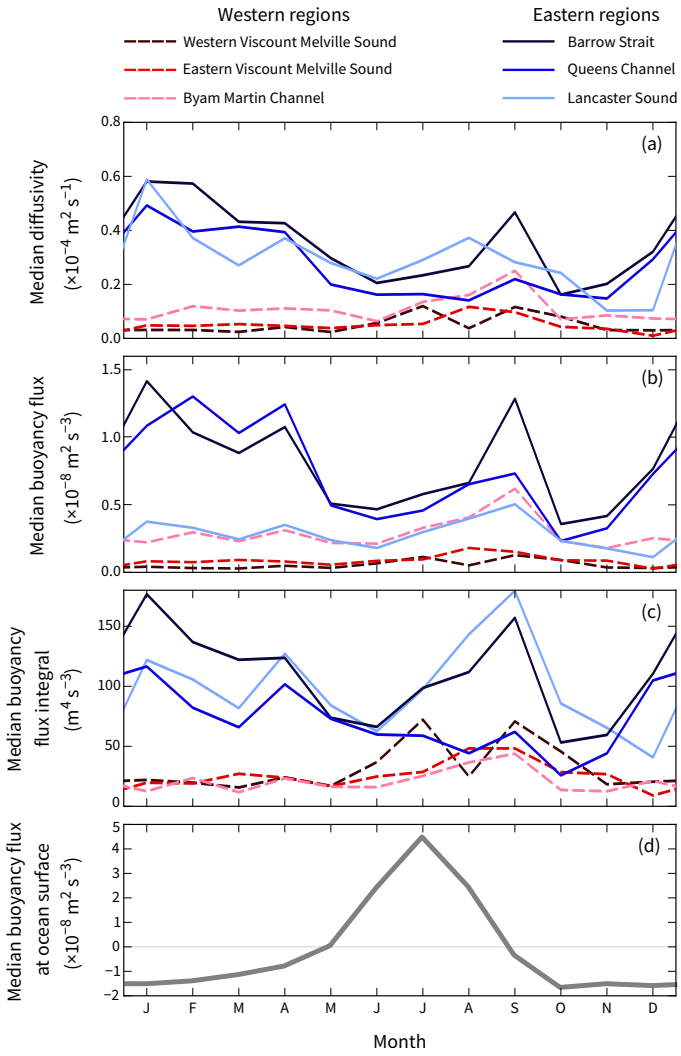

Figure 2.10 – (a–c) Metrics of regionally averaged mixing evaluated on the σ_θ = 27.0 kg m^{-3} isopycnal surface. Medians for each month were calculated from the values for nine years of simulation. (d) Median buoyancy exchange at the ocean surface over all six regions.

et al., 2015). These very high values reduce to $O(10^{-6})\,\mathrm{m^2\,s^{-3}}$ if they are averaged over an area of $O(1)\,\mathrm{km^2}$. Note that these comparisons are tenuous for two reasons. First, dissipation rate estimates can vary by orders of magnitude over a short time, short distance, or within a single profile. Second, there is some uncertainty in the value of the mixing efficiency and indications that it is not constant (Ivey et al., 2008).

Interpreting the results in terms of total (areally integrated) buoyancy flux (Figure 2.10c) emphasizes the roles of the deeper regions, and vice versa, but does not change our conclusion of stronger mixing in the eastern Archipelago. Within the deeper regions, Viscount Melville Sound and Lancaster Sound, the $27.0\,\mathrm{kg\,m^{-3}}$ isopycnal surface has a large area. Conversely, for example, the 580–680 km region of Queens Channel in Figure 2.5a is insufficiently deep to host any water denser than $27.0\,\mathrm{kg\,m^{-3}}$. Indeed, for part of the seasonal cycle, the total buoyancy flux in Queens Channel reduces to that of western Viscount Melville Sound. We note, however, that these values are significantly affected in part by how we designated the six regions in Figure 2.1c; for example, the ocean surface area of the western Viscount Melville Sound region is four times that of Queens Channel.

2.4.4 Surface and near-surface water mass modification

For eight months of the year, the cold atmosphere either directly cools the near-surface water or induces ice growth and consequent brine rejection. These cause a destabilizing flux at the ocean surface (Figure 2.10d), which drives mixing of near-surface water. For the other four months, insolation and ice melt act to restratify the near-surface. The magnitude of the destabilizing flux reaches $1.5 \times 10^{-8}\,\mathrm{m^2\,s^{-3}}$. This is comparable to the buoyancy fluxes through the $27.0\,\mathrm{kg\,m^{-3}}$ isopycnals in Queens Channel and Barrow Strait for parts of the year. For the western regions, however, the ocean surface buoyancy flux is an order of magnitude larger than the diapycnal flux. In effect, variability in near-surface water mass properties is dominated by the buoyancy exchange with the atmosphere. Note that surface buoyancy flux is largely independent of location within the Archipelago.

To determine mixing rates in the near-surface water, we attempted the analysis

from the previous section but for shallower isopycnals such as 26.0 or 26.5 $\mathrm{kg\,m^{-3}}$. However, meaningful estimates of the diapycnal fluxes through these isopycnals is typically not possible. The buoyancy exchange F at the ocean surface is no longer a small term, so the diapycnal buoyancy flux is now the residual of three large terms (see Equation 2.2b). The uncertainty in each of the three terms (see Section 2.4.1) results in an uncertainty in the residual comparable to its magnitude.

There were short periods that allowed a reasonable estimate of the diapycnal flux through the 26.5 $\mathrm{kg\,m^{-3}}$ isopycnal, which is typically half as deep as the 27.0 $\mathrm{kg\,m^{-3}}$ isopycnal (Figure 2.3). These periods occurred early in the simulation, when stronger ice cover mediated surface exchange. During this time, the buoyancy fluxes through the shallower isopycnal displayed similar magnitudes to those described in the previous section.

2.5 Discussion

2.5.1 Predicting mixing without tides

The ANHA12 model used in this study does not contain tides, a trait shared by most other existing models of the Archipelago at similar resolutions (Houssais and Herbaut, 2011; Wang et al., 2012; Wekerle et al., 2013; Lu et al., 2014). It is therefore arguably a poor choice for a study concerned with estimating mixing rates in a region in which mixing is strongly linked to tidal flow (Hannah et al., 2009; Melling et al., 2015) and contains sills that are substantially longer than a tidal excursion. Indeed, a range of quantities related to mixing have been observed or simulated to vary fortnightly with the spring–neap cycle: turbulent energy, velocity shear, eddy diffusivity, nutrient flux, and tidal dissipation (Prinsenberg and Bennett, 1987; Marsden et al., 1994b; Hannah et al., 2009).

Tides within the Archipelago can generate strong shears due to critical latitude effects. In particular, the critical latitude of the M_2 tide coincides with Parry Channel. Consequently, the clockwise component of the tide has thick surface and bottom boundary layers resulting in mixing in the interior (Prandle, 1982). Tides can also induce persistent vertical motions through enhanced Ekman pumping and stretching of relative vorticity. Luneva et al. (2015) demonstrated that these

motions can result in penetration of Atlantic Water to the surface in the Arctic Ocean. These authors also note the strong potential for these motions in the Archipelago, but their model is too coarse to sufficiently resolve internal tidal effects in this shallower region.

Quantitatively, tidally induced mixing may be as strong or stronger than the mixing accounted for in this study. For example, Kagan et al. (2010) calculated the depth-average vertical diffusivity due to internal-tide-induced mixing from a finite element model and found it to be $1–10\times10^{-5}\,\mathrm{m^2\,s^{-1}}$ throughout much of the Archipelago. Even larger values occur within Lancaster Sound where the tidal energy flux is largest (Chen et al., 2009). This range of diffusivities is comparable to the inverse estimates derived here. Note, however, that Kagan et al. (2010) neglect interaction between internal-tide-induced turbulence and other turbulence.

Despite the influence of tides, tideless simulations are likely to remain prevalent given that many contemporary studies are focused on seasonal and interannual variability. It is therefore worth investigating whether reasonable conclusions regarding mixing can be derived from this model and by generalization those similar. Without tides, energy for mixing must come from either atmospheric forcing or the mean flow.

2.5.2 Evaluating the inverse estimates

Direct comparison between observations with the mixing rates derived here is not possible. Only a few dedicated mixing observations are available in the literature and each of these contains only a single site. Nevertheless, we attempt a comparison to at least ensure simulated mixing rates are in the ballpark of observations.

Using turbulence instrument clusters in central Barrow Strait but within 10 km of a small island and shoal, Crawford et al. (1999) measured hourly-averaged diffusivities well below the near-surface halocline of 10^{-5}–$10^{-4}\,\mathrm{m^2\,s^{-1}}$ with occasional spikes up to $10^{-3}\,\mathrm{m^2\,s^{-1}}$. The lower end of this range of values is consistent with Figure 2.10a. We would not expect our results to display the larger diffusivities observed as we derive values averaged over one month and over a large area. Indeed, elevated mixing often arises due to events with hourly timescales. For

example, Marsden et al. (1994a) observed dissipation rates south of Cornwallis Island of $10^{-6}\,\mathrm{m^2\,s^{-3}}$ associated with finite-amplitude internal waves. However, these events typically occurred only once per day and lasted only 1–2 hours. As Marsden et al. (1994a) focused on near-surface events, we do not compare our estimated dissipation rate with their observations.

To establish a better picture of the extent of enhanced mixing predicted by our model, histograms of buoyancy flux for individual grid cells were calculated (Figure 2.11). These are based on the density field and the diffusivity, the latter being dependent on the TKE (Section 2.2). Like other outputs, five-day means of diffusivity were recorded. Two of the six regions are shown: western Viscount Melville Sound and Barrow Strait. The histograms are calculated from output using the whole nine years of simulation, and to make their values comparable to earlier figures we use only cells straddling the $\sigma_\theta = 27.0\,\mathrm{kg\,m^{-3}}$ isopycnal.

For both sections, 80–90% of buoyancy flux values are $< 10^{-9}\,\mathrm{m^{-2}\,s^{-3}}$. Given there is a minimum cut off for K of $10^{-6}\,\mathrm{m^{-2}\,s^{-1}}$ and N^2 is typically $10^{-4}\,\mathrm{s^{-2}}$, this implies that most of the deep water column is, on five-day timescales, relatively tranquil; there is insignificant shear to promote buoyancy flux well above low background values. However, there exists a small set of values with large buoyancy fluxes. The proportion of the water exhibiting these high buoyancy fluxes differs for the two sections shown: buoyancy fluxes exceeding $10^{-7}\,\mathrm{m^2\,s^{-3}}$ make up 1.4% of the total for western Viscount Melville Sound, but 6% of the total for Barrow Strait. Both histograms display a local peak at $\log_{10}(J_\mathrm{b}) = -4$ because of the convective adjustment scheme in which a vertical diffusivity is set to $10^1\,\mathrm{m^2\,s^{-1}}$ in unstable regions (Section 2.2). Large buoyancy fluxes, despite their low frequency, contribute significantly to the total buoyancy flux. For example, only 10% of values in either histogram are greater than their respective inverse estimate.

Ultimately, by comparing our estimates to the limited existing observations within the Archipelago and in other regions (Section 2.4.3), we are only able to state there is nothing that appears to notably contradict the values we obtained. Numerically, our values are the expected order of magnitude, but it is unclear whether this represents model skill or is merely attributed to using realistic values for inputs such as the minimum diffusivity. For that reason, it is arguably more useful to investigate whether the spatial variation we derived is reasonable.

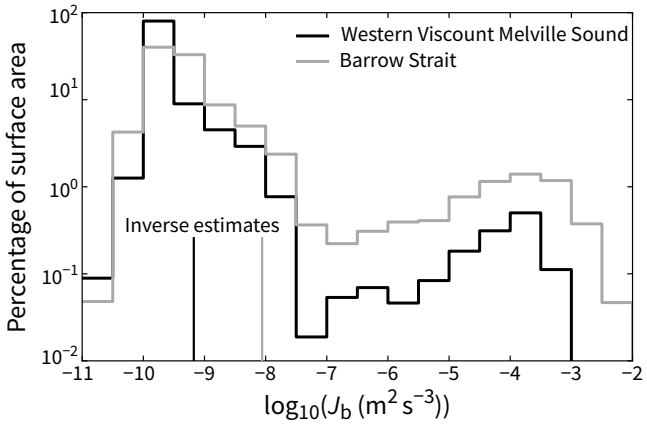

Figure 2.11 – The distribution of buoyancy flux (J_b) on the $\sigma_\theta = 27.0$ kg m^{-3} isopycnal surface within the regions displaying the weakest and strongest mixing in our analysis. For the respective regions, the area-weighted histograms were created using five-day means of diffusivity and density in grid cells vertically straddling the isopycnal surface.

2.5.3 Where is water mass modification occurring?

Within the Archipelago, most modification appears to occur on the eastern side (Barrow Strait, Queens Channel, and Lancaster Sound); Figures 2.7, 2.8, and 2.10 suggest stronger mixing in these regions. Given the minimal flux through Queens Channel, however, it plays a lesser role in the total water mass transformation.

Given its location and topography, it is not surprising that we observed Barrow Strait to be a key region. The western edge of the region contains the shallowest (125 m) sill within Parry Channel, through which much of the total flux passes. Further, this region plays host to a number of different water masses, such as those from the southern Beaufort Sea, northeastern Canadian Basin, and Baffin Bay (de Lange Boom et al., 1987).

The map of surface density in Figure 2.2 agrees qualitatively with our findings of stronger mixing in the eastern Archipelago. Strong lateral density gradients can indicate strong vertical mixing if it is assumed that the mixing causes water masses that are otherwise at depth to outcrop at the surface. As expected, the strongest gradients occur within Barrow Strait, and moderate gradients occur in Queens Channel and Lancaster Sound. Conversely, surface density is relatively constant on the western side of the Archipelago where smaller diffusivities were derived. Equivalent maps to that in Figure 2.2 but at various depths were created

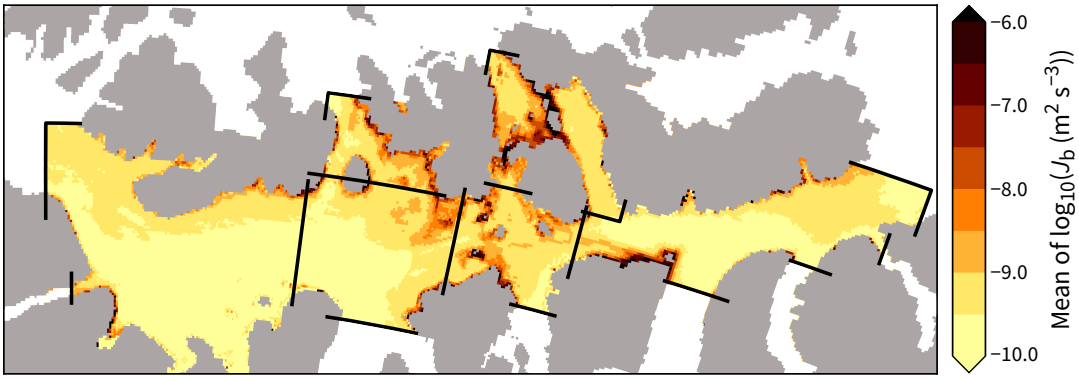

Figure 2.12 – Mean buoyancy flux evaluated on the σ_θ = 27.0 kg m^{-3} isopycnal surface diagnosed from the model's TKE closure scheme and density field. At each horizontal location, the value shown represents the temporal mean over the nine years of simulation for grid cells vertically straddling the isopycnal surface. The log of $J_b = KN^2$ was calculated before the mean was taken.

and showed similar patterns of horizontal gradients.

Observed temperature profiles provide further support for the spatial pattern of mixing we have derived. As noted by de Lange Boom et al. (1987), temperature maxima and minima have been observed in the western Archipelago, but these features are smoothed away by the upward mixing of heat. Consequently they are less visible in profiles in the eastern Archipelago or central sills area.

2.5.4 Identifying mixing hot spots

Analyzing water mass changes across large volumes is necessary for understanding the fate of water moving through the volume (e.g., Figure 2.9). However, it provides no indication of whether the averaged mixing is spread over the volume or the result of small hot spots. To address this, Figure 2.12 displays mean buoyancy flux calculated using the model's diffusivity and density fields for water of density $\sigma_\theta = 27.0\,\mathrm{kg\,m^{-3}}$. The values shown are the temporal average of $\log_{10}(J_b)$. This quantity is intended as a simple measure to highlight where hot spots exist. However, it is important to reiterate a point mentioned in Section 2.4.3: significant portions of the Archipelago may be insufficiently deep for parts of the years to host 27.0 kg m^{-3} water.

Not surprisingly, hot spots of mixing typically occur in shallower regions

(see Figure 2.1c). The converse, however, is not always true: there exist shallow regions without elevated mixing. Hot spots of particular note are those near the centres of the Barrow Strait and Queens Channel regions. As well as being shallow, both of these areas contain small islands that further constrict the flow. Note also that despite the lack of tides in our simulation, Figure 2.12 displays strong similarities with a map of the expected strength of tidal mixing (see Figure 7 of Hannah et al., 2009).

Figure 2.12 also helps understand the fate of water in Lancaster Sound. As described in Section 2.3.1, the component fluxes into and out of Lancaster Sound at its eastern entrance are several times larger than the fluxes elsewhere in the Archipelago (Figure 2.4b). Knowing only this, one may expect this region to display the strongest mixing. However, this is not the case: average buoyancy fluxes in Lancaster Sound are similar to those in Barrow Strait and Queens Channel. The stronger fluxes appear to be counteracted by the relative lack of mixing hotspots as shown by the broad regions of low mixing values throughout the Sound.

2.6 Conclusion

Simple partitioning of the Canadian Arctic Archipelago into six adjoining regions demonstrates that significant differences in diapycnal diffusivity exist. Flow in the western half is comparatively tranquil, so much of the transformation of water during its transit between the Arctic and North Atlantic occurs in the eastern half. Regardless of the metric used to quantify mixing, these spatial differences were consistently displayed. The strongest mixing is attributed to the result of sills in Queens Channel and Barrow Strait. These findings suggest that the interaction of flow with bottom topography is a key feature of models seeking to accurately simulate the dynamics in Archipelago. Indeed, further study is needed on mixing rates within topographically complex channels of the Archipelago to understand their role beyond their capacity to, say, carry a freshwater flux, which is often implied as their only important role.

With respect to temporal variation, mixing strength peaks either once or twice a year depending on the region. The largest peaks correspond to the months

of peak volume flux, which typically occur in the first months of the year in our simulation. Minor peaks also occur during late summer, the time of both minimum ice coverage and strongest toward-Arctic flow.

The numerical values of diffusivity, derived here using inverse estimates, appear reasonable. However, given the lack of tides in our simulation, we expect our values to underestimate the total mixing. Regional averages for the eastern Archipelago were typically 10^{-5}–$10^{-4}\,\mathrm{m^2\,s^{-1}}$. Within the Archipelago, however, there is a shortage of existing mixing rate estimates with which to compare; point observations at single sites or mooring across channels are useful, but many more are needed to allow regional extrapolations. Alternatively, targeted, high-resolution observations of local processes along a channel or over a sill could help quantify and characterize the nature of mixing on scales beyond the resolution of existing observations or models. This could be complemented by process-oriented modelling with tides that enables assessment of the relative importance of mixing phenomena such as internal wave breaking, internal hydraulic jumps and shear instabilities.

Acknowledgments

The authors would like to thank Humfrey Melling and Bill Williams for helpful discussion as this work took shape and two anonymous reviewers whose feedback helped improve this work. Temperature and salinity fields used to construct Figure 2 were provided by Nicolai Kliem. Atmospheric forcing data were provided by Greg Smith of Environment and Climate Change Canada. Initial conditions and open boundary conditions were provided by MERCATOR France. Further information about the ANHA12 model configuration is available at `http://knossos.eas.ualberta.ca/xianmin/anha/index.html`. Data in a reduced form and scripts used to create figures are available at `http://web.uvic.ca/~hugke729/`.

Chapter 3

Tidally modulated internal hydraulic flow and energetics

Abstract

The Canadian Arctic Archipelago is a key conduit for comparatively fresh Arctic waters flowing to the Atlantic. Model estimates of the freshwater outflow, which is strongly correlated with the volume flux, contain major uncertainties because most existing models exclude tides, marginally resolve the internal Rossby radius, or both. At the same time, barotropic tidal models preclude stratified flow effects. Here we assess the relative importance of barotropic and baroclinic processes to water mass transformation, friction, and energy losses motivated by processes observed in a fine-scale survey in the central Archipelago. A sharp separation of warmed Canada Basin water and locally formed water is observed over a long sill in a narrow channel and coincides with an internal hydraulic jump caused by the mean flow. Tidal currents, however, modulate the jump, as demonstrated by both scale analysis and a two-dimensional simulation. The jump, together with internal tides propagating as Kelvin waves, leads to isopycnal displacements up to 50 m. The generation of these internal Kelvin waves has a leading-order role in a regional energy budget. It is small, however, relative to bottom boundary layer dissipation, which accounts for an estimated 50% of the total tidal energy losses. Consequently, adding tides needs to be a priority for regional models.

Published as

Hughes K.G., J. M. Klymak, W. J. Williams, and H. Melling (2018) Tidally modulated internal hydraulic flow and energetics in the central Canadian Arctic Archipelago *J. Geophys. Res.*, 123, 5210–5229, doi:10.1029/2018JC013770

3.1 Introduction

Volume and freshwater fluxes through the Canadian Arctic Archipelago have been the subjects of both observational and modelling studies (e.g., Peterson et al., 2012; McGeehan and Maslowski, 2012) owing to their roles in the global hydrological cycle (Carmack et al., 2016), their transport of nutrient-rich waters from the Pacific to the Atlantic via the Arctic (McLaughlin et al., 2004), and their contributions to 'great salinity anomalies' in the North Atlantic Ocean (Belkin et al., 1998). Existing models, however, tend to overestimate the volume flux, indicating a need to identify the dominant momentum and energy sinks to inform future modelling efforts. For example, several models with 4–6 km resolution have simulated long-term ($>$ 10 years) mean volume fluxes through the western end of Lancaster Sound of 0.8, 0.9, 1.0, and 1.1 Sv (McGeehan and Maslowski 2012; Wekerle et al. 2013, Chapter 2, Lu et al. 2014, respectively). This range is twice the observed estimate of 0.5 Sv (Peterson et al., 2012). Further, 10 coarse-resolution models from an intercomparison project produce a range of freshwater fluxes of 20–110 mSv with a mean of 60 mSv (Jahn et al., 2012), whereas the observed estimate is 30 mSv (Peterson et al., 2012).

Tidal and mean currents are of a similar magnitude within the Archipelago. Both, for example, reach approximately 0.2 m s^{-1} in western Lancaster Sound. With some exceptions (Chen et al., 2009; Luneva et al., 2015; Zhang et al., 2016), tides are not included in most three-dimensional models. Although this implies that tidally driven processes are a prime candidate to rectify the discrepancy between models and observations, care must be taken. Because typical model grid spacings are comparable to the internal Rossby radius and the tidal excursion, even if the smaller-scale processes studied in this chapter are simulated, they may be poorly resolved.

The similarity between tidal and mean current speeds implies that nonlinearities that arise may be significant. Consider energy loss to bottom boundary layer dissipation, which scales as U^3 where U is the total (mean + tidal) velocity. Similarly, internal processes resulting from stratified flow over topography cause barotropic energy losses that scale as U^2 or U^3 (e.g., Llewellyn Smith and Young, 2003; Klymak et al., 2010a). Such processes include internal hydraulic jumps, internal tides, and topographically induced eddies. These can induce drag that

is an order of magnitude larger than friction over a flat bottom (Warner et al., 2013). The cumulative effect of these various drags in the many channels in the Archipelago ultimately influences flow pathways out of the Arctic. For example, Joyce and Proshutinsky (2007) use a barotropic model to demonstrate strong sensitivities to bathymetric variations and lateral friction on the partitioning of flux between the Archipelago and Fram Strait.

Within the Archipelago, fine-scale predictions of tidal velocity and hence tidal dissipation are given by WebTide (see Collins et al., 2011), which sufficiently resolves all but the smallest channels. For our purposes, however, it suffers two limitations. First, being a barotropic model, it precludes baroclinic motions associated with the tide, observations of which include tidally generated, high-frequency internal wave trains (Marsden et al., 1994b; Crawford et al., 1999) and spring–neap modulation of turbulent energy, shear, and eddy diffusivity (Prinsenberg and Bennett, 1987; Crawford et al., 1999). Second, it uses a spatially variable, but temporally fixed, drag coefficient to account for the approximate annual mean sea ice concentration. Furthermore, this extra drag is likely overestimated where ice is hydrodynamically smooth (see, e.g., Crawford et al., 1999). Stratified effects over rough bathymetry may play a role comparable to ice effects, but the former are not accounted for.

While strong tidal currents and rough bathymetry are ubiquitous in the Archipelago, a particularly relevant region is the central sills area near Cornwallis and Bathurst Islands (Figure 3.1). This region hosts many of the channels with the strongest tidal currents in the Archipelago. The shallow ($\sim$50 m) sills here induce strong mixing and upslope advection of heat (e.g., Hannah et al., 2009), thereby leaving a surface signature in the form of visible and invisible polynyas (Melling et al., 2015), where the latter may be identified via comparatively early sea ice break up in summer. Moreover, the central sills area is a meeting ground, an obstacle separating water masses of widely different origin (de Lange Boom et al., 1987). Yet, despite recognition of their role in both mixing and dictating the extent of different waters, the dynamics of flow through the central sills area has received minimal attention.

Here we discuss high-spatial-resolution hydrographic and velocity data over and adjacent to a sill in the central Archipelago (Section 3.2). These data enable three self-contained, complementary approaches to characterizing the tidal and

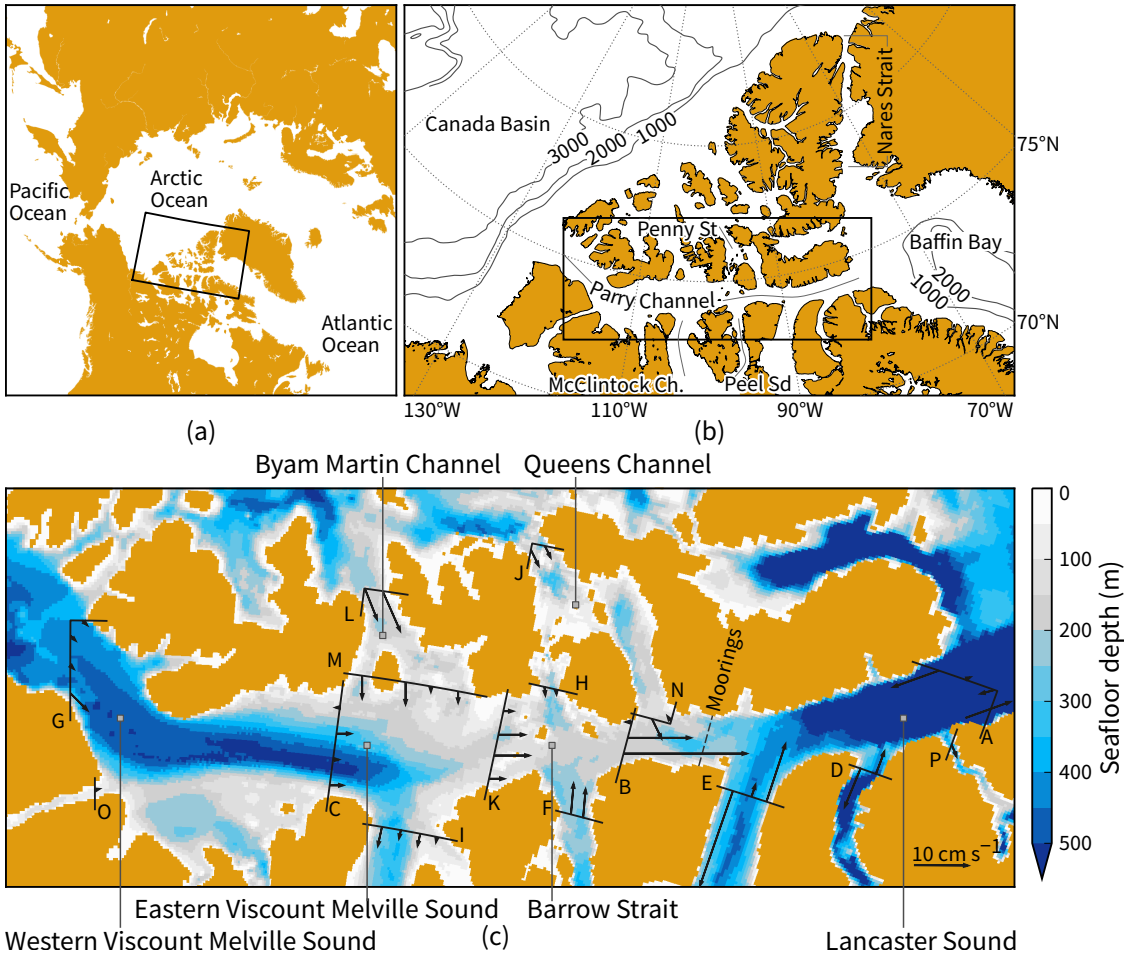

Figure 3.1 – Summary of the observational survey, which was undertaken in a region where tides are strong. (a) The time-average of tidal current magnitude as predicted by WebTide (Collins et al., 2011). (b) Bathymetry in the survey region. Note the complex bathymetry within Penny Strait (upper left corner) and the broad, shallow region northwest of Cornwallis Island. Sea ice conditions are determined from satellite imagery.

sill dynamics. First, we examine the hydrography downstream of the sill and look for signatures of the sill outflow (Section 3.3). Next, we identify an internal hydraulic transition in repeat transects over the sill (Section 3.4). Last, we estimate energy sources and sinks (Section 3.5). We conclude by linking our spatially limited observations to the rest of the central Archipelago (Section 3.6).

3.2 Observational survey and data processing

A four-day survey to elucidate tidal and mean flow dynamics, map turbulent structures, and quantify energetics in the central Archipelago was undertaken in late September 2015 aboard the CCGS Amundsen. The general location was chosen based on past evidence of strong mixing from large-scale transects and tidal modelling (de Lange Boom et al., 1987; Hannah et al., 2009). Six along-channel transects were occupied (Table 3.1, Figure 3.2) to constrain changes with the tidal cycle, and six across-channel transects in Wellington Channel were occupied to estimate volume fluxes and seek evidence for water mass modification. (A seventh across-channel transect was undertaken in western Lancaster Sound, but this is not examined in the present study.) The 200 km-long initial transect provides a coordinate system for all along-channel transects with zero as the northernmost point (see Figure 3.1b), this limit being dictated by sea ice.

Our decisions to go through Maury Channel, not the other nearby channels, and to forego cross-channel transects within this channel reflect a time constraint and ice cover limitation. There were no presumptions at any stage that lateral variability was unimportant or that water preferentially flowed through Maury Channel. We simply lacked time to investigate these aspects.

The primary tools used were a Moving Vessel Profiler (MVP) containing an AML Oceanographic Micro CTD, and a 150 kHz Teledyne RD Instruments Ocean Surveyor ship-mounted Acoustic Doppler Current Profiler (ADCP). Because the water column is measured as the ship steams at $15\,\mathrm{km\,h^{-1}}$, the profiles produce a near-synoptic two-dimensional picture of the ocean over scales of tens of kilometres. Standard rosette CTD profiles (Sea-Bird SBE9) were taken when the MVP was unusable given the sea ice conditions or when ice formed on the winch

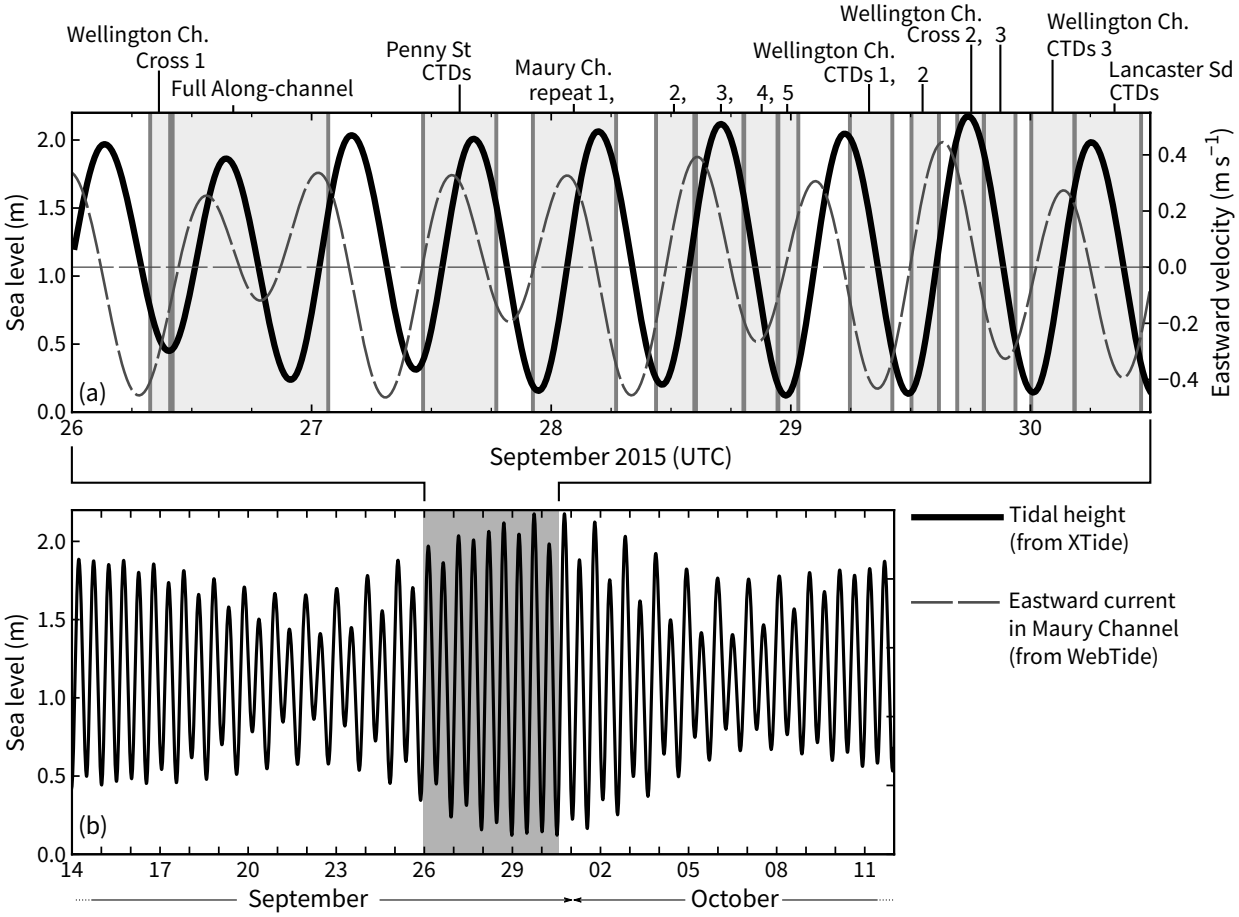

Figure 3.2 – Sampling periods of all transects. (a) Tidal height in Wellington Channel and tidal current velocity through Maury Channel. (b) The position of the four-day sampling period within the spring–neap cycle. Note that currents and heights are evaluated from different sources, hence the discrepancy between whether the tide in panel a is semidiurnal or slightly mixed semidiurnal. See Table 3.2 for tidal height details and Sections 3.1 and 3.5 for WebTide details.

Table 3.1 – Timeline of the observational survey.

Transect	Time (UTC) and Date (2015)	No. of casts
Wellington Channel Cross 1	07:50 26 Sep–09:50 26 Sep	39
Full-length Transect	10:05 26 Sep–01:40 27 Sep	281
Penny Strait CTDs	11:10 27 Sep–18:30 27 Sep	8
Maury Channel Repeat 1	22:10 27 Sep–06:30 28 Sep	180
Maury Channel Repeat 2	10:30 28 Sep–14:20 28 Sep	138
Maury Channel Repeat 3	14:30 28 Sep–19:15 28 Sep	107
Maury Channel Repeat 4	19:20 28 Sep–22:40 28 Sep	112
Maury Channel Repeat 5	22:45 28 Sep–00:45 29 Sep	91
Wellington Channel CTDs 1	05:55 29 Sep–10:10 29 Sep	5
Wellington Channel CTDs 2	12:05 29 Sep–14:50 29 Sep	5
Wellington Channel Cross 2	16:40 29 Sep–19:20 29 Sep	43
Wellington Channel Cross 3	19:20 29 Sep–22:30 29 Sep	52
Wellington Channel CTDs 3[a]	00:05 30 Sep–04:25 30 Sep	5
Lancaster Sound CTDs[a]	04:25 30 Sep–11:05 30 Sep	7

[a] An unintended gap exists in the ADCP record between 03:10 and 08:00 on 30 September.

cable. Additionally, backscatter strength from a 120 kHz, ship-mounted Simrad EK60 echosounder clarifies some of the structures observed with the MVP.

Approximately 1100 vertical profiles of temperature and salinity were obtained with the MVP (Figure 3.1b). The MVP falls at $4\,\mathrm{m\,s^{-1}}$ while recording at 25 Hz. Salinity spiking was largely removed by shifting the temperature signal by 3.2 samples (0.13 s). However, the temperature and conductivity signals are only sufficiently correlated to calculate salinity and density at 2–3 Hz (Figure 3.3a), equating to an effective vertical resolution of 1.5 m. In all casts, the top and bottom 10 m of the water column were not measured and casts were spaced 200–300 m apart in shallow regions and 1000–2000 m in deeper regions.

Rosette-mounted CTD profiles were processed in a similar manner. The slower descent rate ($0.7\,\mathrm{m\,s^{-1}}$) and the coherence of the temperature and conductivity sensors up to 6–7 Hz (Figure 3.3b) gave an effective vertical density resolution of 0.1 m. These density data, low-pass filtered at 6 Hz, are used in Section 3.5 to evaluate Thorpe scales and turbulent dissipation.

Velocities were recorded continuously and processed using the University of Hawaii CODAS ADCP processing software (Firing et al., 1995). Data were recorded in 4 m vertical bins and reached as deep as 190 m. With pings every 10 s and horizontal binning with a 30-sample (5 minute) window, typical spatial

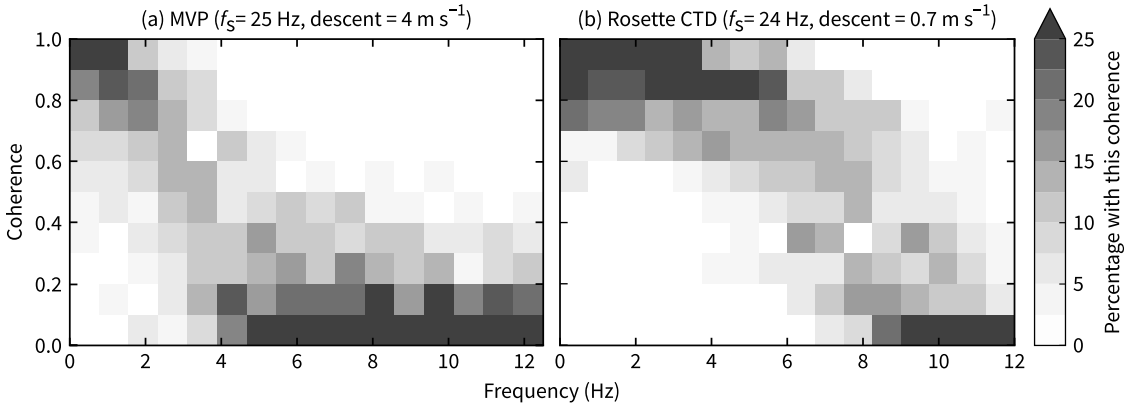

Figure 3.3 – Coherence between the temperature and conductivity sensors for two different platforms. The distributions for each platform were calculated from 30 profiles in the same regions. Coherence (specifically the normalized magnitude squared coherence) is calculated using FFTs of length 128.

averaging is 1.5 km.

3.3 Hydrography

The modelled net southward flux from Wellington Channel and McDougall Sound, which are the pathways east and west of Cornwallis Island, is ∼0.3 Sv (Chapter 2, see also McGeehan and Maslowski, 2012). This flux joins and influences the properties of the larger flow through Parry Channel, the main east–west channel in the Archipelago. In this section, we examine the hydrography between southern Wellington Channel and southern Penny Strait with an aim to better understand and quantify the outflow of northern waters.

3.3.1 An abrupt transition in properties

Two distinct water masses, one traceable to the Arctic Ocean and the other locally formed, occur within 50 km of each other and are separated by shallow sills. An annotated interpretation of these water masses is given in Figure 3.4, together with climatological curves for Canada Basin and Baffin Bay for context. We expect our late-September profiles to be summer-like in character except in the top 20 m where recent heat loss to the cold atmosphere is evident.

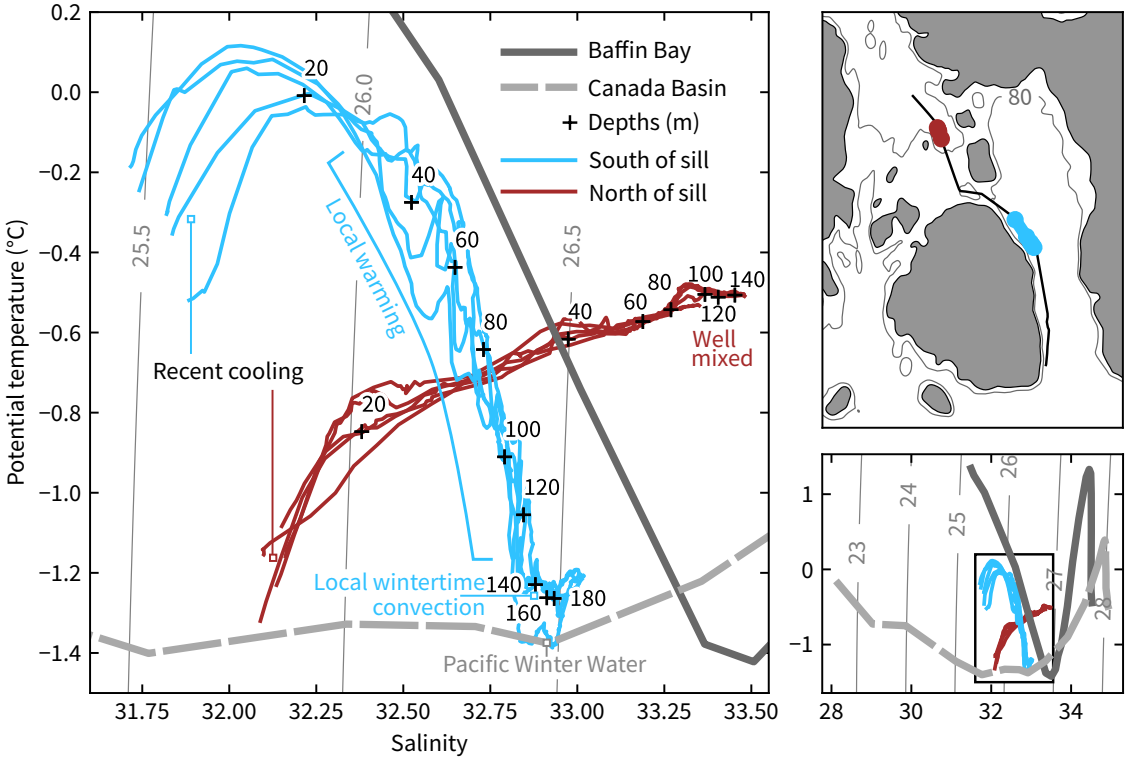

Figure 3.4 – Representative properties either side of the sill. The climatological curves given for context are from Kliem and Greenberg (2003), who use observational data centred about September 1.

Wellington Channel, south of the sills, hosts water that is predominately locally formed during winter. Strong atmospheric exchange in polynyas in the many narrow channels (e.g., Hannah et al., 2009; Melling et al., 2015) produces cool, saline water that convects and fills Wellington Channel. For example, in their Figure 2.6, de Lange Boom et al. (1987) indicate a nearly homogeneous water column in Wellington Channel with a salinity of 33.0 and a temperature of $-1.6\,^{\circ}\mathrm{C}$, similar to what we observe in the bottom 50 m. Their figure also demonstrates uplift and outcropping of $S < 33.0$ waters south of Wellington Channel that allows for local warming and likely explains our observations showing an increase of temperature with proximity to the surface.

Water near Penny Strait, north of the sills, is Canada Basin water that is warmed by mixing with Atlantic Water (e.g., Melling et al., 1984). In the Canada Basin, the Atlantic layer lies beneath the Pacific Water, with the latter at a depth

of 60–200 m (Carmack et al., 2016). The northernmost 10 km of the transect also shows evidence of a warmer water mass centred about 50 m with its extent limited by bathymetry and its specific origin unknown (Figure 3.5a).

The temperature and density fields between Wellington Channel and Penny Strait, especially near the sills, display three notable features (Figure 3.5): a strong temperature front at approximately 100 km, a possible internal hydraulic jump at the same location (see Section 3.4), and a large change in the depth of the 26.5 $\mathrm{kg\,m^{-3}}$ isopycnal. Near the southern end of the sills ($x = 100$ km), isopycnals in the density range $\sigma_\theta = 26.2$–$26.4\,\mathrm{kg\,m^{-3}}$ plunge and then rebound over approximately 10 km. Over the distance of the depressed isopycnals, the temperature structure switches from increasing to decreasing with depth.

3.3.2 Cross-channel structure in Wellington Channel

Being approximately 10 times wider than the internal Rossby radius, the baroclinic component of the flow in Wellington Channel is expected to be cyclonic with northward inflow on the eastern side from Lancaster Sound and southward outflow on the western side (see, e.g., Figure 3.6d). The addition of waters at Wellington Channel's northwestern end should therefore manifest as cross-channel differences in temperature and salinity (see Section 3.3.3). Before examining such changes, we establish the typical properties of the cross-channel transects. The 'Cross 2' transect is representative and provided as an example (Figure 3.6).

The coastal current on the eastern side in the top 30 m is a dominant feature and is observed in all transects. Its warm, fresh signature is responsible for much of the range in temperature–salinity space (Figure 3.6c), but it occupies only a small fraction of the cross-sectional area. This signature is diluted as it flows northward. Typical long-channel rates of change of temperature and salinity estimated by comparing different cross-channel transects are 1°C and 1 psu over 75 km. These gradients suggest the current will retain its signature for another approximately 25–50 km, meaning it will not reach the northern end of Wellington Channel, a finding consistent with de Lange Boom et al. (1987).

Typically there is a net southward flow out of Wellington Channel. During the Cross 2 transect, however, the tidal current is northward. Consequently,

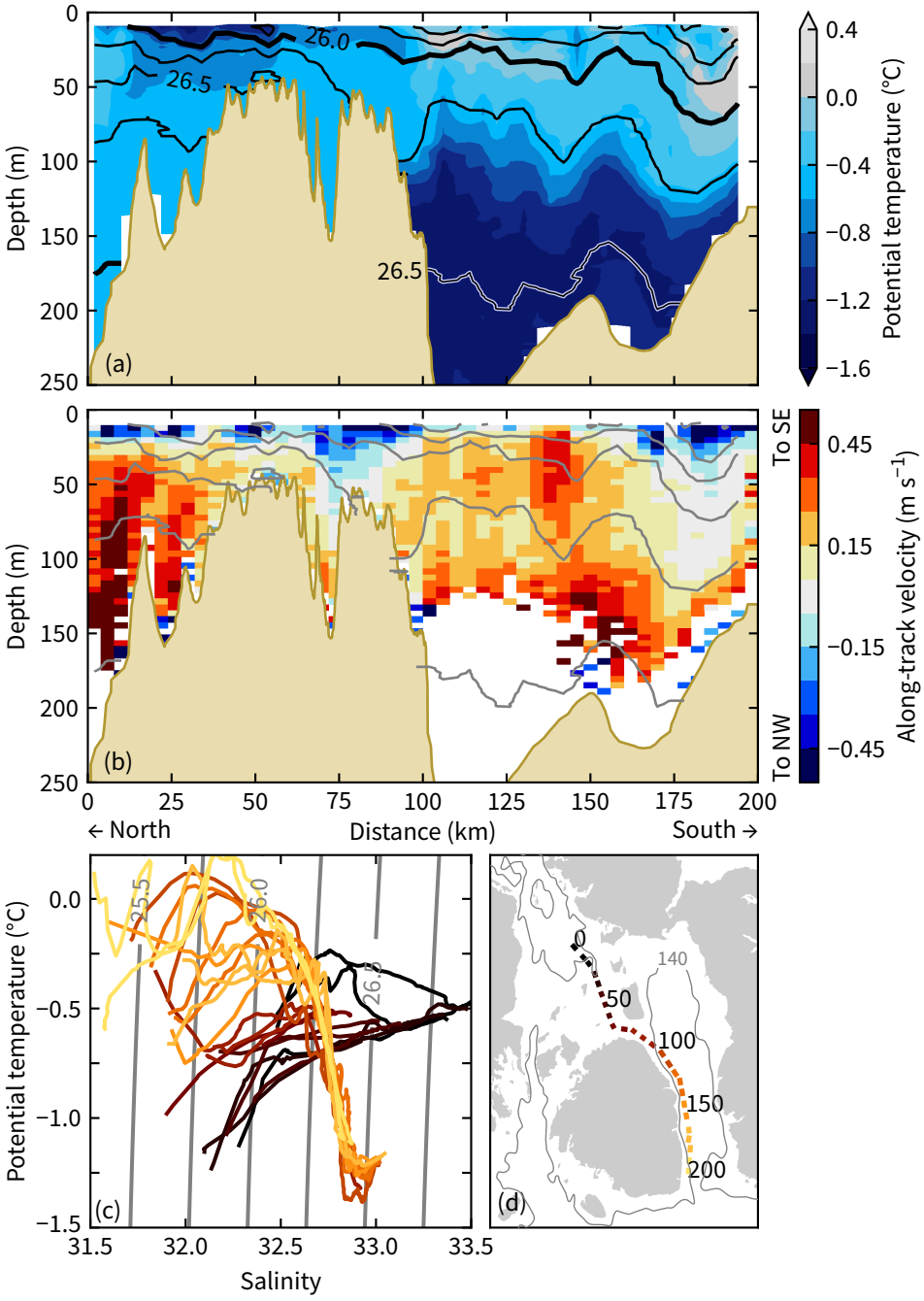

Figure 3.5 – Hydrography along the longest transect. Contour lines in panels a–c are potential density (σ_θ), most temperature–salinity curves are not shown for clarity, and data are smoothed laterally to better depict the larger-scale fields. Note that this longest transect took 16 hours and may therefore alias tidal features.

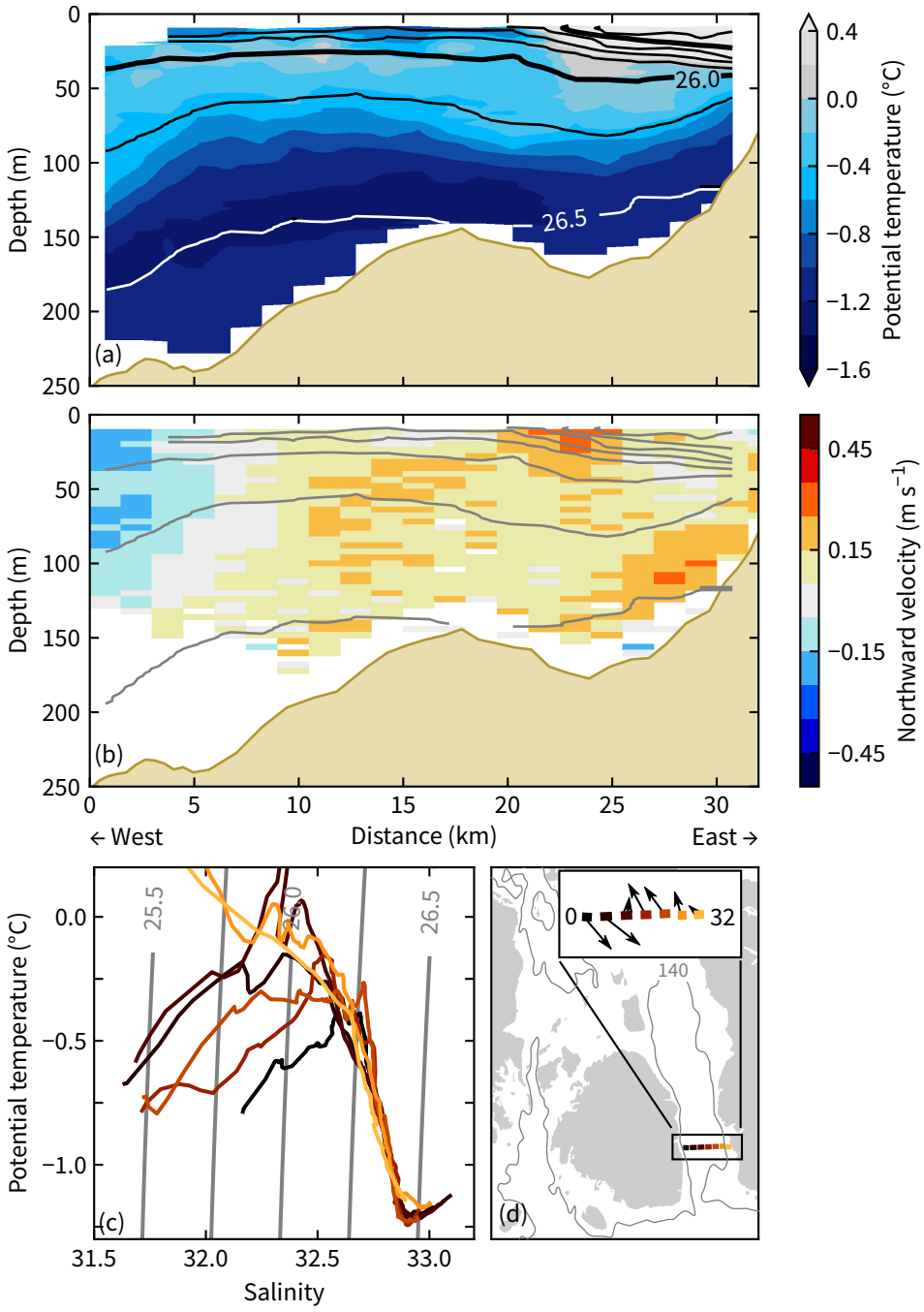

Figure 3.6 – Hydrography in Wellington Channel from the Cross 2 transect. Contour lines in panels a–c are potential density (σ_θ), most temperature–salinity curves are not shown for clarity, and data are smoothed laterally to better depict the larger-scale fields. Note that the arrows in panel d represent the barotropic flow.

Table 3.2 – Along-channel fluxes in Wellington Channel ordered by net flux.

Transect	Mean latitude	N-ward flux (mSv)	S-ward flux (mSv)	Net flux (mSv)	[a]Percent coverage	[b]Tidal height (m)	
						Mean	Range
CTDs 2	75°15′	0	490	−490	55	0.6	0.2 → 1.2
CTDs 3	74°41′	20	250	−230	53	0.7	0.1 → 1.6
Cross 1	74°46′	80	140	−60	55	0.5	0.7 → 0.5
Cross 3	74°50′	210	190	+20	71	1.2	1.8 → 0.6
CTDs 1	75°29′	240	30	+210	41	1.3	2.0 → 0.5
Cross 2	75°0′	370	70	+300	62	2.1	2.1 → 1.9

[a] Percent coverage indicates the portion of the total cross-sectional area in which good ADCP data exist. No extrapolation to include the missing areas is included in the flux calculations.
[b] Tidal height at Refuge Cove in Wellington Channel (Figure 3.1b). Tidal prediction using XTide (Flater, 2016) via the interface at `http://tbone.biol.sc.edu/tide/`. See Table 3.1 for time and date of transect.

much of the water on the eastern side was flowing northward with a speed of 0.1–0.2 m s^{-1}. During the transect, 62% of the total cross-sectional area was captured by the ADCP. The directly measured (unextrapolated) velocities indicate northward and southward volume fluxes of 370 mSv and 70 mSv, respectively. These values vary strongly throughout the tidal cycle (Table 3.2). Note that we choose to not extrapolate fluxes as the missing data are either near the sea surface or seafloor where Ekman layers will occur or near the lateral boundaries where increased friction is expected.

Within Wellington Channel, northward velocity is effectively in phase with tidal elevation: WebTide, a barotropic tidal model of the Archipelago (see Collins et al., 2011), suggests the northward current peaks only 30 minutes after high tide. This is consistent with our observed fluxes (Table 3.2): the largest northward fluxes occur at high tide and the largest southward fluxes at low tide. Between the six across-channel transects in Wellington Channel, the tidal range was covered. Consequently, the observed range in flux should be similar to the true range.

On the western side of the channel, the flow has a similar speed but opposite direction. The velocity and density fields are indicative of either a downwelling coastal jet (e.g., Csanady, 1977) or a southward-travelling internal Kelvin wave. Both processes are consistent with the downward slope of isopycnals 5–10 km from the coast, a scale similar to the internal Rossby radius.

With the exception of the warm coastal current, the warmest water in the transect lies at 30–50 m deep or, more generally, at a density of $\sigma_\theta = 26.0\,\mathrm{kg\,m^{-3}}$. This warm layer is kept away from the surface due to the near-surface halocline. Beneath a density of $26.3\,\mathrm{kg\,m^{-3}}$, the warm signal is no longer apparent and water properties across the channel are largely independent of distance across the channel. As noted earlier, this deeper water is formed during wintertime convection.

3.3.3 Modification within Wellington Channel

Above 140 m, Wellington Channel is not an isolated basin. Instead, a complex hydrography emerges owing to inflows from western Lancaster Sound, Maury Channel, and the other channels north of Cornwallis Island. Here we focus on water in the density range $25.9 < \sigma_\theta < 26.3\,\mathrm{kg\,m^{-3}}$, corresponding to the observed range in Maury Channel.

We infer a complex flow in Wellington Channel by first demonstrating that temperature–salinity data do not agree with a simple conceptual circulation comprising northward flow on the eastern side of the channel that diffusively mixes laterally with southward outflow on the western side (Figure 3.7g). The cold inflow from the northwest (Maury Channel) would augment and modify this outflow. Specifically, the blue temperature–salinity curves in each panel of Figure 3.7 should lie between the red curves and the grey curves, which act here as end members. Similarly, the orange curves should lie between red and blue curves. Only in Figure 3.7a is this apparent.

The internal Rossby radius in Wellington Channel ($<$5 km) is an order of magnitude shorter than the channel's width. Hence, the small-scale lateral variability implied by Figure 3.7 is to be expected. Such variability is particularly evident in the unsmoothed temperature fields near the 25.9–$26.3\,\mathrm{kg\,m^{-3}}$ density range (Figures 3.8a–c). In this form, there is clear decorrelation over kilometre scales of temperature on isopycnals, which are also effectively isohalines.

The complex temperature field and the strongly tide-dependent velocities make diagnosing a heat budget for the region infeasible with our cross-sectional snapshots. Further, using ice movement as a proxy for currents in the unmeasured top 10–15 m, we suspect that wind may have directed cold, near-surface waters

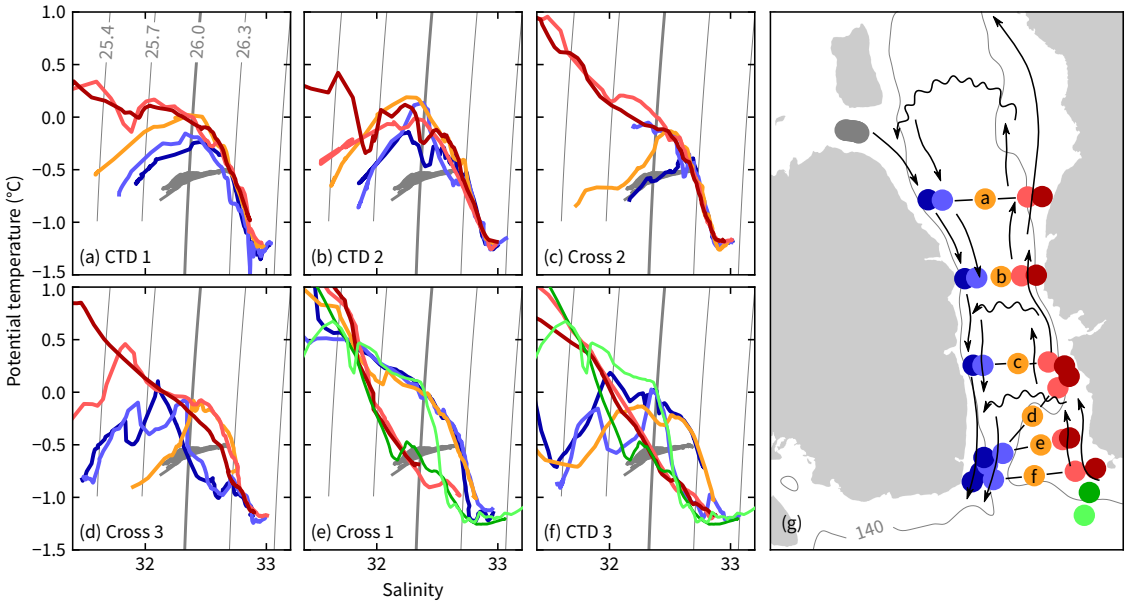

Figure 3.7 – A simple conceptual circulation (panel g) of counter currents and diffusive lateral mixing (wavy arrows) is limited in its ability to explain temperature–salinity patterns in Wellington Channel. *T*–*S* properties for Maury Channel are taken from the initial along-channel transect, and those for western Lancaster Sound (green) are shown on only the panels in which they are deemed relevant. Labels a–f on the map identify the corresponding *T*–*S* panel.

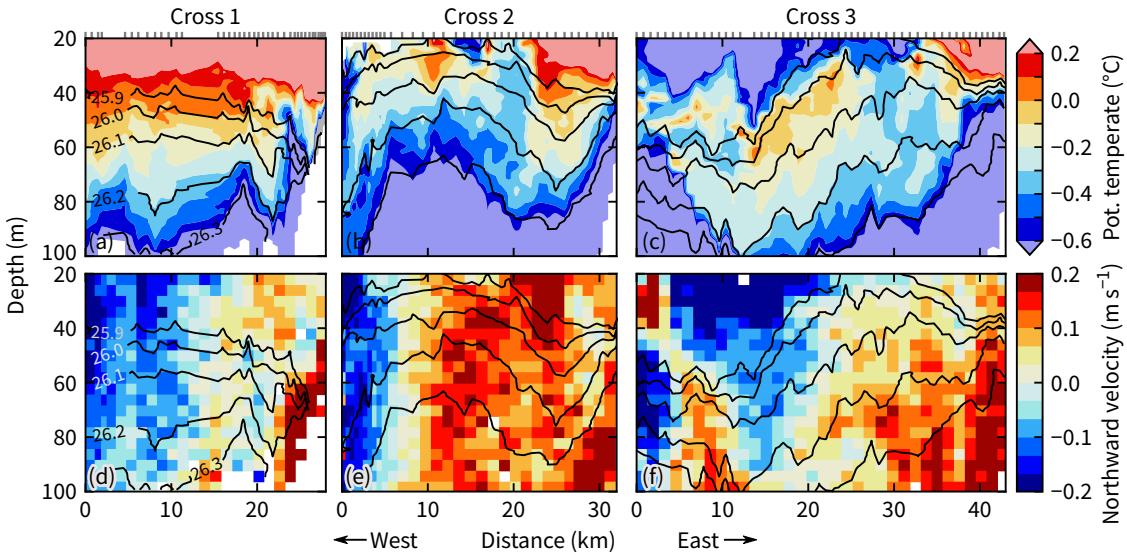

Figure 3.8 – Evidence of small-scale lateral variability from the three MVP transects in Wellington Channel. The temperature colourmap was chosen to be sufficiently wide to encompass most water in the 25.9–26.3 kg m^{-3} density range, but narrow enough to demonstrate the variability on the various isopycnals. Because isopycnals are effectively isohalines at these temperatures, temperature variability on a fixed isopycnal represents variability in water mass hydrographic properties.

southwestward toward McDougall Sound and out of the study area. Together, these challenges mean we cannot quantitatively explain the fate of the cold water inflow through Maury Channel. We note, however, that the location where the cold signal effectively disappears (at $x = 100$ km in Figure 3.5a) coincides with a hydraulic transition discussed in the following section.

3.4 Internal hydraulic flow

The depth-averaged, along-channel current speeds through Maury Channel reach $0.6\,\mathrm{m\,s^{-1}}$ during periods of strong tidal flow. This is three times faster than an estimate of the mode-1 internal wave speed: $c \approx Nh/\pi \approx 0.2\,\mathrm{m\,s^{-1}}$, where the depth h is approximately 50 m and the stratification N is approximately $10^{-2}\,\mathrm{s^{-1}}$. Consequently, the flow in the channel will be internally supercritical ($U > c$) during part of the tidal cycle. In the deeper Wellington Channel, currents are slower, the mode-1 wave speed is larger, and flows are subcritical. Transitions from internally supercritical to subcritical flow are therefore expected at, or near, the steep slope at the eastern end of Maury Channel and possibly elsewhere. Here we examine such transitions using a two-layer, one-dimensional idealization of the observed flow and a simple two-dimensional simulation.

3.4.1 Evidence for an internal hydraulic transition

For each transect, criticality is assessed using the two-layer, composite Froude number G (e.g., Armi, 1986; Lawrence, 1993):

$$G^2 = \frac{u_1}{g' h_1} + \frac{u_2}{g' h_2} \tag{3.1}$$

$$g' = g\frac{\rho_2 - \rho_1}{\rho_2} \tag{3.2}$$

where the velocities u and densities ρ of the top (subscript 1) and bottom (subscript 2) layers are vertical means over each layer of thickness h. An internal hydraulic jump requires a reduction from a value above unity to a value below.

Calculating G from the density and velocity fields is straightforward provided

that (i) an interface is defined and (ii) we assume that the ship's track followed a streamline in the flow. Since there is no strong pycnocline to naturally define the interface, we instead use an internal wave decomposition. Specifically, the depth of the two-layer interface within the channel (at 75–95 km, see Figure 3.9a) comes from the zero-crossing of the horizontal velocity structure of a mode-1 wave, which lies at approximately 25 m (half the depth). The corresponding density at the zero-crossing defines the isopycnal that represents the interface.

Three of the six transects through the channel occurred during a strong eastward current with depth-averaged velocities two-to-three times larger than the mode-1 speed (Figures 3.9b, d, and f). Consequently, the isopycnal representing the two-layer interface drops 50 m at the downstream end of the sill before rebounding 20 m. (MVP profiling during the Repeat 5 transect stopped too early to observe the drop.) The transition to internally subcritical flow occurs approximately 10–20 km east of, and 50 m deeper than, the crest of the sill at 80 km. Eastward of this transition, the current in the lower layer decelerates. Similar observations of a jet over a sill undergoing a hydraulic jump in a channel or fjord are described by Farmer and Denton (1985), Farmer and Armi (1999), Klymak and Gregg (2003), Inall et al. (2005) and Musgrave et al. (2016a).

Flow in the other three transects (Figures 3.9a, c, and e) resembles a two-layer exchange flow with westward flows of 0.3–0.4 $\mathrm{m\,s^{-1}}$ in the upper layer and weak eastward flows in the bottom layer. The shape of the interface also broadly agrees with the theoretical steady-state result of each layer thinning in its respective flow direction (Armi and Farmer, 1986; Farmer and Armi, 1986). However, a steady exchange flow is a dubious interpretation given the time required for such a state to set up relative to the tidal period (Section 3.4.2). Instead, the shape of the interface is more simply explained as the density field equilibrating after the strong eastward current and associated jump. Similarly, transitions about $G = 1$ appear to occur in the exchange flow transects, but their validity is questionable: calculation of G is made noisy by missing ADCP data near the surface and seafloor and internal waves modulating the interface.

Acoustic backscatter adds evidence for our hydraulic interpretation. Although backscatter typically indicates the presence of zooplankton, near topography it can illustrate turbulent structures (e.g., Farmer and Denton, 1985; Seim and Gregg, 1994; Klymak and Gregg, 2004). During the Repeat 1 transect, a period

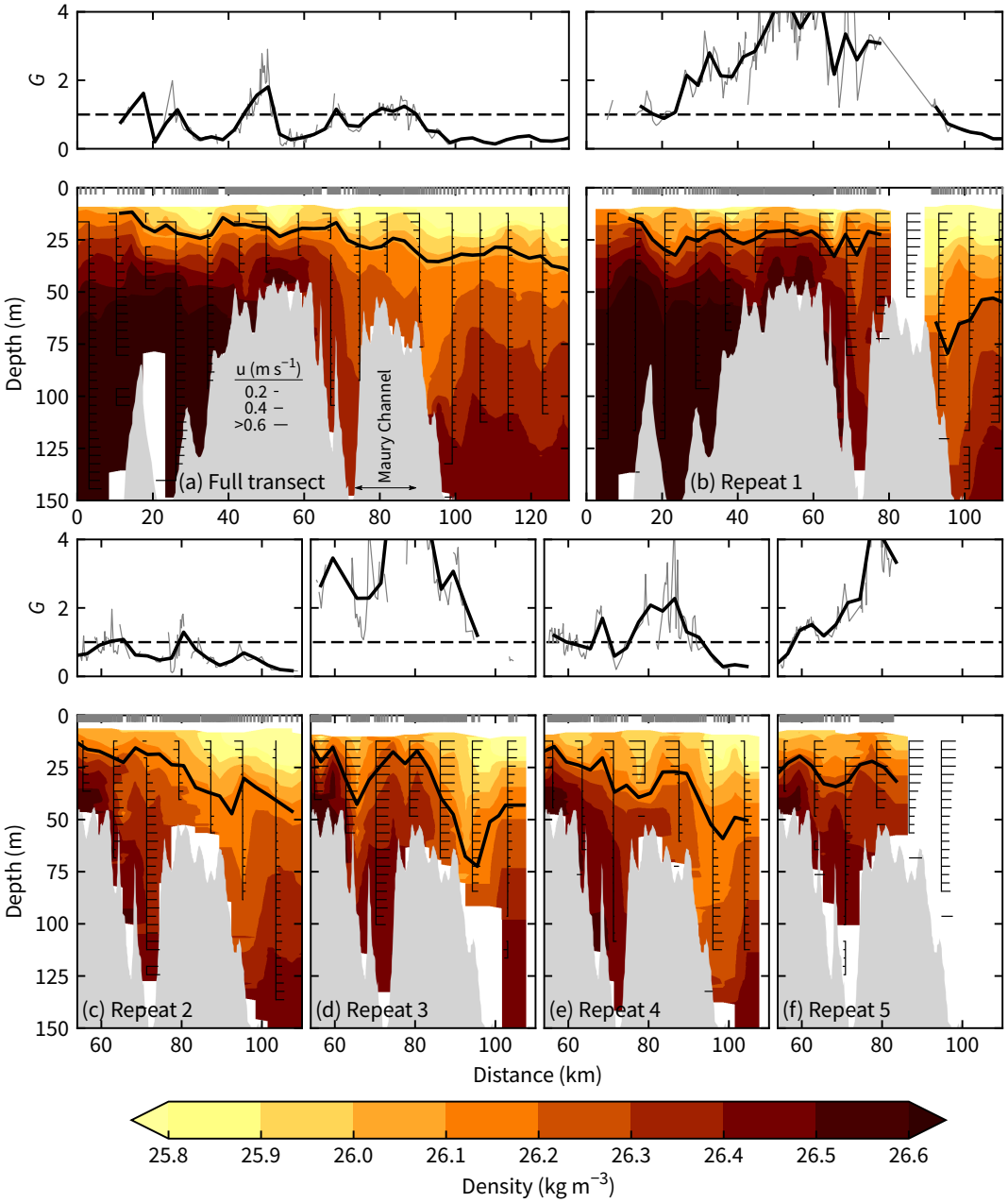

Figure 3.9 – Criticality in along-channel transects. For each transect, the composite Froude number G is calculated by assuming a two-layer flow. The isopycnal representing the interface is shown on the lower panels, together with the density and along-track velocity (stems) fields used to calculate G. Density is smoothed laterally to better depict the large-scale features. Note that values of G are relevant only near Maury Channel, but are extended throughout the full-length transect for completeness.

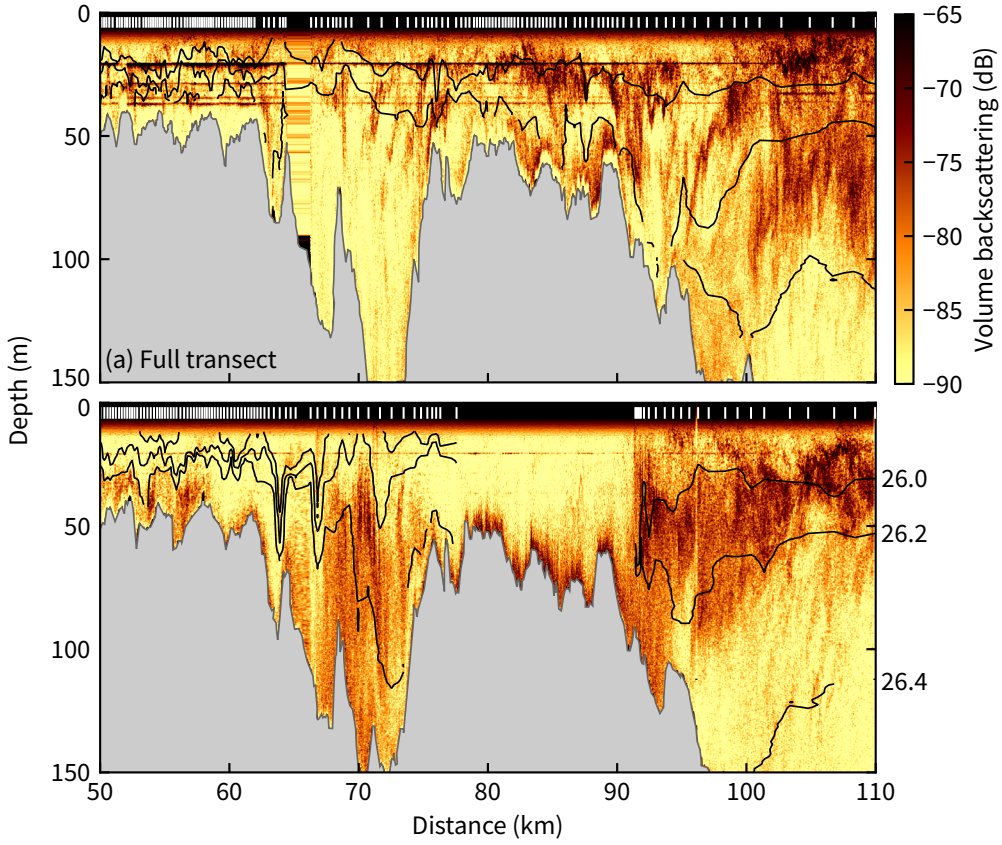

Figure 3.10 – Acoustic backscatter from a 120 kHz echosounder during periods of (a) weak and (b) strong barotropic flow. Associated velocity fields are shown in Figures 3.9a and 3.9b. Note that, unlike most figures in this chapter, the density contours are left unsmoothed.

of internally supercritical flow over the sill, strong backscatter from the 120 kHz EK60 echosounder coincides with the rebounding isopycnals (Figure 3.10b). This also occurs for the other two supercritical transects (Repeats 3 and 5, not shown). Conversely, during weaker flow (Figure 3.10a), the backscatter in this same location is weaker, and the patch of strong backscatter is detached from the topography. Although there is some evidence of what may be Kelvin-Helmholtz billows, especially in Figure 3.10a, the structures are not sufficiently resolved to confirm or deny this.

3.4.2 Time scales for hydraulic flow

A mean eastward flow exists through Maury Channel and is subject to hydraulic control. Although tidal currents modulate this jump, they influence the jump less than the mean flow and the density difference across the sill. This occurs because hydraulic processes over this sill have longer time scales than the tidal period. Two time scales are considered: the time taken for a lee wave to form (Klymak et al., 2010b) and the time taken for upstream flow to adjust.

Flow behaviour near the sill is predominantly governed by the topographic Froude number, $\mathrm{Fr} = U/Nh_m$, where N is the buoyancy frequency, h_m is the height of the sill, and U is a relevant velocity scale, which we take here to be the velocity above the sill during strong flow ($0.6\,\mathrm{m\,s^{-1}}$). The U/N part is a measure of the maximum vertical displacement of a fluid particle given its kinetic energy. Here this is 60 m, which is smaller than the sill height of $\sim$200 m. In this regime of a topographic Froude number less than unity (here $\mathrm{Fr} \approx 0.3$), partial upstream blocking and nonlinear lee waves are expected (Baines, 1987). Deeper water cannot surmount the sill and becomes dynamically passive.

During each tidal period, water near the sill interacts with only a small fraction of the total height and length of the sill. These effective height (h) and length (w) scales imply an aspect ratio $\alpha = h/w$ that determines the relevant horizontal wavenumber of the lee wave. Because the wavenumber components k_x and k_z are related by α, the time taken for a lee wave to form depends on α: lee waves grow more quickly with steeper topography (Klymak et al., 2010b). Note the contrast to the small-obstacle regime ($\mathrm{Fr} \gg 1$) in which horizontal and vertical wavenumbers are independent. Klymak et al. (2010b) derive a time scale of $2\pi/\alpha N$ for the lee wave to propagate one vertical wavelength. For our parameters ($\alpha \approx 75\,\mathrm{m}/15\,\mathrm{km} = 5 \times 10^{-3}, N \approx 10^{-2}\,\mathrm{s^{-1}}$), this equates to 35 hours, an order of magnitude longer than the period over which tidal currents change.

The second time scale, the time taken for the upstream flow field to adjust to critical conditions near the sill, is estimated by dividing the relevant topographic length scale by the rate at which a mode-1 wave can propagate upstream (Pratt and Whitehead, 2008, p. 255). This is difficult to estimate as it depends on the current speed against which the wave propagates. Nevertheless, the length over

which the seafloor upstream changes significantly is several tens of kilometres and the wave speed in, say, 200 m deep water is only $0.5\,\mathrm{m\,s^{-1}}$, implying a time scale of at least a day.

Because hydraulic processes over the sill are slow relative to tidal changes, we see evidence of a hydraulic jump in the form of dropping and rebounding isopycnals even while the tidal current opposes the mean flow. Indeed, this occurs despite the tidal current amplitude being twice the mean current. We estimate the tidal current amplitude and mean current by regressing along-channel current speed against the tidal height at Refuge Cove (Figure 3.1) lagged by 2 hours, which gives the maximum correlation ($r = 0.8$). The regression indicates a tidal current amplitude through the channel of $0.4\,\mathrm{m\,s^{-1}}$ and a mean current of $0.2\,\mathrm{m\,s^{-1}}$.

To confirm the importance of the mean current and density difference across the sill, we perform a two-dimensional, rotationless simulation using the MITgcm (Marshall et al., 1997; Adcroft et al., 2004). Maury Channel is idealized as a smooth bump comprising two half Gaussians that are 200 m tall in 250 m of water (Figure 3.11a). The width scale of each half Gaussian produces similar aspect ratios to the true topography, with the steeper half of the bump on the eastern side. The model extends 300 km to each side with 200 m horizontal grid spacing at the sill crest. This spacing increases 2% per cell away from the sill. (Vertical grid spacing is constant at 1.7 m.) Forcing occurs at the lateral boundaries with both a mean flow and an oscillating component with period T such that the observed tidal current amplitude and mean current over the sill are approximately reproduced. The primary momentum sinks arise from the induced form drag and a quadratic bottom drag ($C_\mathrm{d} = 1 \times 10^{-3}$). The reservoirs to the left and right of the sill contain density fields that are linear representations of the observed density west and east of Maury Channel, respectively. In each reservoir, the initial density field is laterally homogeneous and the two fields join smoothly over the sill (Figure 3.11a). The simulation is spun up for 14 tidal cycles and the 15th tidal cycle is displayed in Figure 3.11.

The simple simulation displays several features observed in the data. A drop in isopycnal depth across the sill exists throughout the tidal cycle due to the mean current and differences in the initial density field. The drop varies in size and is at its largest during and just after the strong eastward flow (cf. Figures 3.9b

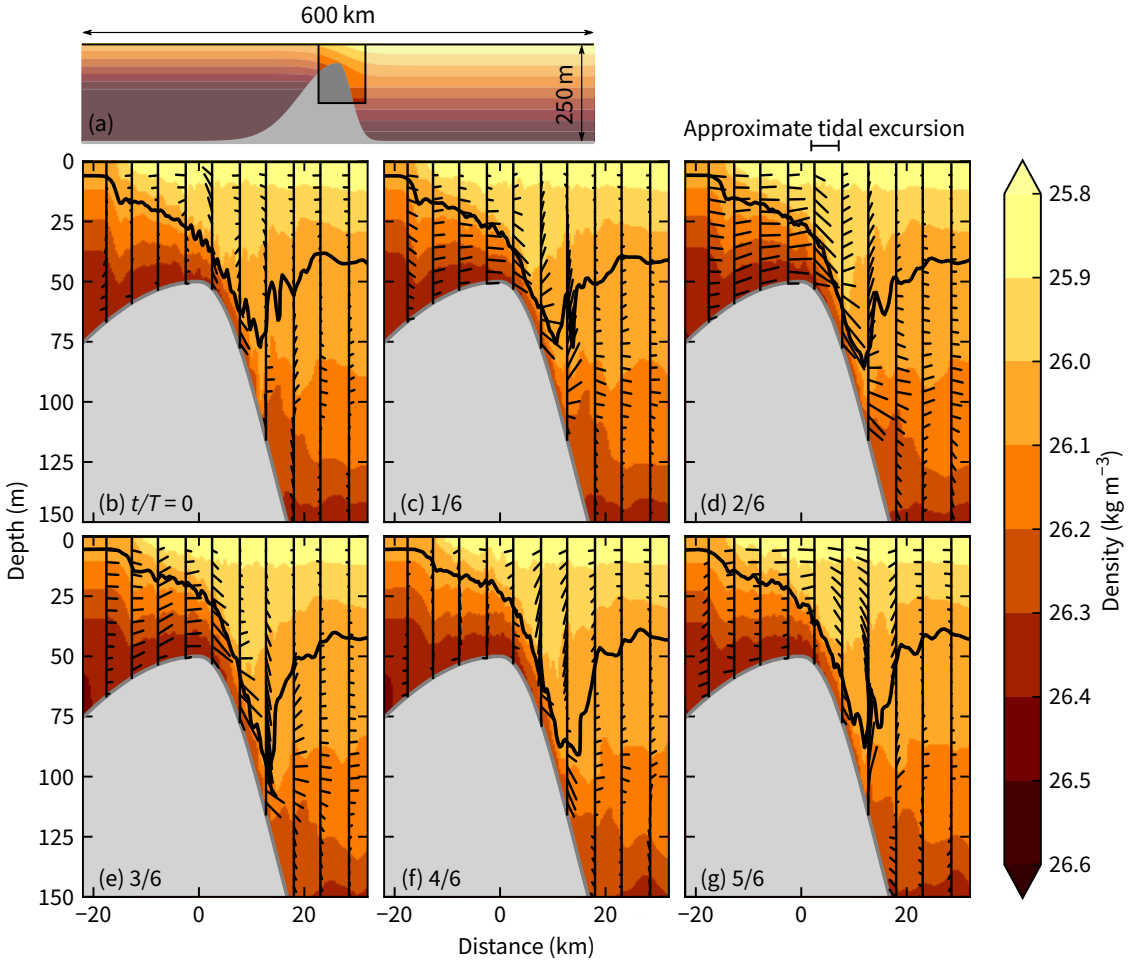

Figure 3.11 – A two-dimensional, idealized, rotationless simulation of flow in Maury Channel. (a) The full model domain and the initial density field. (b–g) Evolution of flow near the sill over the 15th tidal cycle. The model is forced at the boundaries with both a mean flow and an oscillating component with period T. Note that each 26.05 kg m^{-3} isopycnal is traced to aid comparisons between panels.

and 3.9d). During this stage, the jet layer has a high velocity, but the layers above and below are comparatively stagnant. Later in the tidal cycle, a period of westward flow occurs and although it relaxes, the density field still displays a signature of the previous internal hydraulic jump east of the sill.

The equivalent simulation without the initial density difference between the two reservoirs still clearly displays a lee wave but its magnitude is much reduced and it is centred much closer to the crest. Removing the mean flow as well means that the lee wave has insufficient time to develop before the tide changes direction. Alternatively, preserving the density difference while removing the mean forcing produces a jump at the correct depth, albeit a less turbulent jump: the tidally averaged dissipation rate is halved compared to the original simulation. Although the mean barotropic forcing is removed in this last case, mean baroclinic flows of approximately $0.1\,\mathrm{m\,s^{-1}}$ occur over the sill.

3.4.3 Categorizing flow through the constrictions

The four other channels north and west of Cornwallis Island have depths, length scales, and tidal current amplitudes similar to those for Maury Channel (Collins et al., 2011). We therefore expect that flow through each is governed by similar mechanisms and time scales. Indeed, the three channels to the north of the island exhibit similarly sized polynyas in early summer (e.g., Melling et al., 2015). Maury Channel throughflow is therefore a proxy for these other channels and, possibly, Cardigan Strait and Hell Gate, a pair of similarly narrow, albeit deeper, straits 180 km east of Penny Strait that Melling et al. (2008) recognized as important given their combined flux of 0.3 Sv and their advantages as an experimental site.

The channels being considered do not conform to standard, well-studied classifications. In particular, they lie just north of the critical M_2 latitude, and their sill heights are a large fraction of the depth of surrounding channels. The latter factor precludes a large literature that considers small obstacles.

Tidal flow over topography in a region a long distance poleward of the critical latitude generates laterally trapped waves with a decay scale that decreases with latitude (Musgrave et al., 2016b). Closer to the critical latitude, standard linear theories produce solutions that are sensitive to latitude. Theories can be extended to include non-traditional Coriolis components, relative vorticity, and nonlinear

effects (e.g., Vlasenko et al., 2003; Gerkema and Shrira, 2005), which can shift the effective critical latitude a few hundred kilometres in either direction. In in our case, this would either allow freely propagating internal tides or reduce the length scale of trapped waves.

Discussion of freely propagating internal waves may be of secondary importance, however, given the abundance of coastline in the Archipelago. Instead, internal Kelvin waves, which are not restricted by the critical latitude, may be more relevant. For example, Støylen and Fer (2014) found that a major part of the internal wave energy in an Arctic fjord was in the form of an internal Kelvin wave. In our location, even some of the smaller islands north and west of Cornwallis Island may be sufficiently large (larger than the internal Rossby radius) to host clockwise-propagating internal Kelvin waves.

3.5 Toward a regional energy budget

Strong energy loss from the barotropic flow is expected in the central sills area owing to the many shallow constrictions, which enhance both bottom boundary layer dissipation and the effects of stratified flow over topography. Here we estimate terms in the energy budget using our data and existing model results. First, we estimate the incoming energy fluxes for the mean and tidal flows independently. Second, we estimate energy sinks in a manner that accounts for both the mean and tidal flow. For some energy sinks, we consider how our estimates would change if tides were not present, a situation representative of many recent modelling studies (Section 3.1).

The energy budget is necessarily rough in lieu of comprehensive data and modelling. We therefore report terms to only one significant figure unless they are intermediate values within a calculation. Our estimates are summarized in Figure 3.12.

3.5.1 Incoming energy fluxes

Tidal energy fluxes into the channels surrounding Cornwallis Island are $\mathcal{O}(1)$ GW. These estimates (shown in Figure 3.12) are derived from the barotropic tidal model WebTide as described in Appendix A. Note that WebTide's current predic-

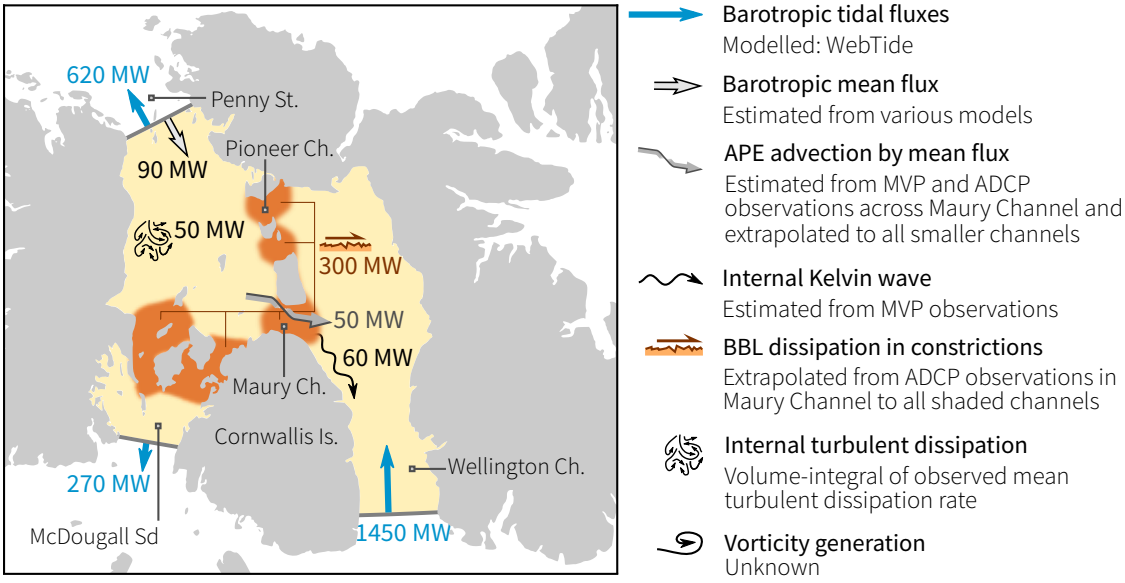

Figure 3.12 – Estimated energy sources and sinks as detailed in Sections 3.5.1 and 3.5.2. Note that the barotropic mean flux depends on a sea surface height difference between the northern and southern ends and is consequently assumed to be zero at the southern exits.

tions depend on the boundary forcing outside the Archipelago and a quadratic drag parameterization, as opposed to taking an inverse approach (e.g., Egbert, 1997). Further, as noted in Section 3.1, WebTide's drag coefficient includes a spatially variable, but temporally fixed, sea ice component. In Penny Strait and McDougall Sound, the drag coefficient is approximately 10×10^{-3}; in Wellington Channel, it is approximately 5×10^{-3} (see Figure 4a in Collins et al., 2011). Because of these increases, WebTide likely overestimates the tidal energy losses in September when the region is ice free. For our purposes this implies that the convergence of tidal energy fluxes in Figure 3.12 of 600 MW is likely overestimated.

The mean flow also loses energy through the central sills area. We first consider the barotropic energy flux E, which for flow in the x direction would become

$$E = \int \rho_0 U \left(U^2/2 + g\Delta\eta \right) \, \mathrm{d}A \tag{3.3}$$

where U is the mean barotropic flow speed, $\Delta\eta$ is the drop in sea surface height across the region being considered, and A is the cross-sectional area with unit normal in the along-channel direction. We take $\Delta\eta$ to be 6 cm between Penny

Strait and Wellington Channel or McDougall Sound (see Figure 3.1b). This value is based on recent modelling studies that exclude tides, which suggest a drop in sea surface height anywhere between 2 and 10 cm (Kliem and Greenberg, 2003; McGeehan and Maslowski, 2012; Wekerle et al., 2013). Given the cross-sectional area of Penny Strait of $5 \times 10^6\,\mathrm{m}^2$ and a velocity of approximately $0.03\,\mathrm{m\,s}^{-1}$ (Chapter 2), the energy flux due to the mean flow through the northern boundary of our region becomes 90 MW. Note that the kinetic energy component is negligible: the flux through Penny Strait would be ∼0.07 MW.

There is also energy lost from the background available potential energy as dense water is advected over the sill. The repeat transects through Maury Channel (see Figure 3.9) indicate that the typical drop in potential energy is $5\,\mathrm{kJ\,m}^{-2}$ from $x = 60$ km to $x = 100$ km. This value is from a vertical integral of potential energy density down to 60 m, below which the water seldom surmounts the sill. We assume this value and the observed mean velocity of $0.2\,\mathrm{m\,s}^{-1}$ (Section 3.4.2) are representative of all the smaller channels north and west of Cornwallis Island, which have a combined width of 50 km. Consequently, there is a 50 MW flux of available potential energy through the smaller channels.

3.5.2 Energy sinks and conversion

In this section we show that dissipation in the bottom boundary layer is likely the mechanism accounting for the strongest losses of energy. The observed tidal current amplitude of $0.4\,\mathrm{m\,s}^{-1}$ in Maury Channel together with the mean flow of $0.2\,\mathrm{m\,s}^{-1}$ (Section 3.4.2) implies a tidally averaged bottom boundary layer dissipation rate of $\rho\, C_\mathrm{d} \left\langle |U|^3 \right\rangle = 0.07$–$0.22\,\mathrm{W\,m}^{-2}$ for $C_\mathrm{d} = 1$–3×10^{-3} . (At neap tide, using current predictions from WebTide, these dissipation values would be approximately half of our observed, near-spring values.) A range for the near-spring values that is dimensionally equivalent to turbulent dissipation can be found by dividing by density and depth, giving dissipation of 1.4×10^{-6}–$4.4 \times 10^{-6}\,\mathrm{m^2\,s^{-3}}$. As will be shown later, this range is two orders of magnitude larger than the interior turbulent dissipation away from bathymetry. By comparison, Wellington Channel is approximately three times deeper than Maury Channel and the observed tidal currents were approximately three times slower. Consequently, $C_\mathrm{d} \left\langle |U|^3 \right\rangle / h \sim 3 \times 10^{-8}\,\mathrm{m^2\,s^{-3}}$.

If we assume that all of the shallow, narrow channels have the same time-dependent velocity as Maury Channel and integrate over the total areal extent of these channels (2000 km^2; dark orange shading in Figure 3.12), we obtain a total loss of order 300 MW. Note that current observations in Pioneer Channel indicate current speeds up to 1.2 $\mathrm{m\,s}^{-1}$ (Topham et al., 1983), but cross-channel and fortnightly variations result in values being comparable to Maury Channel.

The predominance of bottom boundary layer dissipation is likely why WebTide produces realistic tidal current velocities (Appendix A). However, its lack of a mean flow may lead to significant underestimates of $\left\langle |U|^3 \right\rangle / h$ in the shallow channels, which affect predictions of where polynyas form and where primary productivity is enhanced (Hannah et al., 2009). The relative importance to bottom boundary layer dissipation of tidal currents, mean currents, and their interaction is indicated by the value of $\left\langle |U|^3 \right\rangle$ with and without the tidal current or mean current. The absolute value signs preclude a simple algebraic expansion of $\left\langle |U|^3 \right\rangle$, so we determine the values numerically (with units removed for clarity):

$$\begin{aligned} \left\langle |0.2 + 0.4\sin(\omega t)|^3 \right\rangle &= 0.058 \\ \left\langle |0.2|^3 \right\rangle &= 0.008 \quad (14\% \text{ of } 0.058) \\ \left\langle |0.4\sin(\omega t)|^3 \right\rangle &= 0.027 \quad (47\% \text{ of } 0.058) \end{aligned}$$

This form implies that coupling between the tides and the mean flow is a significant component of $\left\langle |U|^3 \right\rangle$, accounting for 39% (100% − 14% − 47%) of the total.

Turbulent dissipation in the interior, although poorly constrained, is likely small relative to that in the bottom boundary layer. To estimate its value, we calculate Thorpe scales from overturns in the rosette CTD profiles following Gargett and Garner (2008) and excluding near-surface measurements where density values are often spurious, presumably owing to the ship's wake. (We cannot use MVP data due to the insufficient vertical resolution described in Section 3.2.) Despite the small number of samples, spatial differences in the dissipation rate were evident: the eight profiles in Penny Strait showed $\varepsilon \approx 10^{-8}$–$10^{-7}\,\mathrm{m^2\,s^{-3}}$, whereas the 16 profiles in Wellington Channel showed $\varepsilon \approx 10^{-9}$–$10^{-8}\,\mathrm{m^2\,s^{-3}}$. Recognizing that Wellington Channel is a larger portion than

Penny Strait of the total volume outlined in Figure 3.12, we simply take the mean dissipation rate from all 24 profiles ($2.2 \times 10^{-8}\,\mathrm{m^2\,s^{-3}}$) as representative of that total volume ($2.0 \times 10^{12}\,\mathrm{m^3}$). This indicates that interior turbulent dissipation accounts for 40 MW.

Enhanced dissipation within hydraulic jumps is expected, but poorly accounted for given the positioning of the CTD profiles. Therefore, energy loss in hydraulic jumps is estimated from the two-dimensional simulation described in Section 3.4.2. The mixing scheme used in that model records the dissipation rate associated with breaking internal waves (Klymak and Legg, 2010). The dissipation rate integrated with depth and distance along the jump gives a per unit width energy loss of $150\,\mathrm{W\,m^{-1}}$. With our earlier conjecture that all the smaller channels near Cornwallis Island behave like Maury Channel, the total loss through the 50 kms of channels would be 8 MW. Consequently, the total loss to turbulent dissipation in the stratified ocean interior rounds to 50 MW. Perhaps surprisingly, energy loss in the hydraulic jump changes negligibly when tides are omitted. Re-running the model described in Section 3.4.2 without the tides results in a similarly sized hydraulic jump with a similar mean dissipation rate. Consequently, hydraulic jumps would represent a small but appreciable energy sink if the region were non-tidal. That is, 8 MW is appreciable relative to the sum of the barotropic mean (90 MW) and available potential energy (50 MW) fluxes.

The final barotropic energy sink we are able to estimate is the conversion of barotropic tidal energy to internal tidal energy. Only in Wellington Channel are there sufficient observations to make an estimate of the internal wave energy flux. We do this by presuming the along-channel density field (Figure 3.5a) is predominantly the manifestation of an internal Kelvin wave moving southward along western Wellington Channel. The along-channel average of the depth-integrated available potential energy density is $6.7\,\mathrm{kJ\,m^{-2}}$. Doubling this (assuming potential and kinetic energies are equipartitioned) gives the total energy density per unit area. The product of this value with an appropriate width scale and speed gives the energy flux. A width scale of 11 km is estimated empirically from inspection of cross-channel transects and accounting for the decrease in wave amplitude with distance from the coast. The speed used is the mean wave speed of a mode-1 internal wave ($0.42\,\mathrm{m\,s^{-1}}$) in Wellington Channel derived from a modal decomposition of density profiles. The internal Kelvin wave in western

Wellington Channel has an estimated energy flux of 60 MW, one-fifth of our 300 MW estimate of bottom boundary layer dissipation in the smaller channels.

3.5.3 Interpreting the energy budget

In some respects, flow in the central sills area is analogous to that in a fjord. In both cases, sills govern the hydrography and tidal and mean flows play comparable roles. We find, however, that unlike most fjords, bottom boundary layer dissipation is the dominant component of the barotropic energy loss. A contrasting example is Knight Inlet, where bottom boundary layer dissipation accounts for 1 of 22 MW, whereas internal wave generation accounts for 15 MW (Klymak and Gregg, 2004).

The predominance of bottom boundary layer dissipation results from the larger length scales in the central sills area. First, the length scale of the sill considered in this chapter is tens of kilometres, at least an order of magnitude larger than typically found in fjords. Bottom boundary layer dissipation is therefore strong over a much larger area. Second, the wider channels studied here, e.g., Wellington Channel, are of order 10 internal Rossby radii wide. Consequently, Kelvin waves, the only efficient mechanism to propagate baroclinic energy away from the sill (Section 3.4.3), occupy only a fraction of the channel width.

Although the Kelvin wave energy flux in Wellington Channel is small compared to bottom boundary layer dissipation, it is still significant given that Wellington Channel is one of three channels in the network under consideration (Penny Strait and McDougall Sound are the other two). Indeed, our estimates indicate Kelvin waves are radiating away more energy than is being lost to turbulent dissipation in the interior of the water column. We lack, however, a simple scaling law to estimate how much energy is likely to be converted into Kelvin wave energy based on external forcing, geometry, and stratification. Further, of the three channels, Wellington Channel appears most conducive to relaying Kelvin waves; the other two channels feature sharp headlands, which may lead to eddy generation instead.

Eddies are not considered in our budget. This does not imply they are insignificant, but rather that we lack sufficient data to make any estimate of their magnitude. Further, their implications for the volume-integrated budget depend

on whether they leave the region. Many of the smaller islands and headlands may generate eddies that ultimately dissipate as local turbulence. Conversely, there is potential for eddies to advect energy out of the system. For example, Klymak and Gregg (2004) and Inall et al. (2005) estimated that eddy shedding accounted for 12% and 30–40% of their respective total barotropic losses for Knight Inlet and Loch Etive.

Because the energy losses described here scale nonlinearly with velocity, a first step to improving a regional energy budget is to obtain estimates of the time-varying total (mean + tidal) velocity in the many channels, particularly the smaller channels, which we have demonstrated to play a disproportionately large role. If, as we presumed earlier, these other channels have similar velocities to Maury Channel, then our energy budget implies that adding tides to models will reduce discrepancies between simulated and observed fluxes (Section 3.1).

3.6 Conclusion

Shallow sills in the centre of the Archipelago separate two distinct water masses. High-spatial-resolution observations through Maury Channel, enabled by a Moving Vessel Profiler, elucidate details of the interaction between the two. Much of the densest water flowing toward the Atlantic is blocked and effectively passive. The extent into Wellington Channel of the colder, denser water that does surmount the sills appears limited by internal hydraulics. Specifically, its cold signal on the 26.1 $\mathrm{kg\,m^{-3}}$ isopycnal disappears at approximately the same location as an internal hydraulic jump. Similarly, an attempt to track the temperature–salinity properties across the density range of the outflow (25.9–26.3 $\mathrm{kg\,m^{-3}}$) was largely unsuccessful. These properties instead highlight the smaller-scale lateral variability within the larger channels.

Numerically reproducing the internal hydraulic jump that occurs at the eastern end of Maury Channel requires both a mean flow and a density difference across the sill. Without these, there is insufficient time within each period for internal hydraulics to play a controlling role. These requirements, together with our location north of the critical M_2 latitude, make it difficult to either categorize the flow through the channel or to compare it against other oceanic channels.

However, Maury Channel is a reasonable proxy for the many other smaller channels in the central sills area. We speculate that the governing mechanism in Maury Channel, internally controlled flow that is modulated by the tide, may also govern in these other channels. This control and our inferences of strong tidally driven bottom boundary layer dissipation provide possible explanations for the overestimate in volume flux by large-scale, tideless models.

Further speculation is limited by the two-dimensionality of our transects. In particular, we lack an estimate of the three-dimensionality of the flow within Maury Channel or near the jump. Hence, we do not know if lateral recirculations are a first-order feature. Similarly, the pathways through the central sills area are poorly constrained: the volume fluxes through the nearby channels relative to that of Maury Channel are not observationally known.

Surveying or modelling this tidally active, multi-channelled region is a logistical challenge. Typical three-dimensional regional models have about a 4 km grid, which does not fully resolve the significant physical processes that we have described. Here we have provided a phenomenology against which modelling studies may compare and we have identified a need for further observations, particularly velocity and its tidal dependence, within the narrower channels given the implication from our energy budget of their disproportionately important roles.

Acknowledgments

We thank Rowan Fox, Hauke Blanken, and the CCGS Amundsen crew for their help obtaining data. Funding is provided through the Canadian Geotraces project, part of the Natural Sciences and Engineering Research Council of Canada's Climate Change and Atmospheric Research (CCAR) initiative.

The data presented herein were collected while aboard the Canadian research icebreaker CCGS Amundsen and made available by the Amundsen Science program, which is supported by the Canada Foundation for Innovation Major Science Initiatives Fund. The views expressed in this publication do not necessarily represent the views of Amundsen Science or that of its partners.

The data as processed by the authors is available at `http://kghughes.com/`

`data`. Alternatively, the data is archived by ArcticNet in the Polar Data Catalogue (`https://polardata.ca`) and can be searched using the following CCIN references numbers: 12519 (MVP), 12713 (CTD), 12718 (ADCP), and 12841 (EK60).

We thank Laurie Padman and a second, anonymous for several recommendations resulting in a much clarified manuscript.

Chapter 4

Tidal conversion in a channel poleward of the critical latitude

Abstract

In two dimensions and poleward of the critical latitude, the conversion of barotropic to baroclinic tidal energy is zero in the linear, inviscid limit. However, in settings such as high-latitude fjords and channels in the Canadian Arctic Archipelago, walls support radiating internal tides as Kelvin waves. These fundamentally three-dimensional systems are investigated with a suite of numerical simulations in rectangular channels of varying width featuring idealized, isolated ridges. Even in channels as wide as five times the internal Rossby radius, tidal conversion can remain as high as predicted by an equivalent two-dimensional, non-rotating system. Curves of tidal conversion as a function of channel width, however, do not vary monotonically. Instead, they display peaks and nulls owing to interference between the Kelvin waves along the wall and similar waves that propagate along the ridge flanks, the wavelengths of which can be estimated from linear theory to guide prediction. Because the wavelengths are comparable to width scales of Arctic channels and fjords, the interference will play a first-order role in tidal energy budgets.

Submitted as

Hughes K.G. and J. M. Klymak (2018) Tidal conversion and dissipation at steep topography in a channel poleward of the critical latitude. *J. Phys. Oceanogr.*

4.1 Introduction

The Arctic is home to numerous channels and fjords that are typically 2–3 times wider than the internal Rossby radius (Cottier et al., 2010). Similarly, the larger channels in the Canadian Arctic Archipelago can be an order of magnitude wider (McLaughlin et al., 2004). Consequently, rotation governs hydrography and energetics. In these settings, and the ocean as a whole, internal tides generated by stratified tidal flow over obstacles are the starting point in an energy cascade from the barotropic tides to irreversible mixing (Munk and Wunsch, 1998; Klymak and Gregg, 2004; Inall et al., 2005; Arneborg et al., 2017). In better-studied, mid-latitude fjords, energy extracted from the barotropic tide is often the primary source for driving the mean circulation (Freeland and Farmer, 1980; Inall and Rippeth, 2002). Furthermore, during periods of stagnation, mixing ultimately induced by radiated tides is the only effective mechanism to mix deep water within a fjord (Stigebrandt and Aure, 1989, and references therein).

Much of a given system's state is concisely captured by three parameters (e.g., Sarkar and Scotti, 2017): the conversion of barotropic to baroclinic energy, the ratio of barotropic tidal energy dissipated locally to the total lost; and the energy transported by internal waves elsewhere. These influence the location, strength, and mechanisms of mixing. Several parameters can help predict the fate of barotropic tidal energy: internal criticality over the topography; the topographic Froude number, Fr; and the ratio of internal wave slope to topographic slope, γ. The last parameter is ill-defined in locations poleward of the critical latitude where the Coriolis frequency f exceeds the tidal frequency ω. This leads to a fourth important parameter: whether the tide is super- or sub-inertial.

In the two-dimensional, linear limit, freely propagating internal tides exist only equatorward of the critical latitude (29.7° for K_1 and 74.5° for M_2). These are termed superinertial internal tides. Linear tidal conversion drops quickly as this latitude is approached, decreasing as $\sqrt{1-(f/\omega)^2}$ (Llewellyn Smith and Young, 2003). Poleward of the critical latitude, still in two dimensions, there is an evanescent response but the only tidally averaged conversion results from nonlinearities and turbulence because linear perturbations in pressure and cross-ridge velocity are 90° out of phase (see, e.g., Musgrave et al., 2016b). Consequently, the fraction of energy lost from the barotropic tide that is dissipated

locally is close to 1, but the amount of energy extracted from the barotropic tide in absolute terms is small compared to low- and mid-latitudes.

Two types of propagating waves exist that thereby allow for a nonzero tidally averaged conversion: (i) coastal trapped waves (e.g., Huthnance et al., 1986), a classification that includes internal Kelvin waves as a limiting case, and (ii) high-frequency internal waves generated by nonlinearities. Rippeth et al. (2017) observe and simulate packets of high-frequency internal waves generated by internally supercritical flow at the edge of Spitsbergen Bank (75°30′ N) and suggest this is a key mechanism linking tides to turbulence poleward of the critical latitude. Støylen and Fer (2014) describe similar high-frequency wave packets in Van Mijenfjorden, Svalbard (77°45′ N), but in this case, the fjord setting also permits internal Kelvin waves at the tidal frequency and these were found to transport the majority of the internal wave energy away from the sill.

Internal Kelvin waves behave as non-rotating internal waves in the direction in which they travel. Therefore, it is reasonable to expect that much of the literature for the two-dimensional (x–z) case is applicable to this chapter in which we consider an isolated bump that is independent of y (Figure 4.1). Specifically, we expect tidal conversion to scale as U_0^2 and N where U_0 and N are the tidal current amplitude and the buoyancy frequency near the crest of the topography, respectively. Further, the majority of the energy flux is likely contained in the first internal mode (Llewellyn Smith and Young, 2003; St. Laurent et al., 2003). These scalings, however, provide no clues as to how conversion will scale with channel width.

The simulated conversion in a channel is influenced strongly by topographically trapped internal wave interference as will be shown later. Curiously, interference also occurs in many nominally two-dimensional scenarios. For example, conversion is controlled by the distance between peaks in idealized, periodic topography (Balmforth and Peacock, 2009). A realistic example of this occurs in Luzon Strait where strong conversion results from constructive interference of semidiurnal internal tides generated at approximately parallel ridges (Buijsman et al., 2012; Klymak et al., 2013). A related example, albeit only significant for short (small fractional height) obstacles, is conversion by a tophat ridge, where the distance between the ends of the tophat is a controlling factor (St. Laurent et al., 2003). An example that involves subinertial diurnal internal tides occurs

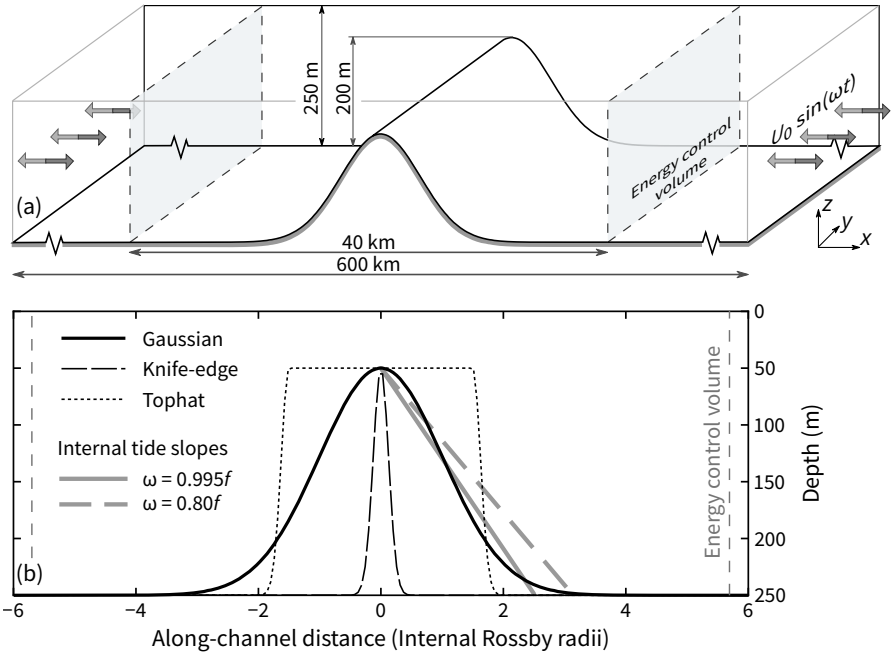

Figure 4.1 – Domain and topographies used in this chapter. Note that, as evident from the wave slopes, the ends of the energy control volume are approximately one mode-1 wavelength from the center.

at Izu-Oshima Island near Japan (34°N) where the natural period for an internal Kelvin wave circumnavigating the 52 km-circumference island is close to the diurnal tidal period. Masunaga et al. (2017) demonstrate that the forcing tidal frequency controls the Kelvin wave magnitude. Mihanović et al. (2014) provide similar results for a 5 km-circumference island in the Adriatic Sea (42°N).

In this chapter, we undertake a suite of three-dimensional numerical simulations of tidal flows in a rectangular channel over three idealized topographies (Section 4.2). The initial, qualitative results (Section 4.3) demonstrate the controlling role of the internal waves that travel along the ridge flanks. Details of these waves are far from trivial (Section 4.4) and cause complicated but predictable changes in tidal conversion as channel width varies (Section 4.5). The importance of tidal conversion to the barotropic energy budget and the subsequent fate of baroclinic energy is evaluated (Section 4.6) and leads to discussions on the practical relevance of this idealized study and the importance of three-dimensionality for subinertial tides (Section 4.7).

Table 4.1 – Summary of all simulations undertaken. Bolded values identify the combination of parameters used in the example in Section 4.3.

Topography	Channel widths (km)	U_0 (cm s^{-1})	ω/f
Variable channel width (Sections 4.3, 4.5 and 4.6.1)			
Gaussian	0.2, 0.4, 0.6, 0.8, 1.2, 1.6, 2, 3, 4, 6, 7, 8, 10, 12, 13, 14, 15, 16, 19, 23, **26**, 29, 32, 37, 42, 48, 56, 65	**4**	0.80, **0.995**
Tophat		4	0.80, 0.995
Knife-edge		4	0.80, 0.995
Variable frequency (Section 4.4.3)			
Gaussian	40	4	0.70, 0.75, 0.80, 0.85, 0.90, 0.95, 0.995, 1.05
Variable forcing (Section 4.6.2)			
Gaussian	26	1, 2, 4, 6, 9, 12, 16, 20, 24	0.995

4.2 Methods

4.2.1 Geometry and forcing

Several three-dimensional, idealized simulations (Table 4.1) of stratified tidal flow over an idealized obstacle are undertaken with the MITgcm (Marshall et al., 1997; Adcroft et al., 2004) together with an online barotropic–baroclinic energy decomposition (Kang and Fringer, 2012; Klymak et al., 2016). The north–south aligned obstacle lies at the centre of a 600 km-long east–west channel (Figure 4.1a). Our analysis will concentrate on a Gaussian obstacle, with knife-edge and tophat simulations providing further clarification (Figure 4.1b). Such obstacles are frequently used in two-dimensional studies (e.g., St. Laurent et al., 2003; Llewellyn Smith and Young, 2003; Klymak et al., 2010a, 2013; Musgrave et al., 2016b).

The chosen dimensions and oceanographic parameters are loosely based on a sill described in Chapter 3 where internal Kelvin waves have been observed. Specifically, a 200 m-tall obstacle sits in 250 m of water with a constant stratification of $N = 6.2 \times 10^{-3}\,\mathrm{s}^{-1}$ ($\Delta\rho = 1.0\,\mathrm{kg\,m}^{-3}$ over 250 m). The obstacle is always

steeper than a non-rotating internal tide slope (Figure 4.1b).

Within 20 km either side of the obstacle crest, the model grid spacing is fixed at $\mathrm{d}x = 200$ m. Beyond this, grid spacing increases 1.5% per cell. In the cross-channel direction, $\mathrm{d}y$ is constant at 200 m and small relative to the internal Rossby radius $L_\mathrm{R} = NH/\pi f = 3500$ m. Vertical grid spacing is also constant (60 cells, $\mathrm{d}z = 4.2$ m). Given the 48:1 aspect ratio of grid cells, all simulations are hydrostatic (see Berntsen et al., 2009).

Tidal currents are forced at the boundaries using 100 km-long velocity sponges with relaxing time scales of 100 s and 1000 s at the outer and inner edges of the sponges, respectively. A phase difference between the two sponges is included to produce a progressive tidal wave. Furthermore, tidal forcing is linearly ramped over the first two tidal cycles. In most simulations, tidal currents in the deep water are kept moderate (4 cm s^{-1}) to produce predominantly, but not perfectly, linear behaviour. Faster tides are considered in Section 4.6.2. Counteracting the tidal forcing is the induced form drag and quadratic bottom drag ($C_\mathrm{d} = 1 \times 10^{-3}$). A free slip condition with no drag is applied at the walls. Viscosity and diffusivity are parameterized based on density overturns (Klymak and Legg, 2010) with background values of 1×10^{-5} m^2 s^{-1} for both parameters.

All simulations use a single tidal constituent, with most simulations using a period of either 44 640 s or 55 800 s. The former is a close approximation to the M_2 tidal period and the latter is simply a hypothetical tide with a period 25% longer. The Coriolis frequency is set based on a latitude of 76°, slightly poleward of the critical latitude for our approximate M_2 tide (74.8°, $\omega = 0.995f$) and well poleward for the longer period tide (50.5°, $\omega = 0.80f$). Both tidal periods conveniently divide into several integer time steps. Here $\mathrm{d}t = 10$ s and easily satisfies the CFL criterion for internal waves, which travel at ≤ 0.5 m s^{-1}. Conversely, surface waves travel at 50 m s^{-1}, so an implicit free surface is used.

4.2.2 Barotropic–baroclinic energy decomposition

We treat the fate of barotropic tidal energy in a tidally steady system following Kang and Fringer (2012) with some simplifications to be described. Barotropic tidal energy is lost to either bottom boundary layer dissipation or converted to baroclinic energy. After conversion, energy may (i) leave the system as an

internal wave flux, (ii) dissipate in the interior, or (iii) dissipate in the bottom boundary layer. The vertically integrated energy budgets become

$$\nabla_H \cdot \langle \overline{\mathbf{F}_0} \rangle = - \langle \overline{C} \rangle - \langle D_0 \rangle \tag{4.1}$$

$$\nabla_H \cdot \left\langle \overline{\mathbf{F}'} \right\rangle = \quad \langle \overline{C} \rangle - \langle D' \rangle - \langle \bar{\varepsilon} \rangle \tag{4.2}$$

where $\mathbf{F}$ is a tidal energy flux, C is conversion from barotropic to baroclinic energy, D is bottom boundary layer dissipation, and ε is turbulent dissipation in the interior. A subscript 0 and a prime denote barotropic and baroclinic components, respectively, ∇_H is horizontal divergence, overbars denote depth integrals, and angle brackets denote tidal averages. With the exception of Section 4.3 where snapshots are shown, all tidal energy terms we present are averaged over the seventh tidal cycle.

The conversion term C is a focus of this chapter and the link between the individual energy budgets for barotropic and baroclinic energies. It is dominated by its linear, hydrostatic component:

$$C_{\text{lin}} = \overline{\rho' g W} \tag{4.3}$$

where ρ' is a density perturbation, and $W = W(z)$ is the vertical velocity that results from convergence or divergence of horizontal barotropic flow between the seafloor and z. Our volume-integrated budgets additionally include the small unclosed components of C documented by Kang (2011, see Equation 5.89).

After conversion, baroclinic energy either dissipates locally (defined as within the 40 km-long energy control volume centred about the obstacle as in Figure 4.1a) or propagates out of the system. The component that leaves is described concisely by the depth-integrated baroclinic flux $\overline{\mathbf{F}'}$:

$$\overline{\mathbf{F}'} = \overline{\mathbf{u}' p'} \tag{4.4}$$

where p' is the pressure perturbation relative to a horizontally independent background state and $\mathbf{u}'$ is the velocity with the depth average removed. We have ignored the advective and diffusive components of $\overline{\mathbf{F}'}$ as these are negligible here.

Bottom boundary layer dissipation is decomposed into barotropic and baro-

clinic components:

$$D_0 = \rho_0 C_\mathrm{d} \left|\mathbf{u}_H\right| (uU + vV) \tag{4.5}$$

$$D' = \rho_0 C_\mathrm{d} \left|\mathbf{u}_H\right| (uu' + vv' + w^2) \tag{4.6}$$

Uppercase, lowercase, and primed velocities are the barotropic, complete, and baroclinic components, respectively. A subscript H denotes the horizontal component.

Turbulent dissipation ε is not decomposed. Doing so is arguably beyond the point of diminishing returns. Instead, we have placed ε in the baroclinic energy budget as we expect that it predominantly results from processes occurring after conversion to baroclinic energy.

4.3 Phenomenology

Much of the behaviour of the stratified tidal flow is apparent in snapshots of baroclinic fields (Figure 4.2) and energy components (Figure 4.3). In this section, we describe this behaviour for a moderately wide (26 km, $7.3L_\mathrm{R}$) channel. This channel is geometrically comparable to Van Mijenfjorden in Svalbard, which has been studied observationally (Støylen and Fer, 2014) and thereby provides some qualitative validation of the processes we study here.

Internal Kelvin waves are the dominant signal in the along-channel baroclinic velocity fields near the boundary. The *e*-folding scale of 1 Rossby radius is evident in map view (Figure 4.2a) and their equivalence to non-rotating internal waves is evident in cross-section (Figure 4.2c); that is, they are beam-like with slopes of $\sqrt{(N^2 - \omega^2)/\omega^2}$, which equates to approximately 0.023 for the $\omega = 0.995f$ tide or equivalently $3.1L_\mathrm{R}/250\,\mathrm{m}$ depth. Note that the beams in Figure 4.2 are diffuse because low-mode waves dominate; high-mode waves propagate away from the topography more slowly and dissipate locally (Klymak et al., 2010a).

The response away from the wall is a combination of transient near-inertial waves and the expected linear, subinertial response (Figures 4.2e and 4.2f). Linear theory for the two-dimensional subinertial case predicts that baroclinic velocities decay exponentially from the obstacle with an inverse decay scale $\hat{k}$ (Musgrave

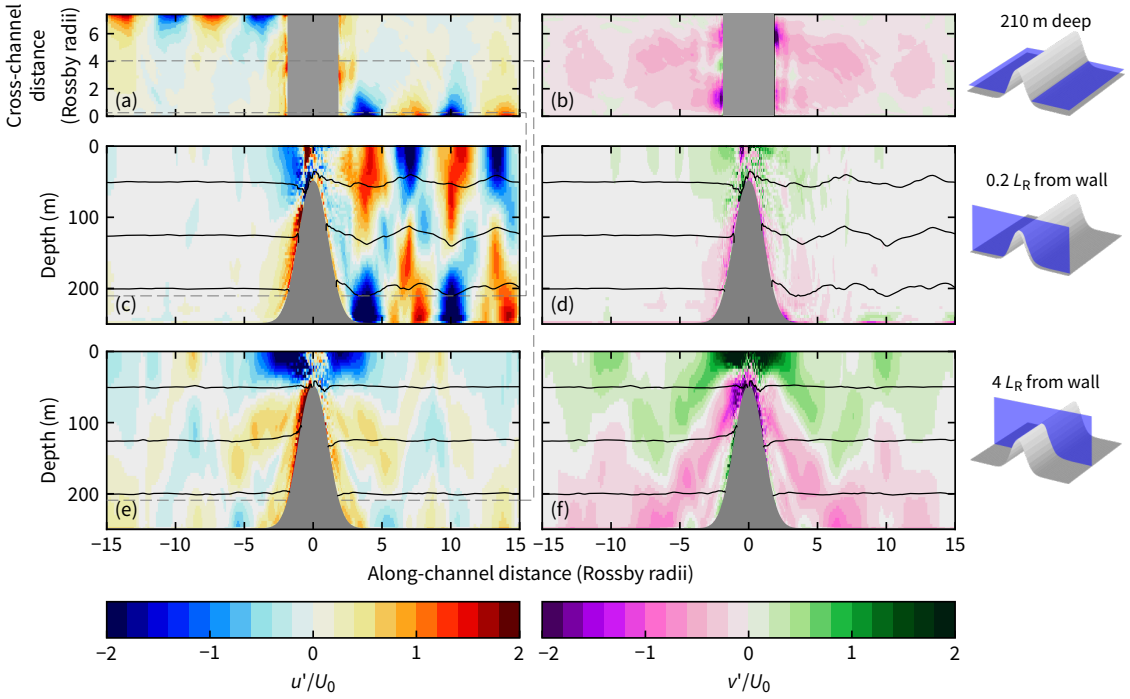

Figure 4.2 – A snapshot of baroclinic velocities and isopycnals after seven tidal cycles. Tidal forcing in the deep water has an amplitude of $U_0 = 4\,\mathrm{cm\,s^{-1}}$ and a frequency of $\omega = 0.995f$.

et al., 2016b):

$$\hat{k} = \frac{\pi}{HN}\sqrt{f^2 - \omega^2} \tag{4.7}$$

For our chosen parameters, $\hat{k}$ corresponds to a decay scale of 34 km $\approx 10L_\mathrm{R}$, which is consistent with Figure 4.2.

Looking at these fields from an energy perspective (Figure 4.3) effectively filters out the near-inertial waves as these have negligible associated energy fluxes. Baroclinic energy density and fluxes (Figures 4.3a–c) predominate in two areas: on the flanks of the topography and beside the walls. Details of the waves travelling along the flanks are discussed in Section 4.4. Here we simply note that they are generated by convergence and divergence at the northeast and southwest parts of the bump and because they are travelling beside an inclined boundary, the baroclinic energy density decays more slowly in the x direction (compared to away from the vertical walls in the y direction).

The internal waves (at the tidal frequency) along the flanks explain much of

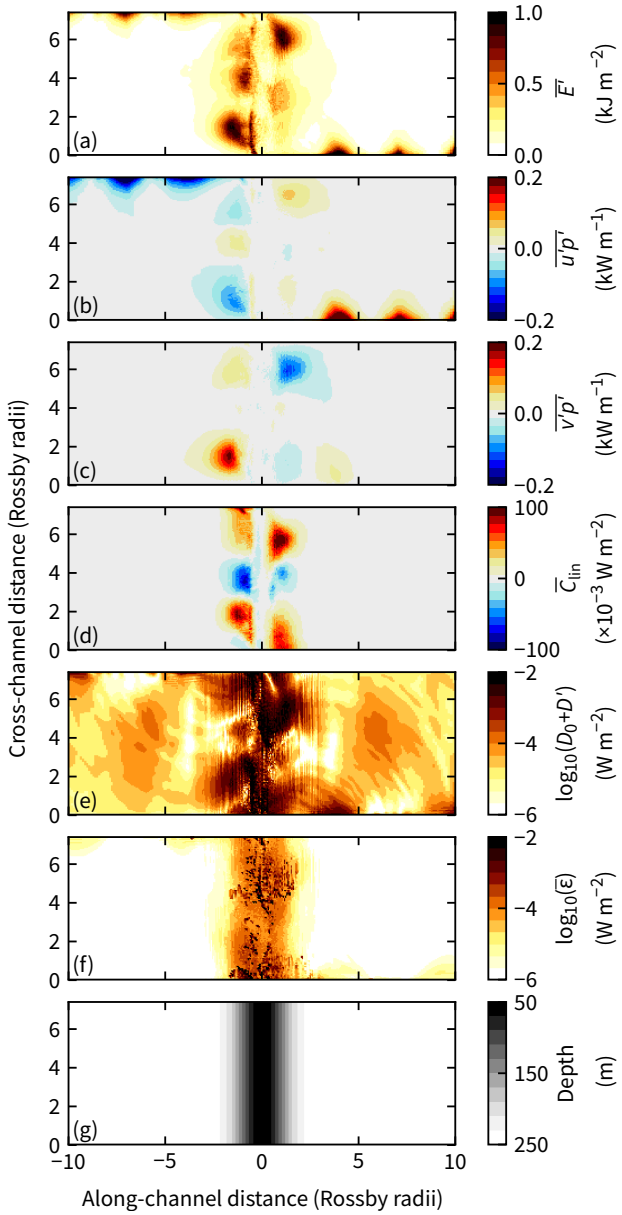

Figure 4.3 – Snapshots of energy terms after seven tidal cycles. Corresponding fields are shown in Figure 4.2. (a) Baroclinic energy density. (b, c) Eastward and northward energy flux via internal waves. (d) The linear component of the conversion rate. (e) Bottom boundary layer dissipation. (f) Turbulent dissipation due to overturning. (g) Obstacle bathymetry.

the conversion term's spatial distribution (Figure 4.3d). For the case shown, the width of the channel 1.8 times the wavelength of the along-flank wave. When this wave interacts with the vertical velocity induced by the barotropic tidal forcing, it leads to lobes of positive and negative conversion. During this snapshot, there is one negative and two positive lobes on each side of the obstacle. The same is true for maps of tidally averaged conversion (not shown). Negative conversion is typically explained as resulting from interaction between remotely and locally generated internal tides (e.g., Kang and Fringer, 2012; Fer et al., 2015; Masunaga et al., 2017). In our case, however, it is better described as the interaction between the currently generated and previously generated internal tides.

Bottom boundary layer dissipation ($D_0 + D'$; Figure 4.3e) is the only term shown that is not concentrated either near the wall or near topography. For example, wave interference, including with the barotropic tide, leads to locally large and small velocities and is responsible for much of the observed distribution. A radial pattern is also evident and occurs because waves are generated as the along-obstacle waves scatter at the northwest and southeast ends of the obstacle. These effects are of minor importance, however, as dissipation levels away from the walls or the obstacle are comparable to what they would be in an equivalently forced system without topography.

Most turbulent dissipation in the interior water column occurs over the obstacle where high-mode waves dissipate and strong nonlinearities occur. Appreciable levels of turbulence also occur along walls. Vertical slices near the walls (not shown) show that turbulence is strongest at mid-depth where isopycnal perturbations are largest and near the seafloor where baroclinic convergence induces instabilities.

4.4 Structure of the along-obstacle waves

The along-obstacle waves are responsible for the spatial pattern of tidal conversion as described in the previous section. Moreover, the extent to which the positive and negative regions cancel controls how conversion and baroclinic flux divergence vary: curves of tidal conversion as a function of channel width display peaks and nulls (Figure 4.4) rather than varying monotonically as may

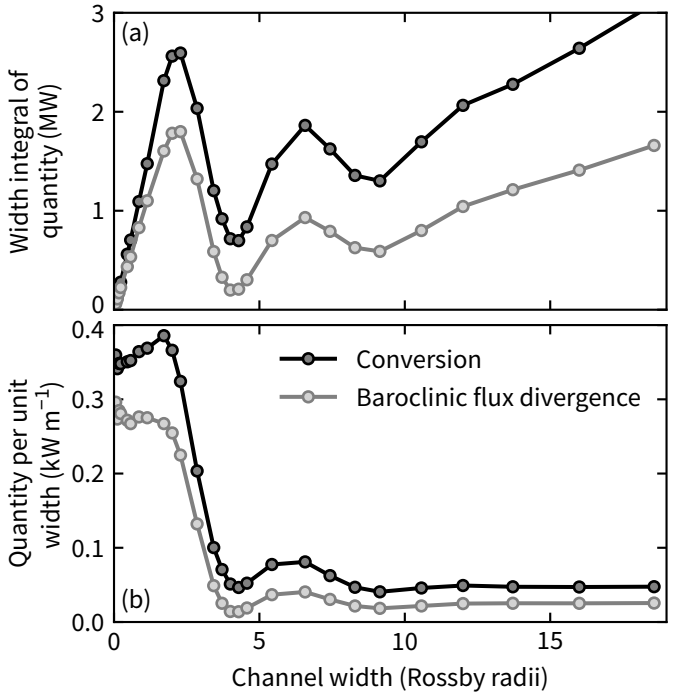

Figure 4.4 – Tidal conversion in channels of varying width with a Gaussian obstacle. The resulting baroclinic flux divergence from the energy control volume is smaller owing to local dissipation.

be reasonably expected. In this section, we develop a linear model of the along-obstacle waves, which are conceptually similar to internal Kelvin waves beside a wall and a step. As background, we first recap the properties of such waves.

4.4.1 Internal Kelvin waves

If an internal Kelvin wave is travelling parallel to a vertical wall at $x = 0$ and is hydrostatic and geostrophically balanced, then velocities normal to the wall are identically zero and the wave solution is separable in y and z. For example, with constant buoyancy frequency, the mode-1 along-channel velocity is

$$v' = \mathcal{V}(z) \exp\left(i(\omega t - k_y y)\right) \exp\left(-x/L_\mathrm{R}\right) \tag{4.8}$$

where $\mathcal{V}(z)$ is a mode shape. Tidal frequency ω and along-channel wavenumber k_y are related by the hydrostatic dispersion relation:

$$\omega = \frac{k_y N}{k_z} \tag{4.9}$$

The mode-1 vertical wavenumber is $k_z = \pi/H$ and the mode-1 component of $\mathcal{V}$ is $\cos(\pi z/H)$ multiplied by some coefficient. The along-channel wavelength then follows as

$$\lambda_y = \frac{2\pi}{k_y} = \frac{2NH}{\omega} \tag{4.10}$$

These waves are non-dispersive:

$$c_p = \frac{\omega}{k_y} = c_g = \frac{\partial \omega}{\partial k_y} = \frac{NH}{\pi} \tag{4.11}$$

4.4.2 Step-trapped Kelvin waves

An internal Kelvin wave can still exist if the vertical wall is replaced by a step change in depth. Following Durran (2000), we term this a step-trapped Kelvin wave. Below the step on the deeper side, the structures of the mode-1 pressure and density perturbations and the baroclinic velocities (Figures 4.5a–d) resemble the bottom half of a standard internal Kelvin wave. Key differences, however, are that there is no zero crossing in $\mathcal{P}$, the zero crossing in $\mathcal{V}$ now occurs near the step height, not mid-depth, and the solution is no longer separable in x and z. Wave solutions are now of the form

$$v' \propto \mathcal{V}(x,z) \exp\left(i(\omega t - k_y y)\right) \tag{4.12}$$

Mode shapes $\mathcal{P}$, $\mathcal{U}$, $\mathcal{V}$, and $\mathcal{W}$ must be calculated numerically as described by Chapman (1982) in detail in his Appendix B, in which he uses the term 'subinertial geophysical model' rather than step-trapped Kelvin wave. The equivalent problem for an atmospheric context, which differs only by the upper boundary condition, is addressed by Samelson (1999) and Durran (2000). We briefly outline the method below.

The problem is constructed by matching both the cross-step velocity and pressure perturbation above the step at $x = 0$ and requiring no normal flow

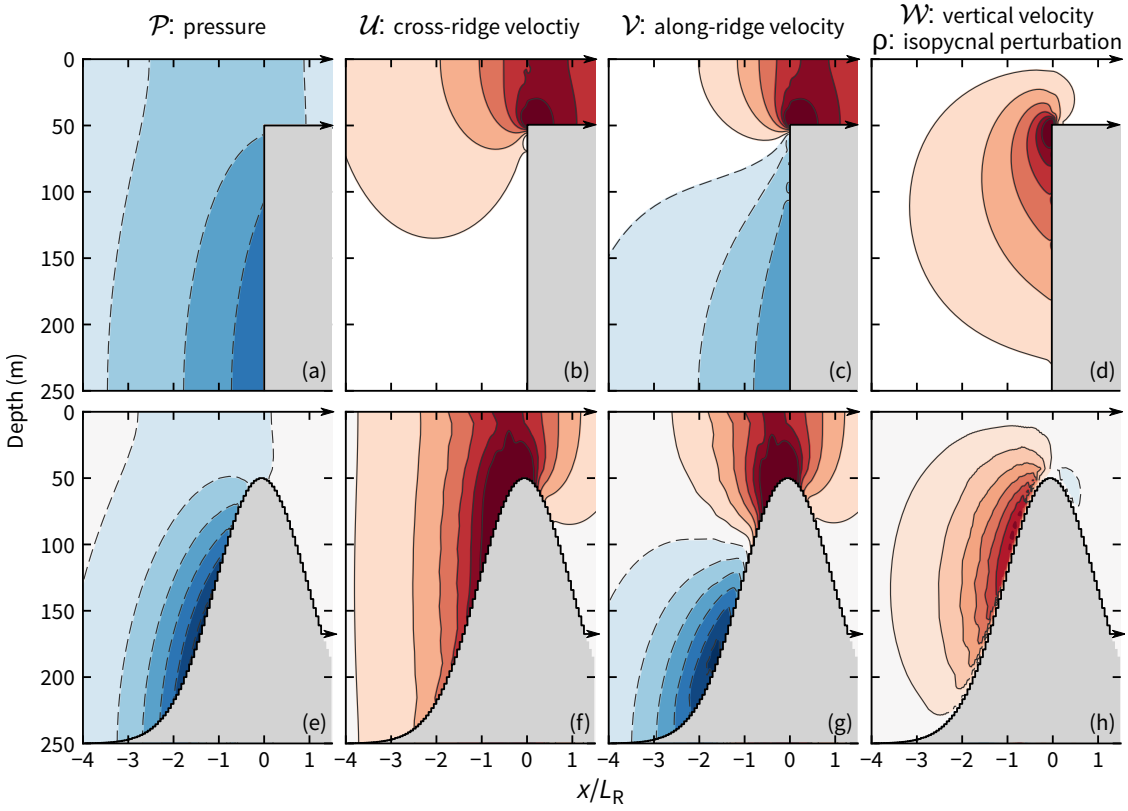

Figure 4.5 – Mode shapes for step- and ridge-trapped Kelvin waves travelling into the page. Hue indicates phase and saturation indicates magnitude. In both cases, a tidal frequency of $0.8f$ is used and the domains extend indefinitely each side of the obstacle. Note that although colour scales are somewhat arbitrary, $\mathcal{U}$ and $\mathcal{V}$ for a given obstacle use the same scale.

at $x = 0$ below the step. Taking the pressure and velocity to be the sum of a large number of Fourier modes, say $M = 20$, the problem becomes a generalized eigenvalue equation of the form

$$\mathsf{L}\mathbf{A} = \omega^* \mathsf{R}\mathbf{A} \tag{4.13}$$

where L and R are $M \times M$ matrices derived from the matching conditions, $\mathbf{A}$ is a vector of M Fourier coefficients, and the frequency ω^* (non-dimensionalized by f) is the eigenvalue.

For our purposes, two complications arise in the matrix problem. First, ω^* appears when constructing L and R. Second, the problem assumes k_y is known

and ω is unknown, which is the opposite to what is needed here. These two problems are overcome by solving the eigenvalue problem iteratively. First, the desired ω^* is set together with a broad estimate for k_y. Solving the eigenvalue problem produces an ω^*, k_y pair in which k_y is the estimate, but ω^* is now the eigenvalue not the set value. The process is repeated with an adjusted estimate of k_y based on linear or quadratic fits through ω^*, k_y pairs from past iterations. Fewer than 10 iterations will typically produce results accurate to four significant figures.

4.4.3 Ridge-trapped Kelvin waves

An internal wave trapped at an arbitrarily shaped ridge is similar in most respects to a step-trapped wave (Figure 4.5), with two important, related differences. Where a slope exists, fluid parcels may travel up and down leading to a nonzero cross-ridge velocity below the crest. The induced changes in vorticity lead to an additional restoring force and consequently a shorter along-ridge wave. In weak stratification these would be similar to topographic Rossby waves.

Solving for the mode shapes is not straightforward. Although the problem is analogous in many ways to coastal trapped waves, the literature for these waves often requires that the topography intersect the coast (e.g., Huthnance, 1975, 1978; Dale and Sherwin, 1996; Johnson and Rodney, 2011). Conversely, codes by Brink (2006) allow for an open boundary but cannot be used here because they produce spurious solutions when $\omega \approx f$. Dale et al. (2001) overcome this issue for the coastal problem by formulating it without a velocity boundary condition that is singular. This singularity does not arise in the method used to calculate the step-trapped wave (Section 4.4.2), which we therefore generalize in this section.

A smoothly sloped ridge is approximated by an arbitrary number of flat-bottomed regions. For each region, as for the step-trapped wave, the pressure and cross-ridge velocity perturbations are expressed as a sum of orthogonal vertical modes and are matched at each step. Kelly et al. (2013) use such a method for superinertial tides across, rather than along, topography. Ultimately, a block matrix equation arises that is conceptually similar to Equation 4.13. Again, this is solved iteratively to determine the Fourier coefficients and wavenumber. Details are provided in Appendix B. An example of the mode shapes for the Gaussian

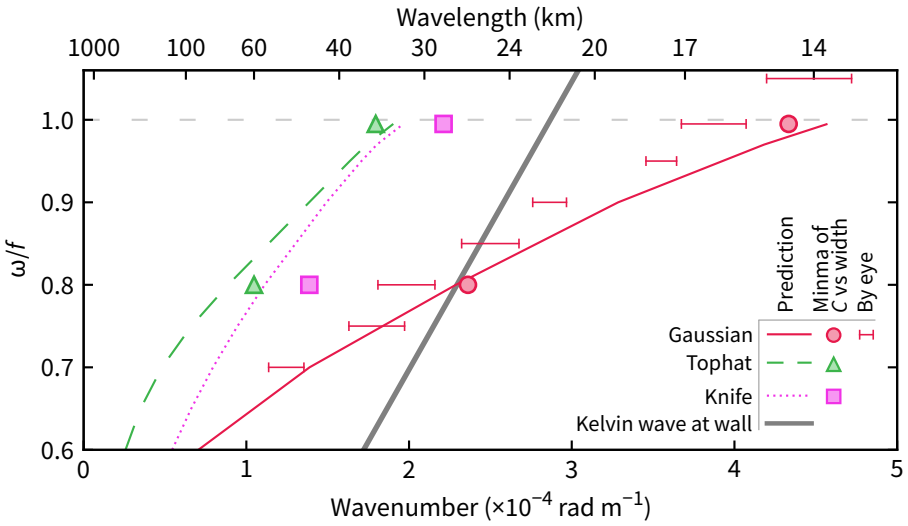

Figure 4.6 – Dispersion curves for the various along-obstacle waves. The curves predicted by the linear, mode-matching method are validated by the markers, which are derived from simulations.

topography are shown in Figures 4.5e–h. The apparently smooth obstacle is actually comprised of 150 flat-bottomed regions, each 200 m wide, corresponding to the resolution used in the simulations.

Knowing mode shapes elucidates the physics of the along-obstacle waves, but is ultimately a byproduct of our aim to predict the wavelength for a given obstacle as this controls how conversion varies with channel width (to be described in Section 4.5). The dispersion curves for all obstacles (Figure 4.6) demonstrate that the Gaussian obstacle induces waves typically half as long as the other obstacles owing to the topographic Rossby effect. Indeed, this effect is the only reason that the along-obstacle wave can be shorter than the internal Kelvin wave beside the wall (Section 4.4.1).

From our suite of simulations, there are two methods by which we can validate the predicted wavelength. The simpler method is to estimate the wavelength 'by eye' from model snapshots in a wide channel like those shown in Figures 4.7c and 4.7d. We used this method for eight frequencies for the Gaussian obstacle. (The largest frequency simulation, $1.05f$, confirms an expectation that ridge-trapped waves can exist at slightly superinertial frequencies and that there is a continuous transition across $\omega = f$ (see Dale et al., 2001).) The by eye estimates

follow the prediction well, albeit with a systematic difference that likely reflects the limitation of the estimate rather than the prediction. The second, more accurate wavelength estimate comes from the minima of a curve of conversion vs channel width. Figure 4.4a provides an example for the Gaussian obstacle at $\omega = 0.995f$. The wavelength in this case is $4.0\,L_\mathrm{R}$ (14 km).

In general, the predicted wavelengths agree well with those estimated from the simulations, even for $\omega \approx f$ cases. We are not clear, however, what causes the small discrepancies. For example, the predicted wavelength for the tophat obstacle forced at $0.8f$ is 70 km, whereas the simulations indicate it is 60 km. Possible explanations include bottom friction in the simulations or the nonlinear stratification that arises due to mixing over the ridge.

4.5 Conversion versus channel width

The efficiency of tidal conversion depends on the channel width scaled by the along-obstacle wavelength, a result alluded to in Figure 4.4. For each obstacle, curves of per unit width conversion for the two tidal frequencies approximately collapse when this width scaling is applied. This occurs despite changes of 50% or more in the along-obstacle wavelength between the two frequencies.

4.5.1 Examples of strongly and weakly responding channels

We first consider a qualitative comparison between strongly and weakly responding channels with a tophat obstacle (Figure 4.7). When the channel width is $1.5\lambda_y$, isopycnal perturbations within the Kelvin wave along the southern edge reach 20 m. Much the same picture also arises for a $0.5\lambda_y$-width channel. Conversely, when the channel width is $1.0\lambda_y$, the Kelvin wave is barely evident. The magnitudes of the waves travelling along the obstacle in the $1.5\lambda_y$ and $1.0\lambda_y$ cases are comparable as these waves have yet to interfere with those generated at the southern end of the channel.

Evidently, interference between the waves generated at the northern and southern ends of the obstacle determines whether the response is large or small. Regardless of channel width, the waves generated at each end should be out of phase because flow diverges at one end of the obstacle at the same time as flow

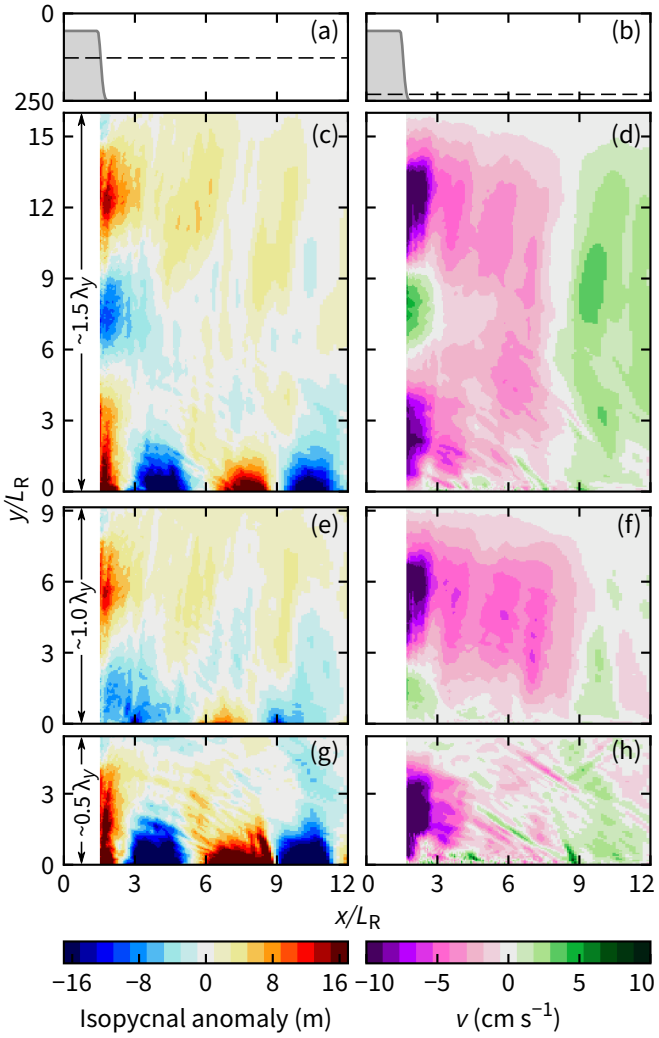

Figure 4.7 – Snapshots of the differing responses in three channels with large, small, and large tidally averaged conversion, respectively. Fields are taken from the eastern half of the tophat simulations after six tidal cycles at the depths shown in panels a and b. $U_0 = 4\,\mathrm{cm\,s^{-1}}$ and $\omega = 0.995f$.

converges at the other, and vice versa a half period later. Assume that, at a specific time, the wave generated at the northeast end of the obstacle is associated with depressed isopycnals (as in Figure 4.7). At this same time, the wave generated at the southeast end will be associated with elevated isopycnals. Because the wave travels $1\lambda_y$ in one tidal period ($c_p = \lambda_y/T$), the waves in the $1\lambda_y$-wide channel, will meet perfectly out of phase. The same would be true for any integer multiple of λ_y. Conversely, for half integer multiples, the extra half period that it takes for the waves to meet leads to constructive interference.

4.5.2 Channel width controls interference and conversion

Tidally averaged conversion provides a single-valued quantity for each simulation that reflects the size of the response and allows easy comparison between all channel widths for a given obstacle and frequency. Specifically, we use the tidally averaged conversion integrated over the 40 km-long energy control volume shown in Figure 4.1a. (Alternatively, we could have used the baroclinic flux divergence to reach the same conclusions.) When expressed per unit width, this quantity can be compared with the two-dimensional, non-rotating limit for very narrow channels.

Curves of conversion against channel width scaled by λ_y (Figure 4.8) demonstrate that interference between the along-obstacle wave and the outgoing Kelvin wave is the dominant physical process controlling the size of the response. Indeed, simple mathematical expressions provide adequate first-order explanations for the observed curve shapes.

Assume isopycnal perturbations in both waves are described by sinusoids. For example, let the Kelvin wave along the wall, which we will refer to as y_1, be described by

$$y_1 = \sin\left(2\pi\omega t\right) \tag{4.14}$$

The ridge-trapped Kelvin wave, y_2, is therefore

$$y_2 = -\sin\left(2\pi\omega t - 2\pi w/\lambda_y\right) \tag{4.15}$$

The phase difference is simply the channel width w relative to the along-channel wavelength, as alluded to earlier, together with a minus sign out front to recognize

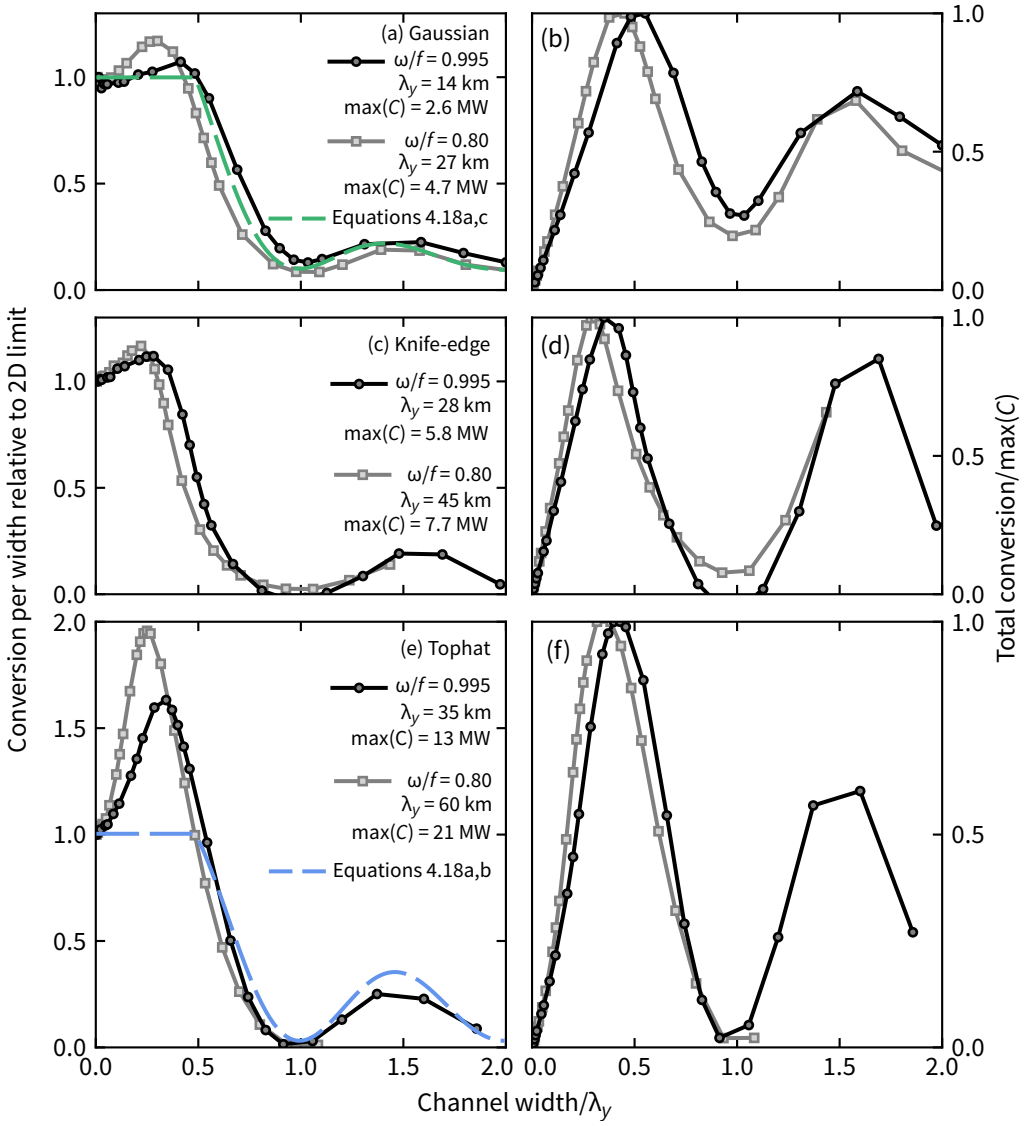

Figure 4.8 – Near-collapse of conversion curves when channel width is non-dimensionalized by the along-obstacle wavelength. For a given obstacle and forcing frequency, max(C) refers to the maximum volume-integrated, tidally averaged conversion rate among all channel widths shown.

that y_2 is generated out of phase with y_1. For a Gaussian obstacle, the wave decays significantly as it travels along the ridge thereby reducing the interference. Empirically, we observe that the wave decays exponentially with a length scale comparable to λ_y. Let y_3 describe this decaying wave:

$$y_3 = -\sin\left(2\pi\omega t - 2\pi w/\lambda_y\right)\exp\left(-w/\lambda_y\right) \tag{4.16}$$

For a non-decaying wave, the tidally averaged flux per unit width will be proportional to

$$\frac{1}{wT}\int_0^T (y_1 + y_2)^2\,\mathrm{d}t \tag{4.17}$$

and similarly for a decaying wave with y_2 replaced by y_3.

For channels less than $0.5\lambda_y$, other factors that are described in Section 4.5.3 come into play. Furthermore, interference is not easily defined as there are not two clearly distinct waves. In this range, we set per unit width conversion to the two-dimensional, non-rotating limit $C_{2\mathrm{D}}$. Ultimately, the expressions for per unit width conversion are

$$\frac{C}{wC_{2\mathrm{D}}} = 1 \qquad w < 0.5\lambda_y \tag{4.18a}$$

$$= \frac{1}{w/\lambda_y}\frac{0.249}{T}\int_0^T (y_1 + y_2)^2\,\mathrm{d}t \qquad \text{tophat, } w > 0.5\lambda_y \tag{4.18b}$$

$$= \frac{1}{w/\lambda_y}\frac{0.386}{T}\int_0^T (y_1 + y_3)^2\,\mathrm{d}t \qquad \text{Gaussian, } w > 0.5\lambda_y \tag{4.18c}$$

where the numerical constants in front of the integrand ensure that the expressions are continuous at $0.5\lambda_y$. Considering their simplicity, these curves agree well with the values derived from the simulations. Notably absent, however, is a prediction for the knife-edge obstacle. In this case, we cannot ignore interference above the crest between the waves on opposite sides of the obstacle and, consequently, a simple fit is no longer possible.

A limitation of our simple fits is they assume conversion is governed only by interference of the two trapped waves. Although this is typically true, counterexamples are channels wider than $10L_{\mathrm{R}}$ with a Gaussian obstacle (Figure 4.4). In these cases, the along-ridge wave decays significantly before it reaches the other side of the channel. Consequently, tidal conversion due to dissipation in

the evanescent wave near the ridge must be considered.

4.5.3 Enhanced conversion in narrow channels

In narrow channels ($\lesssim 0.5\lambda_y$), especially for the tophat obstacle, per unit width conversion may be larger than the two-dimensional, non-rotating limit. This is perhaps counter-intuitive as seldom does the influence of rotation increase tidal conversion (as noted in Section 4.1, conversion in a two-dimensional scenario drops as $\sqrt{1 - f^2/\omega^2}$ and is zero if $\omega < f$). The increase occurs, in part, because of how the barotropic tide propagates in the channel. As the barotropic tidal current impinges on a obstacle, the consequent convergence raises the upstream sea level. This induces a surface pressure gradient which, under Coriolis, leads to convergence and increased sea level at the right-hand wall of the channel near the obstacle and vice versa at the left-hand wall. Half of a tidal period later, the equivalent process occurs at the opposite end of the obstacles.

In all but the narrowest channels, the convergence of barotropic flow owing to rotation is appreciable. As noted in Section 4.2.2, the vertical velocity W is a measure of this convergence. This additional convergence ultimately increases the conversion term C near the wall (Equation 4.3). This is evident in maps of tidally averaged conversion in narrow channels. An example is given in Figure 4.9 for the Gaussian obstacle with a tidal frequency of $0.8f$. Accompanying these maps are the tidally averaged sea surface heights, which are negative everywhere because energy is being extracted from the barotropic tide.

As we will show in the following sections, conversion is the dominant process by which energy is extracted from the barotropic tide. Furthermore, determining whether conversion is comparatively large or small is a pre-requisite for an understanding of the full energy budget for a given channel. In a weakly responding channel, for example, near-obstacle turbulent dissipation will play a larger relative role.

4.6 Barotropic and baroclinic energy budgets

For superinertial latitudes in the weak forcing limit, loss of barotropic tidal energy over an obstacle is typically dominated by the generation of internal

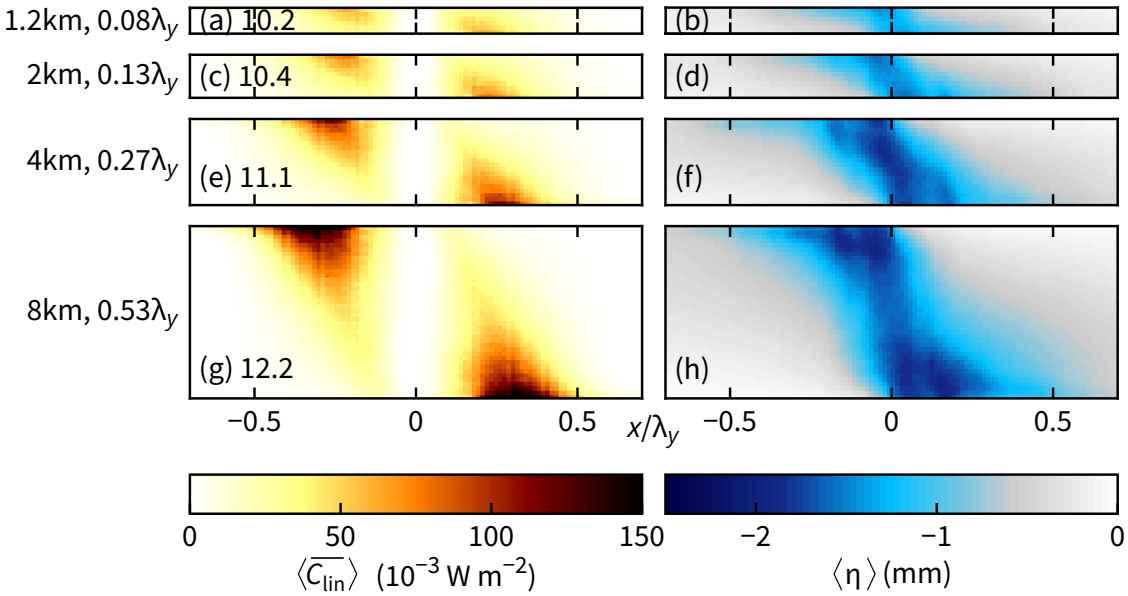

Figure 4.9 – Tidally averaged conversion and sea surface height in narrow channels. Within the range of channels shown, the spatial average of $\langle \overline{C} \rangle$ over the energy control volume (the values given beside the panel labels) increases with channel width. All simulations have a Gaussian obstacle and tidal frequency of $0.8f$.

tides. As forcing is increased, other mechanisms come into play: high-frequency internal wave generation, bottom boundary layer dissipation, and near-ridge dissipation. In this section, we demonstrate that these same principles apply to subinertial internal tide generation in a channel. A channel, therefore, provides an obvious contrast to the subinertial infinite ridge in the weak-forcing limit in which barotropic energy loss is small as tidally averaged conversion occurs only via turbulent dissipation.

4.6.1 Energetics with varying channel width

To investigate how energy terms vary with channel width (Figure 4.10), we use the Gaussian setup with the deep-water tidal current amplitudes fixed at $U_0 = 4\,\mathrm{cm\,s^{-1}}$ (see Table 4.1). The conversion curves, and consequently the flux divergence curves, are predominantly explained by the interference described in Section 4.5. Here we further consider curves for the dissipative terms D_0, D', and ε.

The barotropic component of bottom boundary layer dissipation, D_0, shows the least variation with channel width of all six terms. Consequently, it plays a proportionately larger role in wider channels (Figure 4.10c). Arguably, D_0 should show no variation with channel width given that it arises predominantly from barotropic flow normal to the obstacle. Some variation occurs, however, and is somewhat correlated with the total variance in the velocity fields.

The dissipative terms in the baroclinic energy budget, D' and ε, both display a trend that broadly corresponds to the conversion curve. For example, larger conversion equates to more variance in the baroclinic fields and consequently larger dissipation. The importance of these terms to the baroclinic energy budget (Figure 4.10d) is largest when the channel width is an integer multiple of λ_y, but only because this is when the barotropic energy loss is at a minimum.

For many channel widths, up to 20% of both the barotropic and baroclinic energy budgets is not explicitly accounted for because of three factors. First, we assume the system is in a perfect tidally steady state. However, rates of change of barotropic and baroclinic energy densities over the tidal cycle account for as much as 3–4% of each budget. Second, both $\nabla \cdot \mathbf{F}_0$ and $\overline{C}$ have large oscillations relative to their tidal averages, thereby amplifying any numerical issues related to resolution or discretization. In the wider channels, for example, peak-to-peak amplitudes of these quantities are order 50 times larger than their means. This effect is reduced in narrower channels, hence the better closure of the barotropic budget. Third, we include only explicit dissipation; numerical dissipation is not quantified.

4.6.2 Energetics with varying tidal forcing

When tidal forcing is varied with channel width held fixed, the energetics are largely governed by power laws (Figure 4.11). In this section, we fix channel width (26 km, $1.8\lambda_y$) and forcing frequency ($\omega = 0.995f$) and vary the deep-water tidal current amplitudes over the range $U_0 = 1$–$24\,\mathrm{cm\,s^{-1}}$. For the barotropic energy budget, we empirically find that

$$\left\langle \overline{C} \right\rangle \propto U_0^{2.07\pm0.02} \tag{4.19}$$

$$\langle D_0 \rangle \propto U_0^{2.60\pm0.01} \tag{4.20}$$

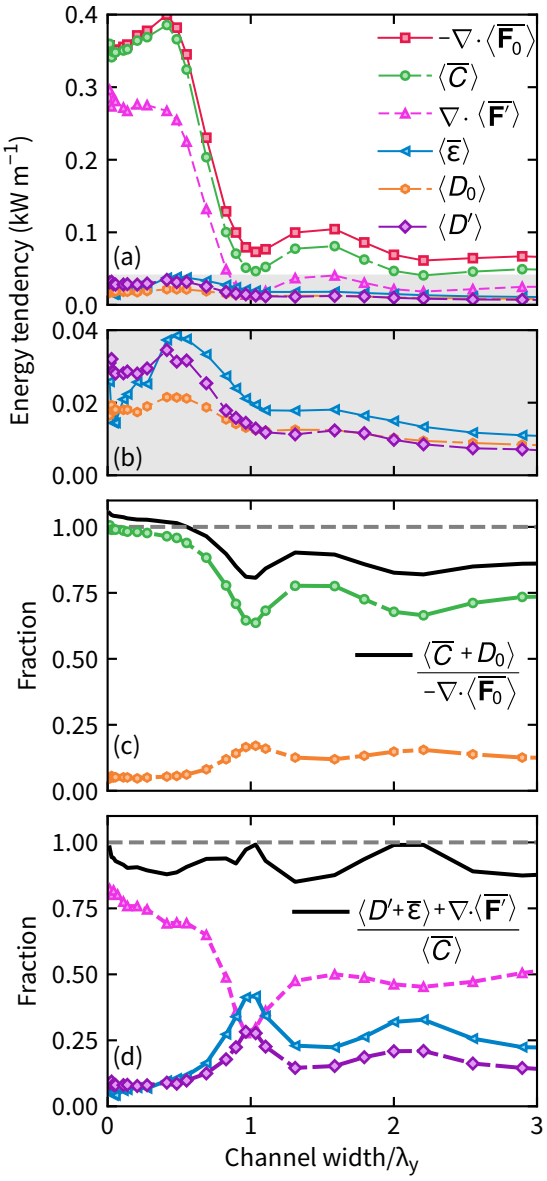

Figure 4.10 – The relevance of different energy terms for varying channel widths. Simulations all include a Gaussian obstacle and a tidal forcing of $U_0 = 4\,\mathrm{cm\,s^{-1}}$ at $\omega = 0.995f$. (a) Each component of the budget per unit width. (b) Zoomed variant of panel a to show the three small terms. (c and d) The barotropic and baroclinic energy budgets, respectively. The black lines indicate the degree to which the terms shown close the individual budgets.

The power law for $\langle \overline{C} \rangle$ is consistent with the two-dimensional, superinertial prediction for knife-edge topography of U_0^2 (Llewellyn Smith and Young, 2003). Despite the smaller exponent for C compared to D_0, conversion is the dominant term in the barotropic energy budget across the forcing range we consider.

The exponent for the D_0 power law is not 3 as may be expected from the simple argument that it should arise from a drag force, $\propto U_0^2$, multiplied by the velocity (e.g., Taylor, 1919). This argument does hold, however, when we account for the difference between the deep-water tidal current and the bottom velocity over the sill, where D_0 is concentrated. The effect of stratification is to inhibit near-bottom flow because vertical advection results in a transfer of kinetic to potential energy. Gemmrich and Klymak (2015), for example, find a power law relationship between the barotropic forcing velocity and the bottom boundary layer velocity of $U_0 \propto u_{\mathrm{bbl}}^{0.87}$. (Their paper uses y, not x, as the cross-topography coordinate; we have adjusted their notation accordingly.) Applying their value in our case produces

$$\langle D_0 \rangle \propto u_{\mathrm{bbl}}^3 \propto \left(U_0^{0.87} \right)^3 = U_0^{2.6} \tag{4.21}$$

The baroclinic energy budget under varying forcing, rather than displaying a power-law nature, is better explained in terms of saturation: the baroclinic flux divergence and the baroclinic bottom boundary layer dissipation both taper off with increasing tidal forcing. Stronger forcing will produce larger baroclinic motions, but these cannot increase indefinitely. In the strongest forcing case ($U_0 = 24\,\mathrm{cm\,s^{-1}}$) isopycnal displacements near the wall can reach 150 m. The internal Kelvin waves that leave the energy control volume, however, are associated with displacements closer to 50 m. For this simulation, much of the potential energy generated is lost either over the ridge or within the first wavelength of the Kelvin wave.

Energy loss over the ridge to turbulent dissipation is the most difficult parameter to explain. Vertical along-channel slices (not shown) demonstrate that it predominantly occurs in breaking lee waves. Empirically, it obeys the following power law:

$$\langle \overline{\varepsilon} \rangle \propto U_0^{2.59 \pm 0.05} \tag{4.22}$$

The similarity to the D_0 power law is likely not a coincidence. For superinertial tides over a sufficiently steep ridge, Klymak et al. (2010a) would predict an

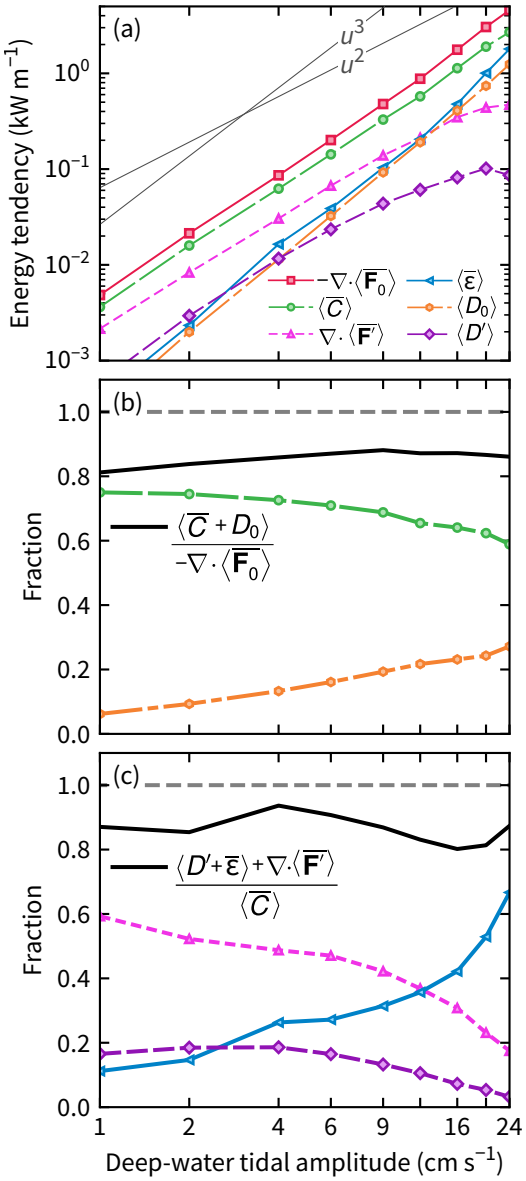

Figure 4.11 – The relevance of different energy terms for varying tidal forcing. Simulations all include a Gaussian obstacle in a channel of width $1.8\lambda_y$. (a) Each component of the budget per unit width. Note the log-log axis, which highlights the power-law scalings. (b and c) The barotropic and baroclinic energy budgets, respectively. The black lines indicate the degree to which the terms shown close the individual budgets.

exponent of 3. As we will describe, we expect a similar result for subinertial tides. As for D_0, the difference between the expected exponent of 3 and the actual exponent of 2.6 may result from a power law scaling of the barotropic velocity and the relevant velocity scale, which in this case is the velocity at the crest.

Klymak et al.'s (2010a) parameterization assumes local dissipation of all energy contained in internal modes that travel slower than the tidal advection speed above the crest. The energy contained in these slower, higher modes is determined from a knife-edge model (Llewellyn Smith and Young, 2003). This linear model, however, predicts zero energy for any mode when poleward of the critical latitude. Therefore we cannot quantitatively apply the parameterization. Nevertheless, their argument for a cubic power law remains valid. Briefly, the power law arises because the energy input into all modes slower than the critical mode n_c scales as U_0^2/n_c and n_c is inversely proportional to U_0. As shown by Musgrave et al. (2016b, see their Equations 2.31 and 2.32), the energy fed into different modes behaves the same for subinertial and superinertial tides and is proportional to U_0^2 in both cases. There is not an obvious way to extend the concept of a critical mode to subinertial modes and thereby introduce an extra factor of U_0. We therefore, instead, appeal to the simple argument that dissipation will be proportional to the rate of energy supply, which is the product of the energy density and velocity (e.g., Tennekes and Lumley, 1972, p. 20)

4.7 Discussion

4.7.1 Practical application of the idealized system

For superinertial latitudes, there are many methods for estimating the fate of energy lost from barotropic tides. Consider, for example, the energy dissipated locally. The methods range from simple rules of thumb, such as the suggestion that the local dissipation efficiency q is 0.3 (St. Laurent et al., 2002), to sophisticated recipes dependent on factors such as forcing, spectral characteristics of topography, and wave–wave interactions (Polzin, 2009; Klymak et al., 2010a). In this section, we reexamine our simulations to devise some general rules governing subinertial tide generation in channels that can be applied in practice.

The first step is to establish the along-ridge wavelength. In this study we

provide a method and code for an arbitrarily shaped ridge with constant or vertically variable stratification. Presuming that the wavelength has been found, we now appeal to the two-dimensional, superinertial literature. In Section 4.6.2, we empirically found that the conversion scales with U_0^2, just as linear, two-dimensional theory suggests. This potentially implies that a first-order estimate of tidal conversion in a subinertial channel can be made using the analytical theory (or a two-dimensional simulation) with $f = 0$, and then multiplying the appropriate fraction depending on the channel width relative to λ_y (see Figure 4.8).

A typical Arctic fjord, as noted by Cottier et al. (2010), is 10 km wide. Assume such a fjord features a steep sill comparable to our 'knife-edge' ridge and has the same stratification we used in the simulations. Hence, we turn to Figure 4.8c. If $\omega/f = 0.995$, then $\lambda_y = 28$ km and the fjord width is $0.35\lambda_y$. Reading off the curve indicates that conversion is 1.1 times the two-dimensional limit. Consequently, although the fjord may be 2–3 times the internal Rossby radius, it behaves as if it were non-rotating with respect to energetics.

For some channels widths, especially $\sim 0.5\lambda_y$, the conversion relative to the two-dimensional limit will depend sensitively on the exact obstacle and accuracy to which λ_y is known. In such cases, a more practical goal may be to calculate upper and lower bounds for the expected conversion. Further, we note that we have not proven that a simple fractional scaling of the two-dimensional limit is always applicable. Confirming such a result would require many more simulations with different combinations of obstacles, tidal frequencies, and tidal forcings.

We now turn to diagnosing or predicting local dissipation fraction q, an often-sought quantity closely related to diapycnal diffusivity. In our argument to follow, we will ignore bottom boundary layer dissipation terms and thereby equate q with ε/C. For subinertial latitudes in general, q is close to 1 unless a boundary is present to act as a waveguide.

Despite covering only a small part of the total parameter space (channel width, tidal forcing, obstacle shape, among others), our simulations produced values of q encompassing much of the 0 to 1 range. Nevertheless, q follows three general rules. First, it is smallest in the narrowest channels. Second, it peaks when channel widths are integer multiples of λ_y. Third, it approaches 1 as

forcing is increased to a level where the internal tides generated have isopycnal displacements comparable to the water depth. Such large displacements could also occur in two dimensions, but they are particularly prevalent here because rotation effectively shifts much of the potential energy toward the channel wall after its generation.

4.7.2 The importance of three-dimensional processes

The physics of tidal conversion poleward of the critical latitude changes significantly when a third dimension is introduced. In particular, convergence and divergence in the along-obstacle direction, a linear process, can generate nonzero tidally averaged conversion. In this study, channel walls induce the convergence and divergence, but any irregularities along the obstacle with a size comparable to the internal Rossby radius could do the same. Studies using only two-dimensional approaches may recognize this possibility, but nevertheless often appeal to a range of other explanations for nonzero conversion such as (i) the possibility that the critical latitude can shift poleward on the order of 100 km due to shear or non-traditional Coriolis effects (e.g., Lerczak et al., 2001; Gerkema and Shrira, 2005); (ii) the empirical result that trapped energy decays with a scale of 3 days, thereby leading to an energy flux (Falahat and Nycander, 2015); or (iii) that advection can generate high-frequency, freely propagating internal waves (e.g., Nakamura et al., 2000; Vlasenko et al., 2003; Rippeth et al., 2017).

Propagating, high-frequency waves are evident in our more strongly forced simulations. Energetically, however, they are a second-order effect relative to the Kelvin waves or near-ridge dissipation. As an example, we analyze a simulation where flow is supercritical over the ridge ($U_0 = 16\,\mathrm{cm\,s^{-1}}$) in terms of low- and high-frequency components of u' and p' (Figure 4.12). Specifically, we record u' and p' at 5 minute intervals at a cross-channel slice 14 km from the crest of the obstacle and then low- and high-pass filter each using Butterworth filters with cutoff frequencies corresponding to half a tidal period (6.2 hours). The low frequency component of the signal ($\overline{u'_{\mathrm{low}}\, p'_{\mathrm{low}}}$) captures 79% of the total, whereas the high-frequency component captures only 12% (cross terms account for the remainder). We recognize that this single example is far from proof that high-frequency waves are of minor importance here, especially when using a

hydrostatic model with 200 m resolution. However, this result is consistent with several others.

Using a two-dimensional, subinertial model, Musgrave et al. (2016b) note that harmonics of a subinertial internal tide can propagate away but their energy content is small. Observationally, de Young and Pond (1989) found that high-frequency internal waves explain only 2% of the energy lost in a British Columbia fjord. (This example includes both superinertial M_2 tides and subinertial K_1 tides). Finally, when simulating internal waves around a mid-latitude island, Masunaga et al. (2017) found that the subinertial diurnal internal tidal energy flux trapped around the island had an intensity roughly 100 times larger than that due to high-frequency waves.

When internal tides are trapped around an island, or similarly a plateau or seamount (e.g., Brink, 1989), the majority of the energy will dissipate locally. In that respect, such three-dimensional systems are similar to a two-dimensional ridge. However, in the two-dimensional case, dissipation within the evanescent wave controls how much energy is extracted from the barotropic tide. Conversely, in the three-dimensional case, the amount of energy converted to a trapped-but-propagating internal tide is the controlling factor. We expect that more energy would be extracted for the three-dimensional case, especially when resonance occurs. For example, strong barotropic energy loss from the K_1 tide in the Kuril Straits is linked to the generation of coastal-trapped waves (Tanaka et al., 2010). Similarly, Fer et al. (2015) describe the conversion at Yermak Plateau (81°N) as substantial and demonstrate that the strongest conversion and dissipation occur at the steep sides of the plateau.

Considering the behaviour of waves trapped at steps and ridges (Section 4.4), we note that the decay of internal tides is a plausible explanation for the observed correlation between bathymetric slope and turbulent dissipation in the Arctic (Rainville and Winsor, 2008; Rippeth et al., 2015; Meyer et al., 2017). (See also Fer et al. (2016) for a similar result for the Antarctic.) This correlation may exist because steeper topography is a better waveguide for subinertial internal tides. Indeed, Musgrave et al. (2017) argue that this explains the large dissipation of diurnal internal tides at the Mendocino Ridge. Furthermore, this explanation, rather than a lee wave explanation, is consistent with the finding that turbulent mixing occurs even for relatively modest tidal currents (Rippeth et al., 2015).

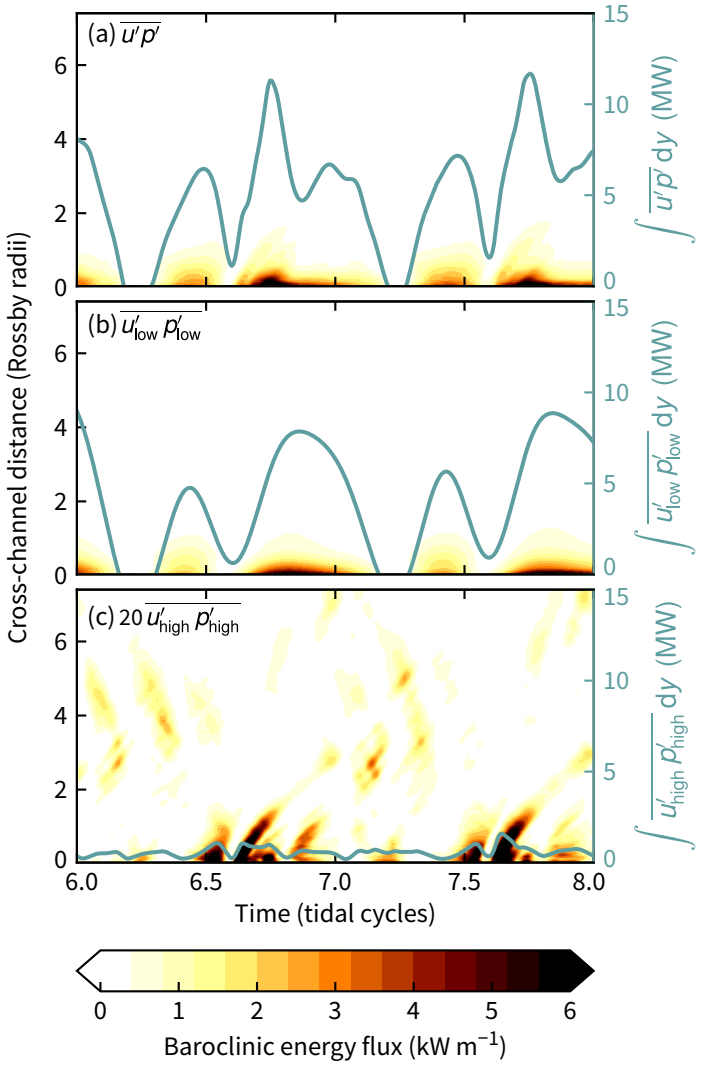

Figure 4.12 – Contribution of low- and high-frequency internal waves to the total baroclinic flux over two tidal cycles. The values shown are taken from a cross-channel slice 14 km east of the crest of the Gaussian obstacle, and the deep-water tidal forcing was 16 cm s^{-1}. Low- and high-frequency motions are separated at a frequency corresponding to a half tidal period. Note the factor of 20 in panel c without which the signal is imperceptible. The width-integral (right-hand axis), however, is not adjusted.

4.8 Conclusion

We have used a suite of numerical simulations to demonstrate a simple mechanism that produces tidal conversion poleward of the critical latitude without any appeal to nonlinear behaviour. Although we have focused on a channel, the simple requirement that the obstacle has either irregularities or a finite length means that subinertial tidal conversion can occur for other features such as plateaus and finite-length ridges. Idealized, three-dimensional modeling of such features in a tidal flow will likely prove fruitful and may elucidate the processes behind the strong subinertial conversion that has been identified in realistic simulations in locations such as Kuril Straits, Izu-Oshima Island, and Yermak Plateau. The role of the ratio of along-obstacle wave to obstacle size in other geometries without channel walls will be an interesting question.

The interference between the waves generated at each end of the obstacle in a channel modulates the energy extracted from the barotropic tide. The length scale over which this occurs, the wavelength of the along-ridge wave, is notably longer than the internal Rossby radius. At least with respect to energetics, channel width is better measured against this wavelength rather than the internal Rossby radius. Indeed, we reiterate the possibly counterintuitive finding that tidal conversion can be larger than suggested by an equivalent non-rotating, two-dimensional case even for channels up to approximately five internal Rossby radii wide.

Finally, we highlight a potentially misleading inference that can arise from studies that describe superinertial internal tides as freely propagating and subinertial tides as trapped. Yes, subinertial internal tides are trapped, but that should not imply that they cannot propagate. As long as they have a boundary to propagate beside, they are free to redistribute energy within the ocean, even if it is only a local redistribution.

Acknowledgments

This research was enabled in part by support provided by WestGrid (`westgrid.ca`) and Compute Canada (`computecanada.ca`). Ann Gargett provided a number of helpful suggestions on this paper. Input for model simulations and output in a reduced form are available from `kghughes.com/data`.

Chapter 5

Conclusion

Mass and energy budgets and theories of hydraulic control and internal tide generation have have been invoked in this thesis to improve the physical understanding of flow dynamics in the Archipelago, with particular attention paid to the central sills area. These budgets and theories have been applied to a large-scale, three-dimensional model; a new high-spatial-resolution, observational dataset; and two- and three-dimensional, process-oriented models of stratified flow over idealized obstacles.

When beginning this work, little was known about the relative importance of smaller-scale processes. It is easy to postulate numerous processes that could be occurring in the many channels. Quantifying these processes, however, and thereby identifying where future modelling and observational efforts should be focused, is difficult and underpins this thesis. My smaller-scale, bottom-up approach is notably different to many recent studies that use large-scale models to investigate large-scale controls (such as sea level pressure differences or wind patterns) on fluxes, particularly freshwater fluxes, through the Archipelago. Indeed, I used such a model in Chapter 2, but examined the fluxes only as a means of explaining, in part, the simulated mixing rates.

In no way am I dismissing the necessity and importance of large-scale modelling for understanding the Archipelago. Instead, my work is complementary. This is exemplified in Chapter 2 where one aim was to identify deficiencies within the model so that it could be improved. A second aim was to simply ask what the model can teach us about the spatial and temporal variability of mixing.

Vertical buoyancy fluxes simulated by the large-scale model indicated the disproportionate importance of constrictions (channels, sills, or both). This proved to be beneficial and a recurring theme throughout the thesis. The Archipelago is a large region and surveying it all in detail would be a monumental task. The modelling demonstrated that much of the region is comparatively quiescent and, at least in terms of cumulative water mass modification, can be safely ignored.

Effort can instead be focused at a small number of hotspots. One of these hotspots was the central sills area where the observational study was undertaken. This is not surprising as the region was chosen based on several inferences of strong modification. Simply looking at a bathymetric chart or even just considering its name would suggest that the central sills area is a hotspot.

The large-scale modelling was useful in providing some baseline mixing estimates together with hints at explanations for a seasonal cycle. As well as the topographic effects, enhanced mixing was correlated with volume flux, a lack of ice cover, and the strength of toward-Arctic flow. These correlations, however, are only a starting point to an adequate description of mixing in the Archipelago. Moreover, these correlations arise in a tideless model.

Tides and mean flows through the Archipelago should not be treated independently (yet often are) because of their comparable magnitudes. This leads to strong coupling for any process that scales nonlinearly with current magnitude, a point stressed in Section 3.5.2. The coupling between mean and tidal flows was a necessary part of the explanation of the internal hydraulics downstream of Maury Channel. More importantly, however, was the role of coupling in the energetics.

The coupling, together with time constraints, resulted in large uncertainties for the observational energy budget for the central sills area. (Reducing these uncertainties was part of the initial motivation for Chapter 4.) Nevertheless, the observational study was effective and efficient. Despite the time constraint, we were able to (i) estimate both the mean and tidal currents through Maury Channel, (ii) cumulatively capture all phases of the internal hydraulic flow through Maury Channel, (iii) observe internal tides radiating southward along Cornwallis Island, and (iv) observationally constrain the potential energy lost over the sill. These somewhat independent measurements were tied together by extrapolating and invoking secondary sources such as WebTide. Consequently, a first-order picture of the energetics emerged.

Mixing, or at least turbulent dissipation, was poorly quantified by our observations. Given the inadequate vertical resolution of the moving vessel profiler, dissipation was estimated using only the 24 casts from the rosette-mounted CTD profiler. Taking microstructure profiles is the obvious solution, but this would not be my first suggestion if a follow-up survey were undertaken. I would

expect this would merely further confirm the conjecture that enhanced dissipation occurs within constrictions, near channel walls, and near steep topography. Many studies already demonstrate a correlation between dissipation and topographic steepness in the Arctic but do not describe a compelling causation (see Section 4.7.2). Instead of microstructure profiles, I would advocate for more focus on the initiation of the energy cascade to its smallest scales. Specifically, I would encourage cross-channel transects within and around the constrictions and a more thorough analysis of internal tide generation.

The generation of internal tides as Kelvin waves was identified as a large sink of barotropic tidal energy in the central sills area. It is second only to bottom boundary layer dissipation which, as argued in Section 3.5.2, is easily estimated as $C_\mathrm{d}U^3$. Conversely, the energy fed into Kelvin waves and its dependence on topography and forcing is not easily estimated.

The study described in Chapter 4 began as an attempt to investigate the internal Kelvin wave beside Cornwallis Island (see Figures 3.5 and 3.12). Specifically, could its energy flux (60 MW) be related to the width, depth, and currents of Maury Channel? If so, this would place the observations in context, rather than being a single realisation of a large parameter space. The question, as we now know, is straightforward to pose, but has a complicated answer. This is especially true in the central sills area as the following example demonstrates.

Maury Channel is 13 km wide. This is half of 26 km, which is the estimate of the along-obstacle wavelength made using the true bathymetry applied to the method described in Section 4.4.3. As indicated in Figure 4.8 when channel with is $0.5\lambda_y$, the efficiency of internal tide generation relative to the two-dimensional, non-rotating limit depends sensitively on obstacle shape. Furthermore, internal tides will also be generated after flow exits the two similarly sized channels north of Maury Channel. These internal tides can then propagate southward and interfere with the internal tide from Maury Channel. Whether these interferences are constructive, destructive, or somewhere in between is likely sensitive to the exact bathymetry.

Given their complexity, accurately evaluating internal tide generation in these three channels, and others like Penny Strait and McDougall Sound, will ultimately require high-resolution, realistic modelling. At one stage, an aim for this thesis was to simulate three-dimensional tidal dynamics in the central sills

area at 200 m horizontal resolution. This was not pursued, however, in favour of the idealized modelling, the results of which are a prerequisite to interpreting any modelling in a realistic setting. In other words, for the central sills area, the value of the idealized modelling lies in elucidating the physical process: the idea that constrictions induce convergence and divergence, which leads to trapped waves propagating parallel to topography. A key message from the conclusion to Chapter 4 is that this three-dimensional process is often implicitly precluded through the use of two-dimensional models.

The internal tide mechanism described in Chapter 4 may not hold for shorter or less steep obstacles. In these cases, the along-obstacle wave may not efficiently transmit an internal wave from one side of the channel to the other. Consequently, it is unclear whether internal wave interference will play a role in tidal conversion in such cases. The role of model resolution is another unaddressed factor. A worthwhile exercise would be to systematically investigate how well tidal conversion is captured as model resolution changes from, say, 200 m to 4 km, the latter value being representative of contemporary large-scale models.

Looking to the future, I am interested to see how large-scale modelling results change if and when tides are included. The results throughout this thesis continually demonstrate that tides are a primary source of energy and admit several energy pathways that otherwise would not occur. Ultimately, the processed described in this thesis provide phenomenologies, and often quantitative measures, against which large-scale models can be evaluated.

Appendix A

Barotropic tidal energy fluxes

The total convergence of the barotropic tidal flux, equivalently the barotropic tidal dissipation, is stated in Section 3.5 to be 590 MW for the channels surrounding Cornwallis Island. This value is found by summing the tidally averaged values for each of the five tidal constituents in the WebTide model following the methodologies of Kowalik and Proshutinsky (1993) and Chen et al. (2009). For each tidal constituent, the velocity components and sea surface height are assumed to vary sinusoidally. The tidally averaged fluxes integrated over depth D in the east–west and north south directions simplify to

$$E_x = \frac{1}{2} g \rho \eta_0 u_0 D \cos(\phi_u - \phi_\eta) \tag{A.1}$$

$$E_y = \frac{1}{2} g \rho \eta_0 v_0 D \cos(\phi_v - \phi_\eta) \tag{A.2}$$

where η_0, u_0, and v_0 are the amplitudes of the sinusoids and the ϕ terms are their associated phases. A kinetic energy term does not appear as it averages to zero over a tidal period.

A standing wave in which velocity and surface height are 90° out of phase has a tidally averaged flux of zero. A progressive wave with zero phase difference has the maximum possible flux. The latter is approximately the case in Wellington Channel (Section 3.3.2) in which northward velocity and sea surface height are only 15° out of phase.

The tidal energy flux convergence is subject to potentially large uncertainty as it assumes that the barotropic flow is reasonably estimated. Modelled tidal elevations and phases near Cornwallis Island typically agree with tide gauges to within 5–15 cm (10–30%) and 10–15°, respectively, for the largest constituents. There is poorer agreement between modelled and predicted velocities, but this comparison is based on sparse ADCP mooring data. For complete details, see Sections 5 and B.5 of Collins et al. (2011).

Appendix B

Ridge-trapped Kelvin wave derivation

The step-trapped Kelvin wave described in Section 4.4.2 can be generalized from a single step to an arbitrary obstacle shape with or without a coastal boundary in a conceptually straightforward, albeit algebraically tedious, manner. Specifically, we assume the obstacle is composed of an arbitrary number of discontinuities $j = 1, ..., J$ separating locally flat regions (Figure B.1). Matching conditions for the pressure P and velocity U perturbations are solved simultaneously at all discontinuities. Python code implementing this calculation is available at `github.com/hugke729/RidgeTrappedWave`. Although it is not required in this thesis, the code provided accepts vertically variable stratification.

The physical problem we seek to solve is

$$P_{zz} + P_{\widehat{x}\widehat{x}} - \hat{l}^2 P = 0 \tag{B.1}$$

where all dimensions (x, y, and z) are scaled by the maximum depth such that $\min(z) = -1$. For a complete derivation see Chapman (1982, hereafter C82). Terms with a hat are further scaled by R in the following way:

$$(\widehat{x}, \widehat{y}) = \left(\frac{x}{R}, \frac{y}{R}\right); \quad \hat{l} = lR; \quad R^2 = \frac{(N/f)^2 - \omega^2}{1 - \omega^2} \tag{B.2}$$

For consistency with C82, in this appendix l denotes along-ridge wavenumber (termed k_y elsewhere in this paper) and ω is non-dimensional (termed ω^* elsewhere). The expression for R^2 is the full expression (see Equation 4, not B1, in C82)

Over each flat region, P is a sum of modes whose coefficients A_n, B_n, C_n^j, and

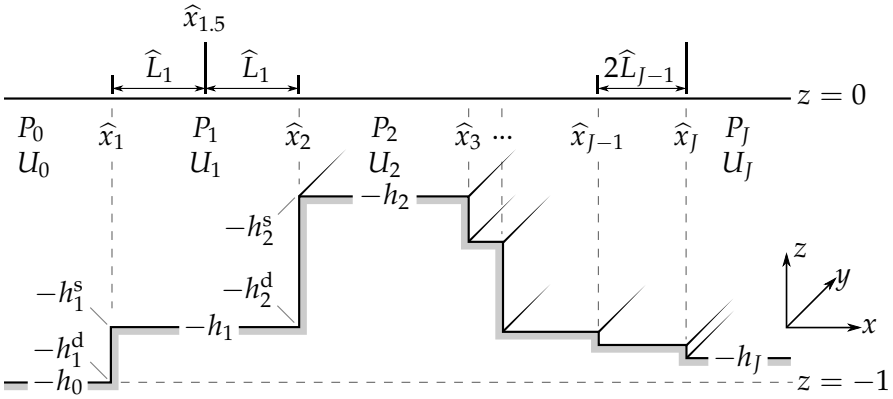

Figure B.1 – Notation used in the derivation of the ridge-trapped wave traveling in the positive y direction (into the page). In practice, the discontinuities would be chosen such that the ridge approximates a smooth surface, especially on the left-hand side. For clarity, this is not the case here.

D_n^j are to be found:

$$P_0 = \sum A_n \exp\left(\alpha_n(\hat{x} - \hat{x}_1)\right) \phi_n(h_0) \tag{B.3a}$$

$$P_J = \sum B_n \exp\left(-\beta_n(\hat{x} - \hat{x}_J)\right) \phi_n(h_J) \tag{B.3b}$$

$$P_j = \sum \left[C_n^j \frac{\cosh\left(\gamma_n^j(\hat{x} - \hat{x}_{j+1/2})\right)}{\cosh\left(\gamma_n^j \hat{L}_j\right)} + D_n^j \frac{\sinh\left(\gamma_n^j(\hat{x} - \hat{x}_{j+1/2})\right)}{\sinh\left(\gamma_n^j \hat{L}_j\right)} \right] \phi_n(h_j) \tag{B.3c}$$

All summations are over n from 0 to $n_{\max} = 20$ (or any desired value). For the constant stratification case

$$\alpha_n^2 = \left(\frac{n\pi}{h_0}\right)^2 + \hat{l}^2, \quad \beta_n^2 = \left(\frac{n\pi}{h_J}\right)^2 + \hat{l}^2, \quad \left(\gamma_n^j\right)^2 = \left(\frac{n\pi}{h_j}\right)^2 + \hat{l}^2 \tag{B.4}$$

and $\phi_n(h)$ is the nth vertical mode shape for a depth h:

$$\phi_n(h) = \cos\left(\frac{n\pi}{h}(z + h)\right) \tag{B.5}$$

The vertically variable stratification case is described at the end of this appendix.

The expressions in Equations B.3a and B.3b are reminiscent of the forms in C82, whereas Equation B.3c follows from Schmidt and Johnson (1997) who consider

waves traveling beside a tophat ridge. This form is chosen such that both P and its derivative simplify appreciably when evaluated at the discontinuities:

$$P_j\big|_{\hat{x}=\hat{x}_{j+1}} = \sum \left[C_n^j + D_n^j\right] \phi(h_j) \tag{B.6}$$

$$\mathrm{d}P_j/\mathrm{d}\hat{x}\big|_{\hat{x}=\hat{x}_{j+1}} = \sum \left[C_n^j \gamma_n^j \tanh\left(\gamma_n^j \hat{L}_j\right) + D_n^j \gamma_n^j \coth\left(\gamma_n^j \hat{L}_j\right)\right] \phi(h_j) \tag{B.7}$$

For a given discontinuity at $\widehat{x}_j$, pressure is matched by equating $P_j\big|_{\hat{x}_j}$ and $P_j\big|_{\hat{x}_{j-1}}$, multiplying both sides by $\phi_m(h_j^{\mathrm{s}})$, and then integrating vertically from $-h_j^{\mathrm{s}}$ to 0. The subscript s denotes the shallower of the two depths at $\widehat{x}_j$ (see Figure B.1). Undertaking this at all discontinuities leads to the following set of equations:

$$\int_{-h_1^{\mathrm{s}}}^{0} \sum A_n \phi_n(h_0)\phi_m(h_1^{\mathrm{s}})\,\mathrm{d}z = \int_{-h_1^{\mathrm{s}}}^{0} \sum \left[C_n^1 - D_n^1\right] \phi_n(h_1)\phi_m(h_1^{\mathrm{s}})\,\mathrm{d}z \tag{B.8}$$

$$\int_{-h_{j+1}^{\mathrm{s}}}^{0} \sum \left[C_n^j + D_n^j\right] \phi_n(h_j)\phi_m(h_{j+1}^{\mathrm{s}}) = \int_{-h_{j+1}^{\mathrm{s}}}^{0} \sum \left[C_n^{j+1} - D_n^{j+1}\right] \phi_n(h_{j+1})\phi_m(h_{j+1}^{\mathrm{s}}) \tag{B.9}$$

$$\int_{-h_J^{\mathrm{s}}}^{0} \sum \left[C_n^{J-1} + D_n^{J-1}\right] \phi_n(h_{J-1})\phi_m(h_J^{\mathrm{s}})\,\mathrm{d}z = \int_{-h_J^{\mathrm{s}}}^{0} \sum B_n \phi_n(h_J)\phi_m(h_J^{\mathrm{s}})\,\mathrm{d}z \tag{B.10}$$

The equivalent process for $U = \omega P_{\hat{x}} - \hat{l}P$ is somewhat messier. Equate U_j and U_{j+1} at the discontinuity at $\widehat{x}_{j+1}$, multiply by $\phi_m(h_{j+1}^{\mathrm{d}})$, and integrate vertically from h_j and h_{j+1} to zero. Integrating over different vertical ranges implicitly ensures that U is zero right against the step (i.e., in the range $-h_{j+1}^{\mathrm{d}} < z < -h_{j+1}^{\mathrm{d}}$ at $\widehat{x}_{j+1}$). The results are

$$\begin{aligned}\int_{-h_0}^{0} &\left[\omega\alpha_n A_n - \hat{l}A_n\right] \phi_n(h_0)\phi_m(h_1^{\mathrm{d}})\,\mathrm{d}z \\ &= \int_{-h_1}^{0} \left[-\omega C_n^1 \varepsilon_n^1 + \omega D_n^1 \zeta_n^1 - \hat{l}C_n^1 + \hat{l}D_n^1\right] \phi_n(h_1)\phi_m(h_1^{\mathrm{d}})\,\mathrm{d}z\end{aligned} \tag{B.11}$$

$$\int_{-h_j}^{0} \left[\omega C_n^j \varepsilon_n^j + \omega D_n^j \zeta_n^j - \hat{l} C_n^j - \hat{l} D_n^j\right] \phi_n(h_j)\phi_m(h_{j+1}^{\mathrm{d}})\,\mathrm{d}z =$$

$$\int_{-h_{j+1}}^{0} \left[-\omega C_n^{j+1} \varepsilon_n^{j+1} + \omega D_n^{j+1} \zeta_n^j - \hat{l} C_n^{j+1} + \hat{l} D_n^{j+1}\right] \phi_n(h_{j+1})\phi_m(h_{j+1}^{\mathrm{d}})\,\mathrm{d}z \quad \text{(B.12)}$$

$$\int_{-h_{J-1}}^{0} \left[\omega C_n^{J-1} \varepsilon_n^{J-1} + \omega D_n^{J-1} \zeta_n^{J-1} - \hat{l} C_n^{J-1} - \hat{l} D_n^{J-1}\right] \phi_n(h_{J-1})\phi_m(h_J^{\mathrm{d}})\,\mathrm{d}z =$$

$$\int_{-h_J}^{0} \left[-\omega \beta_n B_n - \hat{l} B_n\right] \phi_n(h_J)\phi_m(h_J^{\mathrm{d}})\,\mathrm{d}z \quad \text{(B.13)}$$

where

$$\varepsilon_n^j = \gamma_n^j \tanh\left(\gamma_n^j \hat{L}_j\right) \quad \text{(B.14)}$$

$$\zeta_n^j = \gamma_n^j \coth\left(\gamma_n^j \hat{L}_j\right) \quad \text{(B.15)}$$

To simplify notation, we introduce the following matrices

$$E_{mn}^j = \int_{-h_{j+1}^{\mathrm{s}}}^{0} \phi_n(h_j)\phi_m(h_{j+1}^{\mathrm{s}})\,\mathrm{d}z \quad \text{(B.16)}$$

$$F_{mn}^j = \int_{-h_j^{\mathrm{s}}}^{0} \phi_n(h_j)\phi_m(h_j^{\mathrm{s}})\,\mathrm{d}z \quad \text{(B.17)}$$

$$G_{mn}^j = \int_{-h_j}^{0} \phi_n(h_j)\phi_m(h_{j+1}^{\mathrm{d}})\,\mathrm{d}z \quad \text{(B.18)}$$

$$H_{mn}^j = \int_{-h_j}^{0} \phi_n(h_j)\phi_m(h_j^{\mathrm{d}})\,\mathrm{d}z \quad \text{(B.19)}$$

Equations B.8–B.13 can now be cast as a block matrix problem with terms involving ω on the right-hand side. An example with $J = 3$ demonstrates the general

form (with the *mn* indices dropped for clarity):

$$\begin{bmatrix} E^0 & -F^1 & F^1 & & & \\ & E^1 & E^1 & -F^{J-1} & F^{J-1} & \\ & & & E^{J-1} & E^{J-1} & -F^J \\ -\hat{l}G^0 & \hat{l}H^1 & -\hat{l}H^1 & & & \\ & -\hat{l}G^1 & -\hat{l}G^1 & \hat{l}H^{J-1} & -\hat{l}H^{J-1} & \\ & & & -\hat{l}G^{J-1} & -\hat{l}G^{J-1} & \hat{l}H^J \end{bmatrix} \begin{bmatrix} A \\ C^1 \\ D^1 \\ C^{J-1} \\ D^{J-1} \\ B \end{bmatrix} =$$

$$\omega \begin{bmatrix} & & & & & \\ & & & & & \\ & & & & & \\ -G^0\alpha & -H^1\varepsilon^1 & H^1\zeta^1 & & & \\ & -G^1\varepsilon^1 & -G^1\zeta^1 & -H^{J-1}\varepsilon^{J-1} & H^{J-1}\zeta^{J-1} & \\ & & & -G^{J-1}\varepsilon^{J-1} & -G^{J-1}\zeta^{J-1} & -H^J\beta \end{bmatrix} \begin{bmatrix} A \\ C^1 \\ D^1 \\ C^{J-1} \\ D^{J-1} \\ B \end{bmatrix} \tag{B.20}$$

For constant stratification, the matrices E, F, G, and H have analytical forms based on the special matrices P and Q to be defined:
If h_j is shallower than h_{j+1} ($h^{\mathrm{s}}_{j+1} = h_j$, $h^{\mathrm{d}}_{j+1} = h_{j+1}$):

$$E^j_{mn} = \int_{-h_j}^{0} \phi_n(h_j)\phi_m(h_j)\,\mathrm{d}z \qquad = P_{mn}(h_j) \tag{B.21}$$

$$G^j_{mn} = \int_{-h_j}^{0} \phi_n(h_j)\phi_m(h_{j+1})\,\mathrm{d}z \qquad = Q_{mn}(h_j, h_{j+1}) \tag{B.22}$$

If h_j is deeper than h_{j+1} ($h^{\mathrm{s}}_{j+1} = h_{j+1}$, $h^{\mathrm{d}}_{j+1} = h_j$):

$$E^j_{mn} = \int_{-h_{j+1}}^{0} \phi_n(h_j)\phi_m(h_{j+1})\,\mathrm{d}z \qquad * = Q_{nm}(h_{j+1}, h_j) \tag{B.23}$$

$$G^j_{mn} = \int_{-h_j}^{0} \phi_n(h_j)\phi_m(h_j)\,\mathrm{d}z \qquad = P_{mn}(h_j) \tag{B.24}$$

If h_j is shallower than h_{j-1} ($h_j^{\mathrm{s}} = h_j$, $h_j^{\mathrm{d}} = h_{j-1}$):

$$F_{mn}^j = \int_{-h_j}^{0} \phi_n(h_j)\phi_m(h_j)\,\mathrm{d}z \qquad = P_{mn}(h_j) \tag{B.25}$$

$$H_{mn}^j = \int_{-h_j}^{0} \phi_n(h_j)\phi_m(h_{j-1})\,\mathrm{d}z \qquad = Q_{mn}(h_j, h_{j-1}) \tag{B.26}$$

If h_j is deeper than h_{j-1} ($h_j^{\mathrm{s}} = h_{j-1}$, $h_j^{\mathrm{d}} = h_j$):

$$F_{mn}^j = \int_{-h_{j-1}}^{0} \phi_n(h_j)\phi_m(h_{j-1})\,\mathrm{d}z \qquad * = Q_{nm}(h_{j-1}, h_j) \tag{B.27}$$

$$H_{mn}^j = \int_{-h_j}^{0} \phi_n(h_j)\phi_m(h_j)\,\mathrm{d}z \qquad = P_{mn}(h_j) \tag{B.28}$$

Asterisks highlight transposed matrices (nm, not mn) as these are easy to miss. The special matrices P and Q are

$$P_{mn}(h) = \int_{-h}^{0} \cos\left(\frac{n\pi}{h}(z+h)\right)\cos\left(\frac{m\pi}{h}(z+h)\right)\,\mathrm{d}z \tag{B.29}$$
$$= h\delta_{mn}/2 + h\delta_{00}/2$$

$$Q_{mn}(h_1, h_2) = \int_{-h_1}^{0} \cos\left(\frac{n\pi}{h_1}(z+h_1)\right)\cos\left(\frac{m\pi}{h_2}(z+h_2)\right)\,\mathrm{d}z \tag{B.30}$$
$$= h_1 \qquad \text{if } m = n = 0$$
$$= \frac{(-1)^n}{2} h_1 \cos\left(\frac{h_2 n\pi}{h_1}\right) \qquad \text{if } mh_1 = nh_2$$
$$= \frac{h_1^2 h_2 m \sin\left(m\pi\frac{h_1-h_2}{h_2}\right)}{h_1^2 m^2\pi - h_2^2 n^2\pi} \qquad \text{otherwise}$$

As with the step-trapped Kelvin wave in Section 4.4.2, the block matrix equation (Equation B.20) is not a true eigenvalue equation because the eigenvalue ω is used in constructing the left-hand side. However, the problem can be solved in a small number of iterations by iteratively fitting a parabola to estimates of $(\omega, \hat{l})$ pairs.

To extend the problem to allow vertically variable stratification $N(z)$, we fol-

low Durran (2000) who provides the starting point for the equivalent atmospheric problem. Equation B.1 becomes

$$\left(\frac{P_z}{\widetilde{N}^2}\right)_z + P_{\hat{x}\hat{x}} - \hat{l}^2 P = 0 \tag{B.31}$$

where $\widetilde{N} = N/N_0$ with N_0 being the equivalent constant stratification that would produce the same internal Rossby radius. That is, $N_0 = c\pi/H$ with the non-rotating wave speed c found numerically (e.g., Kelly et al., 2013).

Vertical modes ϕ_n and eigenvalues γ_n (or α_n or β_n) are calculated from the following Sturm-Liouville problem:

$$\frac{\mathrm{d}}{\mathrm{d}z}\left(\frac{1}{\widetilde{N}^2}\frac{\mathrm{d}\phi}{\mathrm{d}z}\right) + \left(\gamma^2 - \hat{l}^2\right)\phi = 0 \tag{B.32}$$

Boundary conditions of $\mathrm{d}\phi/\mathrm{d}z = 0$ at the surface and seafloor are approximated with second-order, one-sided derivatives. Once the vertical eigenmodes and eigenvalues are found, the remainder of the calculation is the same as for the constant stratification case, albeit with the matching matrices evaluated numerically rather than using analytical forms.

To convert the ridge problem to a coastal problem where the seafloor goes to zero, we replace Equation B.3b with

$$P_J = \sum B_n \left[\exp\left(\beta_n\left(\hat{x} - \hat{x}_J - 2\hat{L}_J\right)\right) + \left(\frac{\omega\beta_n - \hat{l}}{\omega\beta_n + \hat{l}}\right)\exp\left(-\beta_n\left(\hat{x} - \hat{x}_J - 2\hat{L}_J\right)\right)\right]\phi_n(h_J) \tag{B.33}$$

This form follows from Chapman and Hendershott (1982) and ensures that the velocity at the wall that intersects the seafloor is zero. Consequently, three of the submatrices in Equation B.20 change:

$$-F^J, \hat{l}H^J, -H^J\beta \rightarrow (-F^J, \hat{l}H^J, +H^J)\times \left[\exp\left(-2\beta\hat{L}_J\right) + (1,1,-1)\times\left(\frac{\omega\beta - \hat{l}}{\omega\beta + \hat{l}}\right)\exp\left(2\beta\hat{L}_J\right)\right] \tag{B.34}$$

Note that we have not strictly separated the ω and non-ω terms onto the right

and left sides, respectively.

References

Adcroft, A., C. Hill, J.-M. Campin, J. Marshall and P. Heimbach (2004), Overview of the formulation and numerics of the MIT GCM, in *Proceedings of the ECMWF seminar series on Numerical Methods, Recent developments in numerical methods for atmosphere and ocean modelling*, pp. 139–149.

Alford, M. H., J. B. Girton, G. Voet, G. S. Carter, J. B. Mickett and J. M. Klymak (2013), Turbulent mixing and hydraulic control of abyssal water in the Samoan Passage, *Geophys. Res. Lett.*, 40, 4668–4674, doi:10.1002/grl.50684.

Alford, M. H., T. Peacock, J. A. MacKinnon et al. (2015), The formation and fate of internal waves in the South China Sea, *Nature*, 521, 65–69, doi:10.1038/nature14399.

Armi, L. (1986), The hydraulics of two flowing layers with different densities, *J. Fluid Mech.*, 163, 27–58, doi:10.1017/S0022112086002197.

Armi, L. and D. Farmer (1985), The internal hydraulics of the Strait of Gibraltar and associated sills and narrows, *Oceanol. Acta*, 8(1), 37–46.

Armi, L. and D. M. Farmer (1986), Maximal two-layer exchange through a contraction with barotropic net flow, *J. Fluid Mech.*, 164, 27–51, doi:10.1017/S0022112086002458.

Arneborg, L., P. Jansson, A. Staalstrøm and G. Broström (2017), Tidal energy loss, internal tide radiation, and local dissipation for two-layer tidal flow over a sill, *J. Phys. Oceanogr.*, 47, 1521–1538, doi:10.1175/JPO-D-16-0148.1.

Baines, P. G. (1987), Upstream blocking and airflow over mountains, *Ann. Rev. Fluid Mech.*, 19, 75–97, doi:10.1146/annurev.fl.19.010187.000451.

Baines, P. G. (1995), *Topographic effects in stratified flows*, Cambridge Univ. Press.

Balmforth, N. J. and T. Peacock (2009), Tidal conversion by supercritical topography, *J. Phys. Oceanogr.*, 39, 1965–1974, doi:10.1175/2009JPO4057.1.

Beckmann, A. and R. Döscher (1997), A method for improved representation of dense water spreading over topography in geopotential-coordinate models, *J. Phys. Oceanogr.*, 27, 581–591, doi:10.1175/1520-0485(1997)027<0581:AMFIRO>2.0.CO;2.

Belkin, I. M., S. Levitus, J. Antonov and S.-A. Malmberg (1998), "Great Salinity Anomalies" in the North Atlantic, *Prog. Oceanogr.*, 41, 1–68, doi:10.1016/S0079-6611(98)00015-9.

Berntsen, J., J. Xing and A. M. Davies (2009), Numerical studies of flow over a sill: sensitivity of the non-hydrostatic effects to the grid size, *Ocean Dyn.*, 59, 1043–1059, doi:10.1007/s10236-009-0227-0.

Beszczynska-Möller, A., R. A. Woodgate, C. Lee, H. Melling and M. Karcher (2011), A synthesis of exchanges through the main oceanic gateways to the Arctic Ocean, *Oceanography*, 24(3), 82–99, doi:10.5670/oceanog.2011.59.

Brink, K. H. (1989), The effect of stratification on seamount-trapped waves, *Deep-Sea Res.*, 36, 825–844, doi:10.1016/0198-0149(89)90031-9.

Brink, K. H. (2006), Coastal-trapped waves with finite bottom friction, *Dyn. Atmos. Oceans*, 41, 172–190, doi:10.1016/j.dynatmoce.2006.05.001.

Broecker, W. S. (1991), The great ocean conveyor, *Oceanography*, 4, 79–89, doi:10.5670/oceanog.1991.07.

Buijsman, M. C., J. M. Klymak, S. Legg et al. (2014), Three-dimensional double-ridge internal tide resonance in Luzon Strait, *J. Phys. Oceanogr.*, 44, 850–869, doi:10.1175/JPO-D-13-024.1.

Buijsman, M. C., S. Legg and J. Klymak (2012), Double-ridge internal tide interference and its effect on dissipation in Luzon Strait, *J. Phys. Oceanogr.*, 42, 1337–1356, doi:10.1175/JPO-D-11-0210.1.

Carmack, E., F. McLaughlin, M. Yamamoto-Kawai, M. Itoh, K. Shimada, R. Krishfield and A. Proshutinsky (2008), Freshwater storage in the northern ocean and the special role of the Beaufort Gyre, in R. R. Dickson, J. Meincke and P. Rhines (eds.), *Arctic-subarctic ocean fluxes: Defining the role of the Northern Seas in climate*, Springer, pp. 145–169, doi:10.1007/978-1-4020-6774-7_8.

Carmack, E. C. (2007), The alpha/beta ocean distinction: A perspective on freshwater fluxes, convection, nutrients and productivity in high-latitude seas, *Deep-Sea Res. II*, 54, 2578–2598, doi:10.1016/j.dsr2.2007.08.018.

Carmack, E. C., M. Yamamoto-Kawai, T. W. N. Haine et al. (2016), Freshwater and its role in the Arctic Marine System: Sources, disposition, storage, export, and physical and biogeochemical consequences in the Arctic and global oceans, *J. Geophys. Res.*, 121, doi:10.1002/2015JG003140.

Chapman, D. C. (1982), On the failure of Laplace's tidal equations to model subinertial motions at a discontinuity in depth, *Dyn. Atmos. Oceans*, 7, 1–16, doi:10.1016/0377-0265(82)90002-1.

Chapman, D. C. and M. C. Hendershott (1982), Shelf wave dispersion in a geophysical ocean, *Dyn. Atmos. Oceans*, 7, 17–31, doi:10.1016/0377-0265(82)90003-3.

Chelton, D. B., R. A. DeSzoeke, M. G. Schlax, K. El Naggar and N. Siwertz (1998), Geographical variability of the first baroclinic Rossby radius of deformation, *J. Phys. Oceanogr.*, 28(3), 433–460, doi:10.1175/1520-0485(1998)028<0433:GVOTFB>2.0.CO;2.

Chen, C., G. Gao, J. Qi, A. Proshutinsky, R. C. Beardsley, Z. Kowalik, H. Lin and G. Cowles (2009), A new high-resolution unstructured grid finite volume Arctic Ocean model (AO-FVCOM): An application for tidal studies, *J. Geophys. Res.*, 114, C08017, doi:10.1029/2008JC004941.

Chen, C., G. Gao, Y. Zhang, R. C. Beardsley, Z. Lai, J. Qi and H. Lin (2016), Circulation in the Arctic Ocean: Results from a high-resolution coupled ice-sea nested Global-FVCOM and Arctic-FVCOM system, *Prog. Oceanogr.*, 141, 60–80, doi:10.1016/j.pocean.2015.12.002.

Collins, A. K., C. G. Hannah and D. Greenberg (2011), Validation of a high resolution modelling system for tides in the Canadian Arctic Archipelago, *Can. Tech. Rep. Hydrog. Ocean Sci.*, 273, vii + 72pp.

Cottier, F. R., F. Nilsen, R. Skogseth, V. Tverberg, J. Skarðhamar and H. Svendsen (2010), Arctic fjords: a review of the oceanographic environment and dominant physical processes, in J. A.

Howe, W. E. N. Austin, M. Forwick and M. Paetzel (eds.), *Fjord Systems and Archives*, vol. 344, Geol. Soc. Lond., pp. 35–50, doi:10.1144/SP344.4.

Crawford, G., L. Padman and M. McPhee (1999), Turbulent mixing in Barrow Strait, *Cont. Shelf Res.*, 19, 205–245, doi:10.1016/S0278-4343(98)00086-7.

Csanady, G. (1977), The coastal jet conceptual model in the dynamics of shallow seas, in E. D. Goldberg, I. N. McCave, J. J. O'Brien and J. H. Steele (eds.), *The sea*, vol. 6, pp. 117–144.

Dale, A. C., J. M. Huthnance and T. J. Sherwin (2001), Coastal-trapped waves and tides at near-inertial frequencies, *J. Phys. Oceanogr.*, 31, 2958–2970, doi:10.1175/1520-0485(2001)031<2958:CTWATA>2.0.CO;2.

Dale, A. C. and T. J. Sherwin (1996), The extension of baroclinic coastal-trapped wave theory to superinertial frequencies, *J. Phys. Oceanogr.*, 26, 2305–2315, doi:10.1175/1520-0485(1996)026<2305:TEOBCT>2.0.CO;2.

D'Alembert, J. L. R. (1752), *Essai d'une nouvelle theorie de la résistance des fluides*, David l'aîné.

de Lange Boom, B. R., H. Melling and R. A. Lake (1987), Late winter hydrography of the Northwest Passage: 1982, 1983 and 1984, *Can. Tech. Rep. Hydrogr. Ocean Sci.*, (79), 165 pp.

de Young, B. and S. Pond (1989), Partition of energy loss from the barotropic tide in fjords, *J. Phys. Oceanogr.*, 19(Feb), 246–252, doi:10.1175/1520-0485(1989)019<0246:POELFT>2.0.CO;2.

Dewey, R., D. Richmond and C. Garrett (2005), Stratified tidal flow over a bump, *J. Phys. Oceanogr.*, 35(10), 1911–1927, doi:10.1175/JPO2799.1.

Durran, D. R. (2000), Small-amplitude coastally trapped disturbances and the reduced-gravity shallow-water approximation, *Q. J. R. Meteorol. Soc.*, 126, 2671–2689, doi:10.1002/qj.49712656904.

Egbert, G. D. (1997), Tidal data inversion: Interpolation and inference, *Prog. Oceanogr.*, 40, 53–80, doi:10.1016/S0079-6611(97)00023-2.

Falahat, S. and J. Nycander (2015), On the generation of bottom-trapped internal tides, *J. Phys. Oceanogr.*, 45, 526–545, doi:10.1175/JPO-D-14-0081.1.

Farmer, D. M. and L. Armi (1986), Maximal two-layer exchange over a sill and through the combination of a sill and contraction with barotropic flow, *J. Fluid Mech.*, 164, 53–76, doi:10.1017/S002211208600246X.

Farmer, D. M. and L. Armi (1999), Stratified flow over topography: The role of small scale entrainment and mixing in flow establishment, *Proc. Roy. Soc. London*, 455, 3221–3258, doi:10.1098/rspa.1999.0448.

Farmer, D. M. and R. A. Denton (1985), Hydraulic control of flow over the sill in Observatory Inlet, *J. Geophys. Res.*, 90(C5), 9051–9068, doi:10.1029/JC090iC05p09051.

Fer, I., E. Darelius and K. B. Daae (2016), Observations of energetic turbulence on the Weddell Sea continental slope, *Geophys. Res. Lett.*, 43, 760–766, doi:10.1002/2015GL067349.

Fer, I., M. M uller and A. K. Peterson (2015), Tidal forcing, energetics, and mixing near the Yermak Plateau, *Ocean Science*, 11, 287–304, doi:10.5194/os-11-287-2015.

Ferron, B., H. Mercier, K. Speer, A. Gargett and K. Polzin (1998), Mixing in the Romanche Fracture Zone, *J. Phys. Oceanogr.*, 28, 1929–1945, doi:10.1175/1520-0485(1998)028<1929:MITRFZ>2.0.CO;2.

Ferry, N., L. Parent, G. Garric, B. Barnier, N. C. Jourdain and the Mercator Ocean Team (2010), Mercator global eddy permitting ocean reanalysis GLORYS1V1: Description and results, *Mercator Ocean Quart. Newsl.*, 36, 15–27.

Fichefet, T. and M. A. Morales Maqueda (1997), Sensitivity of a global sea ice model to the treatment of ice thermodynamics and dynamics, *J. Geophys. Res.*, 102(C6), 12609–12646, doi:10.1029/97JC00480.

Firing, E., J. Ranada and P. Caldwell (1995), Processing ADCP data with the CODAS Software System Version 3.1, *Joint Institute for Marine and Atmospheric Research, University of Hawaii and National Oceanographic Data Center*.

Fissel, D. B., D. Lemon and D. N. Knight (1984), An oceanographic survey of the Canadian Arctic Archipelago March 1983, Institute of Ocean Sciences, Sidney, B.C., *Can. Contr. Rep. of Hydrogr. Ocean Sci.*, 355pp.

Flater, D. (2016), XTide (version 2.15), `http://www.flaterco.com/xtide/`.

Freeland, H. J. and D. M. Farmer (1980), Circulation and energetics of a deep, strongly stratified inlet, *Can. J. Fish Aquat. Sci.*, 37, 1398–1410, doi:10.1139/f80-179.

Gargett, A. and T. Garner (2008), Determining Thorpe scales from ship-lowered CTD density profiles, *J. Atmos. Oceanic Tech.*, 25, 1657–1670, doi:10.1175/2008JTECHO541.1.

Garrett, C. (2004), Frictional processes in straits, *Deep-Sea Res. II*, 51, 393–410, doi:10.1016/j.dsr2.2003.10.005.

Gemmrich, J. and J. M. Klymak (2015), Dissipation of internal wave energy generated on a critical slope, *J. Phys. Oceanogr.*, 45, 2221–2238, doi:10.1175/JPO-D-14-0236.1.

Gerkema, T. and V. I. Shrira (2005), Near-inertial waves on the "nontraditional" β plane, *J. Geophys. Res.*, 110, C01003, doi:10.1029/2004JC002519.

Goosse, H., T. Fichefet and J.-M. Campin (1997), The effects of the water flow through the Canadian Archipelago in a global ice–ocean model, *Geophys. Res. Lett.*, 24(12), 1507–1510, doi:10.1029/97GL01352.

Gregg, M. and E. Özsoy (2002), Flow, water mass changes, and hydraulics in the Bosphorus, *J. Geophys. Res.*, 107(C3), doi:10.1029/2000JC000485.

Gregg, M. C., D. W. Winkel, J. A. MacKinnon and R. C. Lien (1999), Mixing over shelves and slopes, in P. Müller and D. Henderson (eds.), *Dynamics of oceanic internal gravity waves II, Proceedings, Hawaiian Winter Workshop*, pp. 35–42.

Hannah, C. G., F. Dupont and M. Dunphy (2009), Polynyas and tidal currents in the Canadian Arctic Archipelago, *Arctic*, 62(1), 83–95, doi:10.14430/arctic115.

Hogg, N., P. Biscaye, W. Gardner and W. J. Schmitz Jr. (1982), On the transport and modification of Antarctic Bottom Water in the Vema Channel, *J. Mar. Res.*, 40, suppl., 231–263.

Houssais, M.-N. and C. Herbaut (2011), Atmospheric forcing on the Canadian Arctic Archipelago freshwater outflow and implications for the Labrador Sea variability, *J. Geophys. Res.*, 116, C00D02, doi:10.1029/2010JC006323.

Hu, X. and P. G. Myers (2014), Changes to the Canadian Arctic Archipelago sea ice and freshwater fluxes in the twenty-first century under the Intergovernmental Panel on Climate Change A1B climate scenario, *Atmosphere-Ocean*, 52(4), 331–350, doi:10.1080/07055900.2014.942592.

Hu, X., J. Sun, T. O. Chan and P. G. Myers (2018), Thermodynamic and dynamic ice thickness contributions in the Canadian Arctic Archipelago in NEMO-LIM2 numerical simulations, *The Cryosphere*, 12, 1233–1247, doi:10.5194/tc-12-1233-2018.

Huthnance, J., L. Mysak and D.-P. Wang (1986), Coastal trapped waves, in C. N. K. Mooers (ed.), *Baroclinic Processes on Continental Shelves*, American Geophysical Union, Washington, D. C., pp. 1–18, doi:10.1029/CO003p0001.

Huthnance, J. M. (1975), On trapped waves over a continental shelf, *J. Fluid. Mech.*, 69, 689–704, doi:10.1017/S0022112075001632.

Huthnance, J. M. (1978), On coastal trapped waves: analysis and numerical calculation by inverse iteration, doi:10.1175/1520-0485(1978)008<0074:OCTWAA>2.0.CO;2.

Inall, M., T. Rippeth, C. Griffiths and P. Wiles (2005), Evolution and distribution of TKE production and dissipation within stratified flow over topography, *Geophys. Res. Lett.*, 32, L08607, doi:10.1029/2004GL022289.

Inall, M. E. and T. P. Rippeth (2002), Dissipation of tidal energy and associated mixing in a wide fjord, *Environ. Fluid Mech*, 2, 219–240, doi:10.1023/A:1019846829875.

Ivey, G. N., K. B. Winters and J. R. Koseff (2008), Density stratification, turbulence, but how much mixing?, *Annu. Rev. Fluid Mech.*, 40, 169–184, doi:10.1146/annurev.fluid.39.050905.110314.

Jahn, A., Y. Aksenov, B. A. de Cuevas et al. (2012), Arctic Ocean freshwater: How robust are model simulations?, *J. Geophys. Res.*, 117, C00D16, doi:10.1029/2012JC007907.

Johnson, E. R. and J. T. Rodney (2011), Spectral methods for coastal-trapped waves, *Cont.Shelf Res.*, 31, 1481–1489, doi:10.1016/j.csr.2011.06.009.

Joyce, T. M. and A. Proshutinsky (2007), Greenland's island rule and the Arctic Ocean circulation, *J. Mar. Res.*, 65, 639–653, doi:10.1357/002224007783649439.

Kagan, B. A., E. V. Sofina and A. A. Timofeev (2010), On diapycnal mixing induced by internal tidal waves in the Arctic Ocean, *Izvestiya Atmos. Oceanic Phys.*, 46, 224–231, doi:10.1134/S0001433810020106.

Kang, D. (2011), *Energetics and dynamics of internal tides in Monterey Bay using numerical simulations*, Ph.D. dissertation, Stanford University.

Kang, D. and O. Fringer (2012), Energetics of barotropic and baroclinic tides in the Monterey Bay area, *J. Phys. Oceanogr.*, 42, 272–290, doi:10.1175/JPO-D-11-039.1.

Kelly, S. M., N. L. Jones and J. D. Nash (2013), A coupled model for laplace's tidal equations in a fluid with one horizontal dimension and variable depth, *J. Phys. Oceanogr.*, 43, 1780–1797, doi:10.1175/JPO-D-12-0147.1.

Kliem, N. and D. A. Greenberg (2003), Diagnostic simulations of the summer circulation in the Canadian Arctic Archipelago, *Atmosphere-Ocean*, 41(4), 273–289, doi:10.3137/ao.410402.

Klymak, J. M., M. Buijsman, S. Legg and R. Pinkel (2013), Parameterizing surface and internal tide scattering and breaking on supercritical topography: the one- and two-ridge cases, *J. Phys. Oceanogr.*, 43, 1380–1397, doi:10.1175/JPO-D-12-061.1.

Klymak, J. M. and M. C. Gregg (2001), Three-dimensional nature of flow near a sill, *J. Geophys. Res.*, 106(C10), 22295–22311, doi:10.1029/2001JC000933.

Klymak, J. M. and M. C. Gregg (2003), The role of upstream waves and a downstream density pool in the growth of lee waves; stratified flow over the Knight Inlet sill, *J. Phys. Oceanogr.*, 33, 1446–1461, doi:10.1175/1520-0485(2003)033<1446:TROUWA>2.0.CO;2.

Klymak, J. M. and M. C. Gregg (2004), Tidally generated turbulence over the Knight Inlet Sill, *J. Phys. Oceanogr.*, 34, 1135–1151, doi:10.1175/1520-0485(2004)034<1135:TGTOTK>2.0.CO;2.

Klymak, J. M., S. Legg, M. H. Alford, M. Buijsman, R. Pinkel and J. D. Nash (2012), The direct breaking of internal waves at steep topography, *Oceanography*, 25(2), 150–159, doi:10.5670/oceanog.2012.50.

Klymak, J. M., S. Legg and R. Pinkel (2010a), A simple parameterization of turbulent tidal mixing near supercritical topography, *J. Phys. Oceanogr.*, 40, 2059–2074, doi:10.1175/2010JPO4396.1.

Klymak, J. M. and S. M. Legg (2010), A simple mixing scheme for models that resolve breaking internal waves, *Ocean Modell.*, 33, 224–234, doi:10.1016/j.ocemod.2010.02.005.

Klymak, J. M., S. M. Legg and R. Pinkel (2010b), High-mode stationary waves in stratified flow over large obstacles, *J. Fluid Mech.*, 644, 321–336, doi:10.1017/S0022112009992503.

Klymak, J. M., H. L. Simmons, D. Braznikov, S. Kelly, J. A. MacKinnon, M. H. Alford, R. Pinkel and J. D. Nash (2016), Reflection of linear internal tides from realistic topography: The Tasman continental slope, *J. Phys. Oceanogr.*, 46, JPO–D–16–0061.1, doi:10.1175/JPO-D-16-0061.1.

Komuro, Y. and H. Hasumi (2005), Intensification of the Atlantic deep circulation by the Canadian Archipelago throughflow, *J. Phys. Oceanogr.*, 35(5), 775–789, doi:10.1175/JPO2709.1.

Kowalik, Z. and A. Y. Proshutinsky (1993), Diurnal tides in the Arctic Ocean, *J. Geophys. Res.*, 98(C9), 16449–16468, doi:10.1029/93JC01363.

Lawrence, G. A. (1993), The hydraulics of steady two-layer flow over a fixed obstacle, *J. Fluid Mech.*, 254, 605–633, doi:10.1017/S0022112093002277.

Leblond, P. H. (1980), On the surface circulation in some channels of the Canadian Arctic Archipelago, *Arctic*, 33(1), 189–197, doi:10.14430/arctic2554.

Lerczak, J. a., M. C. Hendershott and C. D. Winant (2001), Observations and modeling of coastal internal waves driven by a diurnal sea breeze, *J. Geophys. Res.*, 106, 19715–19729, doi:10.1029/2001JC000811.

Lindsay, R. (2013), Unified sea ice thickness climate data record collection spanning 1947-2012, Version 1, doi:10.7265/N5D50JXV.

Llewellyn Smith, S. G. and W. R. Young (2003), Tidal conversion at a very steep ridge, *J. Fluid Mech.*, 495, 175–191, doi:10.1017/S0022112003006098.

Lu, Y., S. Higginson, S. Nudds, S. Prinsenberg and G. Garric (2014), Model simulated volume fluxes through the Canadian Arctic Archipelago and Davis Strait: Linking monthly variations to forcing in different seasons, *J. Geophys. Res.*, 119, 1927–1942, doi:10.1002/2013JC009408.

Lu, Y., R. G. Lueck and D. Huang (2000), Turbulence characteristics in a tidal channel, *J. Phys. Oceanogr.*, 30, 855–867, doi:10.1175/1520-0485(2000)030<0855:TCIATC>2.0.CO;2.

Lueck, R. and T. Osborn (1985), Turbulence measurements in a submarine canyon, *Cont. Shelf Res.*, 4, 681–698, doi:10.1016/0278-4343(85)90036-6.

Luneva, M. V., Y. Aksenov, J. D. Harle and J. T. Holt (2015), The effects of tides on the water mass mixing and sea ice in the Arctic Ocean, *J. Geophys. Res.*, 120(10), 6669–6699, doi:10.1002/2014JC010310.

MacCready, P., G. Pawlak, K. Edwards and R. McCabe (2003), Form drag on ocean flows, in *Proceedings of the 13th'Aha Huliko'a Hawaiian Winter Workshop on Near Boundary Processes and their Parameterization*, pp. 119–130.

Madec, G. and the NEMO team (2008), *NEMO ocean engine*, Institut Pierre-Simon Laplace No. 27.

Marsden, R., R. Ingram and L. Legendre (1994a), Currents under land-fast ice in the Canadian Arctic Archipelago part 2: Vertical mixing, *J. Mar. Res.*, 52, 1037–1049, doi:10.1357/0022240943076812.

Marsden, R., R. Paquet and R. Ingram (1994b), Currents under land-fast ice in the Canadian Arctic Archipelago part 1: Vertical velocities, *J. Mar. Res.*, 52, 1017–1036, doi:10.1357/0022240943076795.

Marshall, J., A. Adcroft, C. Hill, L. Perelman and C. Heisey (1997), A finite-volume, incompressible Navier Stokes model for studies of the ocean on parallel computers, *J. Geophys. Res.*, 102, 5753–5766, doi:10.1029/96JC02775.

Masunaga, E., O. B. Fringer, Y. Kitade, H. Yamazaki and S. M. Gallager (2017), Dynamics and energetics of trapped diurnal internal Kelvin waves around a mid-latitude island, *J. Phys. Oceanogr.*, 47, 2479–2498, doi:10.1175/JPO-D-16-0167.1.

McGeehan, T. and W. Maslowski (2012), Evaluation and control mechanisms of volume and freshwater export through the Canadian Arctic Archipelago in a high-resolution pan-Arctic ice-ocean model, *J. Geophys. Res.*, 117, 1–25, doi:10.1029/2011JC007261.

McLaughlin, F. A., E. C. Carmack, R. G. Ingram, W. J. Williams and C. Michel (2004), Oceanography of the Northwest Passage, in A. R. Robinson and K. H. Brink (eds.), *The Sea*, vol. 14, chap. 31, pp. 1211–1242.

Melling, H. (2000), Exchanges of freshwater through the shallow straits of the North American Arctic, in E. L. Lewis, P. J. Jones, P. Lemke, T. D. Prowse and P. Wadhams (eds.), *The Freshwater Budget of the Arctic Ocean*, Springer, pp. 479–502, doi:10.1007/978-94-011-4132-1_20.

Melling, H., T. A. Agnew, K. K. Falkner et al. (2008), Fresh-water fluxes via Pacific and Arctic outflows across the Canadian Polar Shelf, in R. R. Dickson, J. Meincke and P. Rhines (eds.), *Arctic–Subarctic Ocean Fluxes: Defining the role of the Northern Seas in Climate*, Springer, pp. 193–247, doi:10.1007/978-1-4020-6774-7_10.

Melling, H., C. Haas and E. Brossier (2015), Invisible polynyas: Modulation of fast ice thickness by ocean heat flux on the Canadian polar shelf, *J. Geophys. Res.*, 120, 777–795, doi:10.1002/2014JC010404.

Melling, H., R. Lake, D. Topham and D. Fissel (1984), Oceanic thermal structure in the western Canadian Arctic, *Cont. Shelf Res.*, 3(3), 233–258, doi:10.1016/0278-4343(84)90010-4.

Meyer, A., I. Fer, A. Sundfjord and A. K. Peterson (2017), Mixing rates and vertical heat fluxes north of Svalbard from Arctic winter to spring, *J. Geophys. Res.*, 122, 4569–4586, doi:10.1002/2016JC012441.

Michel, C., R. G. Ingram and L. R. Harris (2006), Variability in oceanographic and

ecological processes in the Canadian Arctic Archipelago, *Prog. Oceanogr.*, 71, 379–401, doi:10.1016/j.pocean.2006.09.006.

Mihanović, H., G. Beg Paklar and M. Orlić (2014), Resonant excitation of island-trapped waves in a shallow, seasonally stratified sea, *Cont. Shelf Res.*, 77, 24–37, doi:10.1016/j.csr.2014.01.014.

Moum, J. N., J. D. Nash and J. M. Klymak (2008), Small scale processes in the coastal ocean, *Oceanography*, 21(4), doi:10.5670/oceanog.2008.02.

Münchow, A., K. K. Falkner and H. Melling (2007), Spatial continuity of measured seawater and tracer fluxes through Nares Strait, a dynamically wide channel bordering the Canadian Archipelago, *J. Mar. Res.*, 65(6), 759–788, doi:10.1357/002224007784219048.

Munk, W. and C. Wunsch (1998), Abyssal recipes II: energetics of tidal and wind mixing, *Deep-Sea Res.*, 45(12), 1977–2010, doi:10.1016/S0967-0637(98)00070-3.

Musgrave, R. C., J. A. MacKinnon, R. Pinkel, A. F. Waterhouse, J. Nash and S. M. Kelly (2017), The influence of subinertial internal tides on near-topographic turbulence at the Mendocino Ridge: Observations and Modeling., *J. Phys. Oceanogr.*, 47, 2139–2154, doi:10.1175/JPO-D-16-0278.1.

Musgrave, R. C., J. A. MacKinnon, R. Pinkel, A. F. Waterhouse and J. D. Nash (2016a), Tidally driven processes leading to near-field turbulence in a channel at the crest of the Mendocino Escarpment, *J. Phys. Oceanogr.*, 46, 1137–1155, doi:10.1175/JPO-D-15-0021.1.

Musgrave, R. C., R. Pinkel, J. A. MacKinnon, M. R. Mazloff and W. R. Young (2016b), Stratified tidal flow over a tall ridge above and below the turning latitude, *J. Fluid Mech.*, 793, 933–957, doi:10.1017/jfm.2016.150.

Myers, P. G. (2005), Impact of freshwater from the Canadian Arctic Archipelago on Labrador Sea Water formation, *Geophys. Res. Lett.*, 32, L06605, doi:10.1029/2004GL022082.

Nakamura, T., T. Awaji, T. Hatayama, K. Akitomo, T. Takizawa, T. Kono, Y. Kawasaki and M. Fukasawa (2000), The generation of large-amplitude unsteady lee waves by subinertial K_1 tidal flow: A possible vertical mixing mechanism in the Kuril Straits, *J. Phys. Oceanogr.*, 30, 1601–1621, doi:10.1175/1520-0485(2000)030<1601:TGOLAU>2.0.CO;2.

Nash, J. D. and J. N. Moum (2001), Internal hydraulic flows on the continental shelf: High drag states over a small bank, *J. Geophys. Res.*, 106, 4593–4611, doi:10.1029/1999jc000183.

Niwa, Y. and T. Hibiya (2011), Estimation of baroclinic tide energy available for deep ocean mixing based on three-dimensional global numerical simulations, *J. Oceanogr.*, 67, 493–502, doi:10.1007/s10872-011-0052-1.

Osborn, T. R. (1980), Estimates of the local rate of vertical diffusion from dissipation measurements, *J. Phys. Oceanogr.*, 10(1), 83–89, doi:10.1175/1520-0485(1980)010<0083:EOTLRO>2.0.CO;2.

Peterson, I., J. Hamilton, S. Prinsenberg and R. Pettipas (2012), Wind-forcing of volume transport through Lancaster Sound, *J. Geophys. Res.*, 117, C11018, doi:10.1029/2012JC008140.

Polzin, K. L. (2009), An abyssal recipe, *Ocean Modelling*, 30, 298–309, doi:10.1016/j.ocemod.2009.07.006.

Prandle, D. (1982), The vertical structure of tidal currents, *Geophys. Astrophys. Fluid Dyn.*, 22, 29–49, doi:10.1080/03091928208221735.

Pratt, L. and P. Lundberg (1991), Hydraulics of rotating strait and sill flow, *Annu. Rev. Fluid Mech.*, 23, 81–106, doi:10.1146/annurev.fl.23.010191.000501.

Pratt, L. J. and J. A. Whitehead (2008), *Rotating hydraulics: Nonlinear topographic effects in the ocean and atmosphere*, Springer, doi:10.1007/978-0-387-49572-9.

Prinsenberg, S. and J. Hamilton (2005), Monitoring the volume, freshwater and heat fluxes passing through Lancaster Sound in the Canadian Arctic Archipelago, *Atmosphere-Ocean*, 43(1), 1–22, doi:10.3137/ao.430101.

Prinsenberg, S., J. Hamilton, I. Peterson and R. Pettipas (2009), Observing and interpreting the seasonal variability of the oceanographic fluxes passing through Lancaster Sound of the Canadian Arctic Archipelago, in *Influence of Climate Change on the Changing Arctic and Sub-Arctic Conditions*, pp. 125–143, doi:10.1007/978-1-4020-9460-6_10.

Prinsenberg, S. J. and E. B. Bennett (1987), Mixing and transports in Barrow Strait, the central part of the Northwest Passage, *Cont. Shelf Res.*, 7(8), 913–935, doi:10.1016/0278-4343(87)90006-9.

Prinsenberg, S. J. and E. B. Bennett (1989), Transport between Peel Sound and Barrow Strait in the Canadian Arctic, *Cont. Shelf Res.*, 9(5), 427–444, doi:10.1016/0278-4343(89)90008-3.

Rainville, L., C. M. Lee and R. A. Woodgate (2011), Impact of wind-driven mixing in the Arctic Ocean, *Oceanography*, 24, 136–145, doi:10.5670/oceanog.2011.65.

Rainville, L. and P. Winsor (2008), Mixing across the Arctic Ocean: Microstructure observations during the Beringia 2005 Expedition, *Geophys. Res. Lett.*, 35, L08606, doi:10.1029/2008GL033532.

Rippeth, T. P., B. J. Lincoln, Y.-D. Lenn, J. A. M. Green, A. Sundfjord and S. Bacon (2015), Tide-mediated warming of Arctic halocline by Atlantic heat fluxes over rough topography, *Nature Geosci.*, 8, 191–194, doi:10.1038/ngeo2350.

Rippeth, T. P., V. Vlasenko, N. Stashchuk, B. D. Scannell, J. A. M. Green, B. J. Lincoln and S. Bacon (2017), Tidal conversion and mixing poleward of the critical latitude (an Arctic case study), *Geophys. Res. Lett.*, 44, doi:10.1002/2017GL075310.

Samelson, R. M. (1999), The vertical structure of linear coastal-trapped disturbances, *Mon. Weather Rev.*, 127, 201–213, doi:10.1175/1520-0493(1999)127<0201:TVSOLC>2.0.CO;2.

Sánchez-Garrido, J. C., G. Sannino, L. Liberti et al. (2011), Numerical modeling of three-dimensional stratified tidal flow over Camarinal Sill, Strait of Gibraltar, *J. Geophys. Res.*, 116, C12026, doi:10.1029/2011JC007093.

Sarkar, S. and A. Scotti (2017), From topographic internal gravity waves to turbulence, *Annu. Rev. Fluid Mech.*, 49, 195–220, doi:10.1146/annurev-fluid-010816-060013.

Schmidt, G. A. and E. Johnson (1997), Instability in stratified rotating shear flow along ridges, *J. Mar. Res.*, 55, 915–933, doi:10.1357/0022240973224201.

Seim, H. E. and M. C. Gregg (1994), Detailed observations of a naturally occurring shear instability., *J. Geophys. Res.*, 99(C5), 10049–10073, doi:10.1029/94JC00168.

Serreze, M. C., A. P. Barrett, A. G. Slater et al. (2006), The large-scale freshwater cycle of the Arctic, *J. Geophys. Res.*, 111, C11010, doi:10.1029/2005JC003424.

Smith, G. C., F. Roy, P. Mann, F. Dupont, B. Brasnett, J. F. Lemieux, S. Laroche and S. Bélair (2013), A new atmospheric dataset for forcing ice-ocean models: Evaluation of reforecasts using the Canadian global deterministic prediction system, *Q. J. R. Meteorol. Soc.*, 140, 881–894, doi:10.1002/qj.2194.

St. Laurent, L., S. Stringer, C. Garrett and D. Perrault-Joncas (2003), The generation of internal tides at abrupt topography, *Deep-Sea Res. I*, 50, 987–1003, doi:10.1016/S0967-0637(03)00096-7.

St. Laurent, L. C., H. L. Simmons and S. R. Jayne (2002), Estimating tidally driven mixing in the deep ocean, *Geophys. Res. Lett.*, 29, doi:10.1029/2002GL015633.

St Laurent, L. C. and A. M. Thurnherr (2007), Intense mixing of lower thermocline water on the crest of the Mid-Atlantic Ridge, *Nature*, 448, 680–683, doi:10.1038/nature06043.

Staalstrøm, A., L. Arneborg, B. Liljebladh and G. Broström (2015), Observations of turbulence caused by a combination of tides and mean baroclinic flow over a fjord sill, *J. Phys. Oceanogr.*, 45(2), 355–368, doi:10.1175/JPO-D-13-0200.1.

Stigebrandt, A. and J. Aure (1989), Vertical mixing in basin waters of fjords, *J. Phys. Oceanogr.*, 19, 917–926, doi:10.1175/1520-0485(1989)019<0917:VMIBWO>2.0.CO;2.

Støylen, E. and I. Fer (2014), Tidally induced internal motion in an Arctic fjord, *Nonlin. Processes Geophys.*, 21, 87–100, doi:10.5194/npg-21-87-2014.

Tanaka, Y., T. Hibiya, Y. Niwa and N. Iwamae (2010), Numerical study of K_1 internal tides in the Kuril straits, *J. Geophys. Res.*, 115(C9), doi:10.1029/2009JC005903.

Taylor, G. I. (1919), Tidal friction in the Irish Sea, *Phil. Trans. Roy. Soc. A*, 220, 1–33, doi:10.1098/rsta.1920.0001.

Tennekes, H. and J. L. Lumley (1972), *A first course in turbulence*, MIT Press.

Topham, D. R., R. G. Perkin, S. D. Smith, R. J. Anderson and G. den Hartog (1983), An investigation of a polynya in the Canadian Archipelago, 1, Introduction and oceanography, *J. Geophys. Res*, 88, 2888–2899, doi:10.1029/JC088iC05p02888.

Vlasenko, V., N. Stashchuk, K. Hutter and K. Sabinin (2003), Nonlinear internal waves forced by tides near the critical latitude, *Deep-Sea Res. I*, 50, 317–338, doi:10.1016/S0967-0637(03)00018-9.

Wadley, M. R. and G. R. Bigg (2002), Impact of flow through the Canadian Archipelago and Bering Strait on the North Atlantic and Arctic circulation: An ocean modelling study, *Q. J. R. Meteorol. Soc.*, 128(585), 2187–2203, doi:10.1256/qj.00.35.

Wang, Q., M. Ilicak, R. Gerdes et al. (2016), An assessment of the Arctic Ocean in a suite of interannual CORE-II simulations. Part II: Liquid freshwater, *Ocean Modell.*, 99, 86–109, doi:10.1016/j.ocemod.2015.12.009.

Wang, Q., P. G. Myers, X. Hu and A. B. G. Bush (2012), Flow constraints on pathways through the Canadian Arctic Archipelago, *Atmosphere-Ocean*, 50, 373–385, doi:10.1080/07055900.2012.704348.

Wang, Q., C. Wekerle, S. Danilov, X. Wang and T. Jung (2017), A 4.5 km resolution Arctic Ocean simulation with the global multi-resolution model FESOM1.4, *Geosci. Model Dev. Discuss.*, (July), doi:10.5194/gmd-2017-136.

Warner, S. J. and P. MacCready (2009), Dissecting the pressure field in tidal flow past a headland: When is form drag "real"?, *J. Phys. Oceanogr.*, 39, 2971–2984, doi:10.1175/2009JPO4173.1.

Warner, S. J. and P. MacCready (2014), The dynamics of pressure and form drag on a sloping headland: Internal waves versus eddies, *J. Geophys. Res.*, 119, 1554–1571, doi:10.1002/2013JC009757.

Warner, S. J., P. MacCready, J. N. Moum and J. D. Nash (2013), Measurement of tidal form drag using seafloor pressure sensors, *J. Phys. Oceanogr.*, 43, 1150–1172, doi:10.1175/JPO-D-12-0163.1.

Wekerle, C., Q. Wang, S. Danilov, T. Jung and J. Schröter (2013), The Canadian Arctic Archipelago throughflow in a multiresolution global model: Model assessment and the driving mechanism of interannual variability, *J. Geophys. Res.*, 118, 4525–4541, doi:10.1002/jgrc.20330.

Whalen, C. B., L. D. Talley and J. A. MacKinnon (2012), Spatial and temporal variability of global ocean mixing inferred from Argo profiles, *Geophys. Res. Lett.*, 39, L18612, doi:10.1029/2012GL053196.

Woodgate, R. (2013), Arctic Ocean circulation: going around at the top of the world, *Nat. Educ. Knowl.*, 4(8).

Zhang, Y., C. Chen, R. C. Beardsley et al. (2016), Studies of the Canadian Arctic Archipelago water transport and its relationship to basin-local forcings: Results from AO-FVCOM, *J. Geophys. Res.*, 121, 4392–4415, doi:10.1002/2016JC011634.